UNIVERSITY OF SOUTHAMPTON

FACULTY OF SCIENCE

DEPARTMENT OF PHYSICS

KERNEL DENSITY ESTIMATORS APPLIED TO HARD X-RAY OBSERVATIONS OF THE CRAB PULSAR

by

Ian Ruthven Carstairs, B.Sc., F.R.A.S.

A thesis submitted for the degree of

Doctor of Philosophy

April 1992

UNIVERSITY OF SOUTHAMPTON

ABSTRACT

FACULTY OF SCIENCE

PHYSICS

Doctor of Philosophy

KERNEL DENSITY ESTIMATORS APPLIED TO HARD X-RAY OBSERVATIONS OF THE CRAB PULSAR

by Ian Ruthven Carstairs

The *MIFRASO* balloon-borne hard X-ray telescope made three observations of the Crab Pulsar during its flights in 1986 and 1987. A number of other objects were also observed, such as the galactic binary systems A0535+26, Cygnus X-1 and Hercules X-1, the Seyfert galaxies NGC 4151 and MCG 8-11-11, the quasar 3C273, the Coma galactic cluster and the unusual binary system SS433. The telescope had an energy range of 15-300 keV with a fine timing resolution of 0.33ms.

The kernel density estimator (KDE) technique has been recently proposed as an unbiased estimator of pulsar light curves. The KDE technique is an alternative to the traditional binned histogram and has been applied to the *MIFRASO* observations, providing consistent results which are more sensitive to the shape of the pulsed emission. The accompanying statistical test for phase uniformity, the $H_{\hat{m}}$ test, has been applied to one of the Crab observations in a periodicity search. The resulting period was found to agree with the radio period of the pulsar, interpolated to a time contemporary with the *MIFRASO* observations. The traditional tests for phase uniformity, the Pearson and Rayleigh tests, were also investigated and found to be inferior to the new $H_{\hat{m}}$ test.

Spectral deconvolution of the time-averaged Crab Pulsar signal was performed and the resultant power-law fit found to be in good agreement with pervious observations. Using the pulse profiles estimated using the KDE technique, the pulsed emission was separated from the unpulsed emission and separately deconvolved. The resultant spectrum is well described by a power-law fit of harder spectral index than the time-averaged spectrum, in agreement with current models of the pulsar emission mechanisms.

Finally, a period searching algorithm using the $H_{\hat{m}}$ test was implemented upon a transputer array, providing significant speedups in execution time. A limited periodicity search of the *MIFRASO* observation of the X-ray binary Cygnus X-1 using the transputer-implemented $H_{\hat{m}}$ test failed to reveal any pulsations.

'...the way we look to a distant constellation
that's dying in a corner of the sky,
these are the days of miracle and wonder...'

- Paul Simon,
from the 'Graceland' album

The Crab Nebula in the constellation of Taurus. The Nebula is the result of a star exploding in the year 1054 A.D., which may have been witnessed and recorded by our ancestors. At the centre of the expanding Nebula lies the Crab Pulsar, a collapsed star rotating thirty times a second and sending out a beam of radiation that encompasses radio waves right the way through to very high energy gamma rays.

Dedicated to the life, dreams and vision of
Gene Roddenberry
(1921 – 1991).

PREFACE

The *MIFRASO* balloon-borne hard X-ray telescope project was an international team effort with collaborators from three separate institutes. This thesis is primarily concerned with the application of new forms of timing analysis to the *MIFRASO* observations of the Crab Pulsar carried out in 1986 and 1987. The author was entirely responsible for the reduction of the fast timing information gathered with this telescope. Although he played no part in the actual construction of the telescope, the author did support the abortive 1989 launch campaign and prepared some of the hardware for the down-range telemetry stations. The author also assisted in the energy and attitude-sensor calibration of the instrument prior to launch.

The initiative to use the kernel density estimation technique on the observations of the Crab Pulsar was entirely the author's and this work forms the bulk of this thesis. Timing analysis routines for the analysis of the A0535+26 data were also written by the author. In addition, the author collaborated on writing a parallel version of the $H_{\hat{m}}$ test running on an array of transputers which was used to period search the Crab and Cygnus X-1 data. Finally, the author collaborated with workers in Milan on the spectral deconvolution of the Crab Pulsar pulse profile.

CONTENTS

APPENDICES

INTRODUCTION

'For many years it was stated that there were two areas of study in astronomy : the Crab Nebula and all the rest'

- Professor Arnold Wolfendale

The discovery of pulsars by Jocelyn Bell-Burnell and Antony Hewish in 1967 (Hewish et al., 1968) began a new era in observational astronomy. Since those early days, hundreds of pulsars have been discovered, both single, isolated radio pulsars and accretion-driven binary X-ray pulsars. The search for new pulsars is one of the most exciting fields in modern astronomy and covers wavelengths from radio through to the highest energy ground-based gamma-ray detectors. As new observational techniques are developed to search for the pulsations, so new data analysis methods are also emerging to examine the data collected by these new experiments.

Despite the exotic nature of many of the pulsars detected, the 'familiar' Crab Pulsar at the centre of the Crab Nebula in the constellation of Taurus remains one of the most exciting. The youngest pulsar so far discovered, it was born in a supernova explosion that occurred just nine hundred years ago; an explosion which may well have been witnessed by our ancestors. The Crab Pulsar remains the only such object seen to emit radiation from radio waves through X-rays right up to very high energy gamma rays. Continually monitored in the radio band by Jodrell Bank Radio Observatory it is a popular target for new telescopes to observe. There are many exciting areas of research still waiting to be explored in the context of the Crab Pulsar : the possible sighting of cyclotron lines by some groups enables one to make direct estimates of the surface magnetic field of the pulsar, whilst the observation of glitches in the periodicity enable the interior of the neutron star to be probed. Some groups claimed to have seen subpulses, or microstructure, in the light curve, and this is another area that the present research has investigated.

This thesis concerns itself with three observations of the Crab pulsar made in the hard X-ray region with the *MIFRASO* (*MI*lan-*FRA*scati-*SO*-uthampton) balloon borne telescope. The telescope is the result of an international collaboration between three institutes: the Astronomy Group at Southampton University and the CNR institutes of Milan and Frascati, Italy. The telescope has had two successful flights, in 1986 and 1987 and has provided a wealth of new measurements on galactic and extra-galactic sources. The author personally took part in the 1989 launch campaign of *MIFRASO* which was marred by a balloon failure just after launch.

The thesis is concerned primarily with the timing analysis of the Crab Pulsar, although spectral results are included as well. These include the search for cyclotron lines in the energy spectrum, for example. A new technique both for the estimation of the light curve and for searching for a pulsed signature has been recently developed for the analysis of high-energy data and this technique, the 'kernel density estimator technique' has been adapted by the author for the analysis of the *MIFRASO* hard X-ray observations. To the author's knowledge this is the first time that such a method has been used to interpret pulsar timing results outside of the original group that developed it, and the first time that it has been applied to hard X-ray results. The initiative to use these new methods to analyse the *MIFRASO* observations of the Crab Pulsar was entirely the author's. The new method has several advantages over the older methods of binning the light curve and using the well-established chi-squared or Rayleigh tests for periodicity searches.

The advent of parallel processing on arrays of transputers represents a new era in the computational side of modern astronomical data analysis, enabling considerable decreases in computation time in, for example, pulsar searches to be achieved. The author has been involved in the use of a transputer array in the Southampton Astronomy group and has developed parallel code for the new timing analysis software to be run on the array. Parallel versions of the timing routines run on the transputer array were used throughout this thesis.

Finally, the author applied the new methods for pulsar searching to a *MIFRASO* observation of the suspected black hole candidate Cygnus X-1. No-one knows for sure whether the compact object in the binary system is a black hole or a pulsar, and it is only by conducting such searches that new discoveries will be made.

CHAPTER 1 : THE GUEST STAR IN TAURUS

1.1 Historical Sketch

The Crab Nebula and its associated Crab Pulsar are the remains of a supernova explosion that occurred on 4th July, 1054. There has been considerable interest in ancient sightings and records of this event, in the hope that they will provide clues as to the early features of the explosion and the subsequent growth of the nebula.'Guest Star' is a term that the ancient Chinese and the people of the Far East used to describe a new star, that is, a star that suddenly appeared in the sky and then gradually disappeared from sight. For example, the novae and supernovae of AD 1006, 1572 and 1604 were all described as Guest Stars by Chinese, Japanese and Korean astronomers. It is natural to search for historical records of the Crab explosion, and several appear below (Mitton, 1979) :

'In the first year of Zhi-ho reign period, fifth day of Ji-chou, a Guest Star appeared approximately several inches to the south-east of Tian-guan. After a year and more it gradually vanished.'

- Sung-Shi

'In the first year of the Jia-hu reign period, third month, day of Xin-wei, the Director of the Astronomical Bureau reported that since the fifth month of the first year of the Zhi-ho reign period a Guest Star has appeared in the morning in the east guarding Tian-guan and had only now become invisible.'

- Sung-Shi-Ren-Zong-Ben-Ji

'In the first year of the Zhi-ho reign period, seventh month, twenty- second day ... Yang Weide said : 'I humbly observe that a Guest Star has appeared, and above the star in question there is a faint glow, yellow in colour.'

'During the third month of the first year of the Jia-hu reign period the director of the Astronomical Bureau said : 'The Guest Star has vanished .' Earlier, during the first day of the Zhi-ho reign period the Guest Star appeared in the morning in the east, guarding Tian-guan. It was visible in the daytime, like Venus. It had pointed rays on all sides and its colour was reddish-white, and it was visible for twenty-three days'

- Sung-Hui-Yao

'In the second year of the Tenki reign period, forth month, after the middle decade, at the hour of Chou, a Guest Star appeared in the degree of Tsue and Shen. It was seen in the east and flared up at Tian-guan. It was as large as Jupiter.'

- Meigetsuki

Among all of the historical records, about 80% are from China, dating from the time of the Sung dynasty. All of the above quotations mention '*Tian-guan*'. This is thought to refer to the star zeta-Tau. Fig.1.1 shows the position of this star with respect to the Crab. The Japanese record by Meigetsuki quoted above refers to the 'degrees of Tsui and Shen', zones of right ascension which have been plotted on the chart.

It is significant that none of the sightings refer to the Crab explosion as a comet, but rather use the correct term for a Guest Star ('*k'o-hsing*'). Furthermore, the various accounts remain silent on any motion of the star during the very long period of visibility, nearly two years,

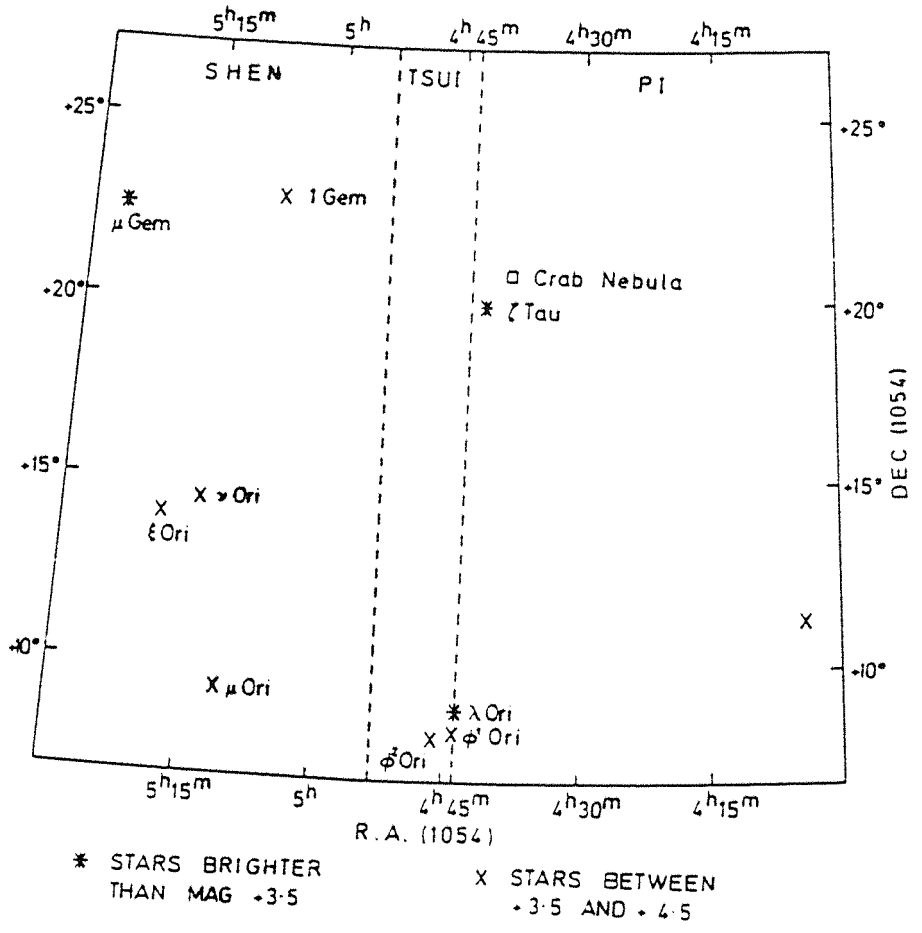

Fig.1.1. The position of the star zeta-tau with respect to the Crab Nebula. Also shown are the 'degrees of Tsui and Shen', zones of right ascension. From Clark and Stephenson, 1978.

which would be unusual for a comet. The third record quoted above shows the star still in the vicinity of zeta-Tau nearly two months after its first appearance.

Although well placed for observation in the northern hemisphere, there is not a single record of the event from European or Arab astronomers. However, there may well be records from the Navajo Indians of northern Arizona. Fig.1.2 shows two of the petroglyphs (rock paintings) discovered in 1955. The designs show a crescent and a circle, which were interpreted to depict the crescent moon and a nearby supernova explosion. The deduction is superficially plausible because on the morning of 4th July 1054 the crescent moon, as seen from north America, was very close to the supernova. Furthermore, the crescent design is very rare in meso-American rock art. The exact date when the paintings were made is not known, but further archaeological evidence suggest that the caves housing the paintings were inhabited during the year 1054. Several similar paintings were found in the 1970s.

In 1972 archaeologists found a painting in red hematite of a handprint, inverted crescent moon, the sun and a bright star at Chaco Canyon, north-west New Mexico. The location is known to be a sacred site of the Pueblo Indians who inhabited the area from the tenth to the twelfth centuries. Two more similar paintings have been found in other parts of New Mexico. Although there are doubts concerning the validity of these paintings in depicting the Crab supernova explosion, the possibility that Hohokam and Anasazi ancient astronomers in North America saw the event and recorded it in their art is certainly an intriguing one.

Moving on to modern times, the telescope has revolutionised our knowledge of the skies. It was in 1731 that the Crab Nebula was first discovered with the telescope. The English amateur astronomer John Bevis set out to produce a new atlas of the stars, and editions of his atlas with their finely engraved copper plates clearly show the Crab in the correct position next to zeta-Tau. Fig.1.3 shows plate XXIII from his 'Uranographia Britannica' showing the Crab

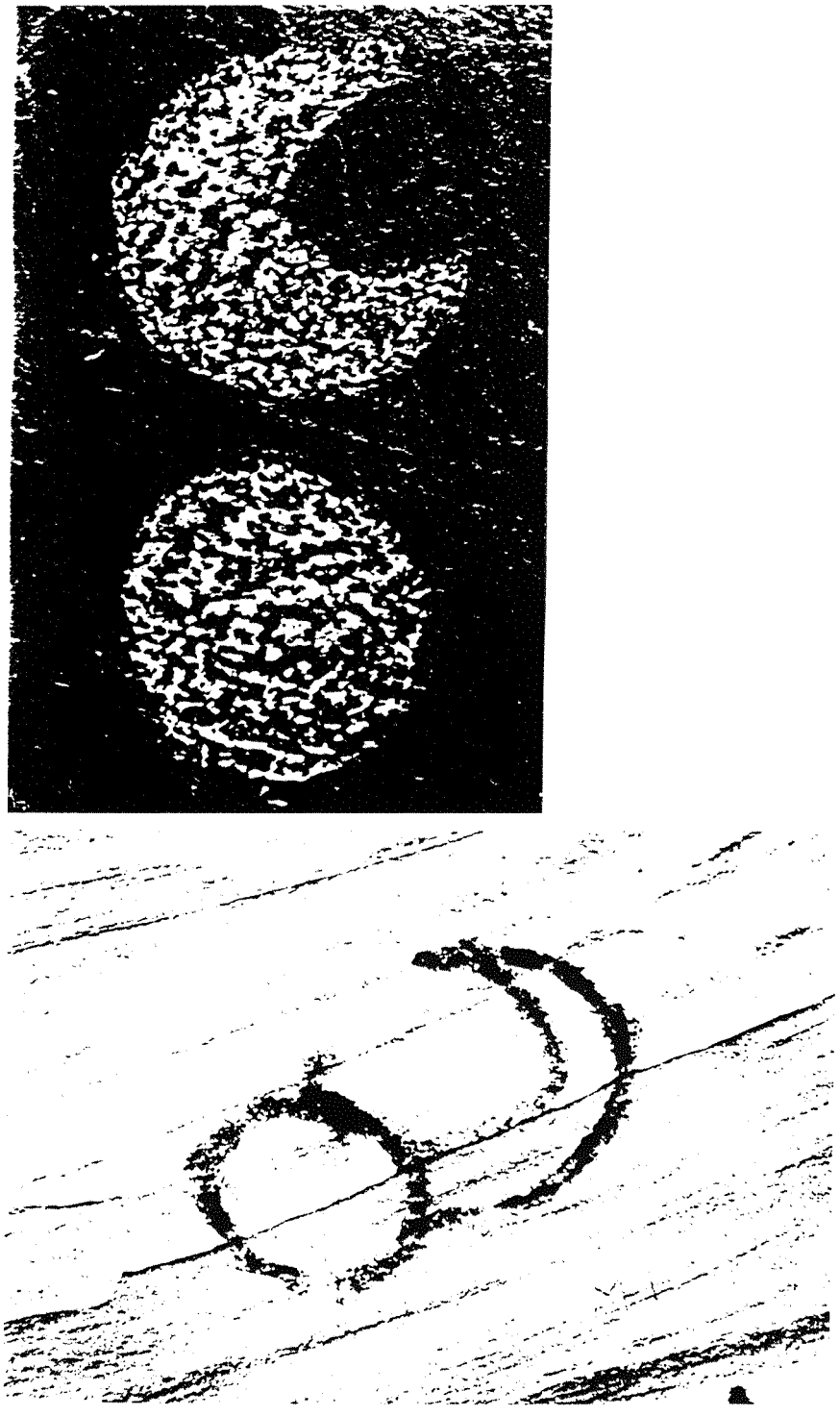

Fig.1.2. Two of the rock paintings discovered in 1955 by William C. Miller in northern Arizona (a) on a wall in the Navaho Canyon and (b) on a cave wall in White Mesa. They may be symbolic representations of the crescent moon and the Crab supernova explosion of 1054 A.D. From Mitton, 1979.

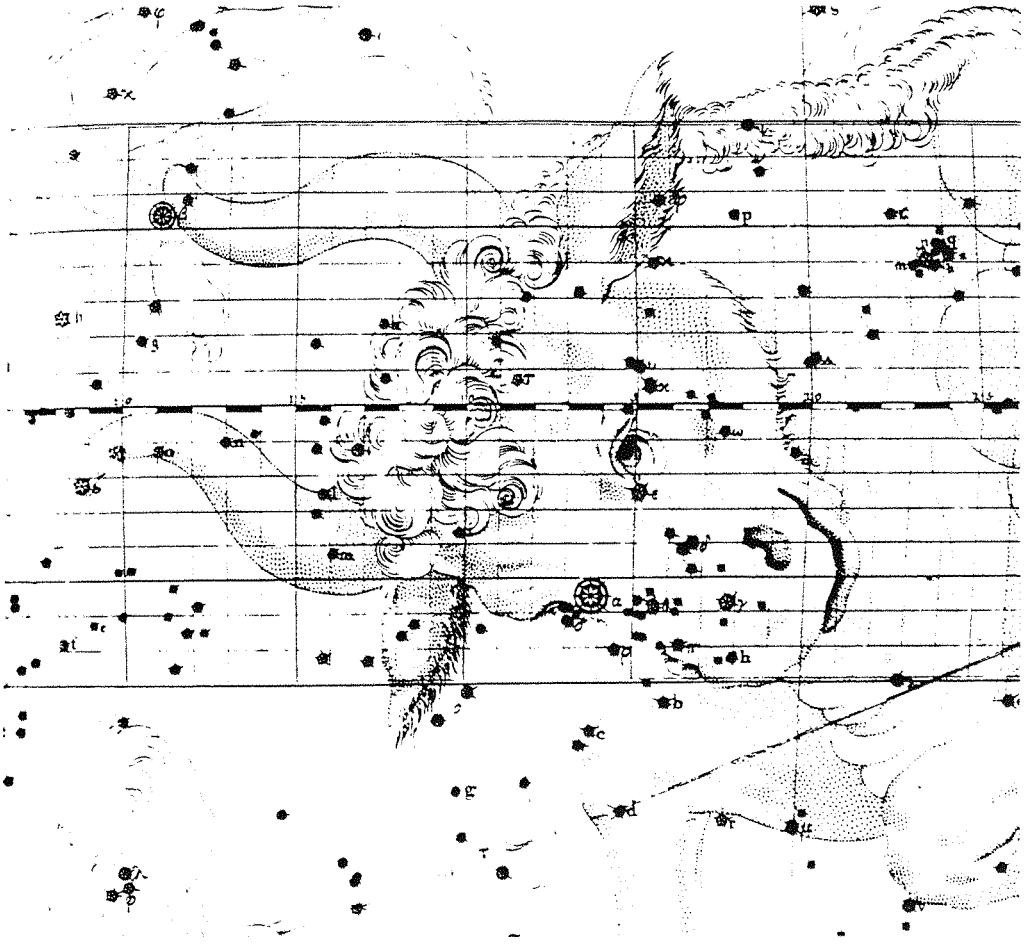

Fig.1.3. Portion of Plate XIII from John Bevis' 'Uranographia Britannica' showing the constellation Taurus. The Crab Nebula, found by Bevis in 1731, is marked as a faint round symbol above and to the right of Zeta-Tau. From Mitton, 1979.

Nebula as the faint round symbol above and to the right of zeta-Tau. Despite having his atlas, Bevis did not publisise the discovery of the Nebula. In 1771 Bevis wrote to Charles Messier in order to draw his attention to the Nebula, although it is possible that Messier already knew about the Crab. Messier acknowledged the discovery by Bevis in the definitive version of the Messier catalogue published in 1784, where the Crab Nebula was given as the first entry in the catalogue, M1.

The publishing of Messier's catalogue stimulated further research on the nature of nebulae. It was the Third Earl of Rosse who first used the term the 'Crab Nebula' to describe M1. He built many large telescopes for observing nebulae and star fields, and in a paper in the Philosophical Transactions of the Royal Society for 1844 published drawings that are believed to have led to the widespread use of the term 'Crab Nebula' owing to its superficial resemblance to a crab. Lord Rosse first used this name himself in 1848. He included the following description of it :

'...we see resolvable filaments singularly disposed, springing principally from its southern extremity, and not, as is usual in clusters, irregularly in all directions. Probably a greater power would bring out other filaments, and it would then assume the ordinary form of a cluster...'

Rosse here echoes the then generally held view that the nebula would clarify into masses of stars with sufficiently high resolving power. Over the years Rosse continued intermittently to observe the Crab Nebula as part of a vast project of nebula observations. In 1880 the Royal Dublin Society published Rosse's observations of nebulae and stars. The remarks on the Crab Nebula underline the difficulties faced when observing nebulae prior to the introduction of photography. For example, the entry for 29th November 1848 reads :

'Crab Nebula. Would have figured it different from drawing in Philosophical Transactions 1844'

By 1885 Lord Rosse had enough data for the engraving of a plate of the Crab Nebula. Despite the obvious shortcomings of Rosse's work compared to modern photographs, his engraving has much in common with the finest photographs, including the prominent 'bay' in the eastern part of the nebula and the filament structure. Fig.1.4 shows two sketches of the Crab Nebula made by Rosse.

One of Rosse's acquaintances was the English amateur astronomer William Lassell, who built a 24-inch reflector and moved to Malta to observe. In his notes on the Mediterranean observations of the Crab made in 1852 we find reference to stars apparently embedded in it as well as to the delicate filamentary structure :

'With 160X power of eyepiece it is a very bright nebula, with two or three stars in it, but with 565X it becomes a much more remarkable object . .. Long filaments run out from all sides and there seems to be a number of very faint and minute stars scattered over it.'

The general picture of the nebula that emerged from these early visual observations was of an object with complex structure, such as bays and filaments, with some stars in the field of view. It could not itself be resolved into myriads of stars, as had been the case with many nebulae now properly called star clusters.

In 1892 a 20-inch reflecting telescope obtained the first photograph of the Crab. Later many of the astronomers active at the turn of the century took photographs of it. Most thought it was an anomalous planetary nebula. Photographs taken in the usual spectral range of 360-500nm show the amorphous nebula with a distorted S-shape together with a tangle of bright

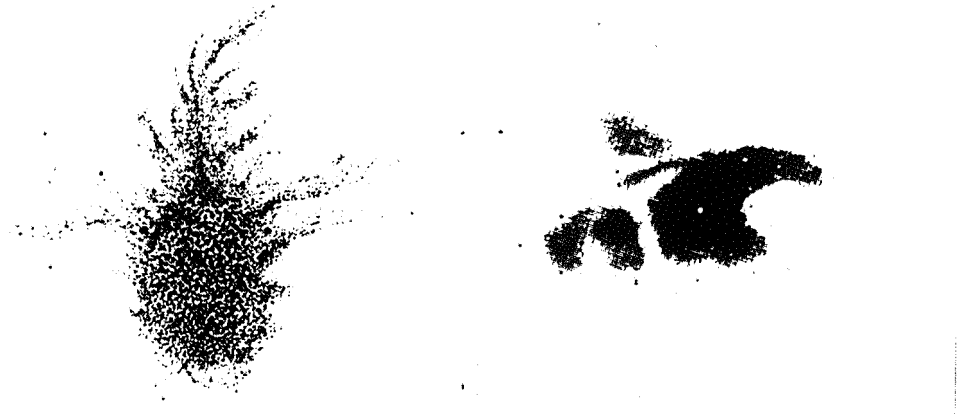

Fig.1.4. Sketches of the Crab Nebula made by Lord Rosse. It was Lord Rosse who first used the expression 'Crab Nebula' to describe this object. From Mitton, 1979.

thread-like filaments.

V.M.Slipher working at the Lowell Observatory, Arizona, was the first person to apply spectroscopy to the Crab Nebula. In the period 1913 to 1915 he took spectra of the Crab and in doing so made a significant discovery. He found that individual emission lines in the spectrum were split into components with slightly different wavelengths. Slipher knew about the recently demonstrated Stark effect and concluded that strong electric fields in the Nebula were responsible for splitting the spectral lines. Although he turned out to be wrong in this instance his approach to the Crab Nebula was correct : the Nebula is a unique physics laboratory in the sky.

In 1921 C.O.Lampland, working at the Lowell Observatory, compared detailed photographs of the Crab taken over a period of eight years and discovered noticeable motion in individual components. He found that both dark and luminous features had moved significantly in that period . In addition to the movement, Lampland found changes in brightness of certain parts of the nebula that could not be attributed to movement. Important independent confirmation of Lampland's discovery came from J.C.Duncan of the Mount Wilson Observatory who measured the relative movement of individual knots and clumps. He used two plates, taken with the 60-inch Mount Wilson telescope taken 11.5 years apart. The research demonstrated that material was moving out from the center of the Crab Nebula. It immediately became clear, extrapolating backwards from these motions, that the expansion of the Crab Nebula must have begun about 900 years earlier. In the same year, Lundmark was to note the proximity of the Crab to the Guest Star of A.D.1054.

In 1928 Hubble was to associate the nebula with the supernova explosion of 1054. Conclusive evidence of this association was provided by Duyvendak, Oort and Mayall in 1942. Photographs of the nebula taken in several colours by Baade in 1942 showed that it consisted of a network of line-emitting filaments superimposed upon a more uniform region of continuous

emission. Nearly all of the visible light comes from this central region. The radio source Taurus A was discovered by Bolton in 1948 and identified with the Crab by Bolton, Stanley and Slee in 1949 - this was the first radio source to be identified with an optical object. In 1953 Shklovskii proposed that the optical continuum radiation was generated by the synchrotron process; his prediction that the light from the nebula should be linearly polarised was confirmed in 1954. A strong source of X- rays in Taurus was identified with the Crab by Bowyer in 1964 - one of the first identifications of a celestial X-ray source. In the same year, a low-frequency, point-like radio source was discovered near the centre of the nebula by Hewisk and Okoye. Finally, a pulsar was found in the nebula by Staelin and Reifenstein in 1968. The pulsar is ultimately responsible for most of the emission from the nebula, from radio through to X and gamma-rays.

Due to the close association between the nebula and the pulsar, there follows a review of each, starting with the Crab Nebula.

1.2 The Crab Nebula

At radio and X-ray wavelengths the Crab Nebula is one of the brightest sources in the sky, although at optical wavelengths it is not so prominent with an apparent visual magnitude of 8.4 (Manchester and Taylor, 1977). Fig.1.5 shows the continuum spectra of both the nebula and the pulsar from low radio frequencies to the gamma-ray region. The nebula spectrum appears to be essentially continuous over this entire range, although observations are lacking in the far infrared and ultraviolet regions. With the possible exception of the highest gamma-ray energies, the entire nebula emission is almost certainly generated by the synchrotron process. The luminosity derived from the nebula spectrum under the assumption of isotropic emission is 10^{38} erg s^{-1}, of which about 12% is emitted at radio frequencies. High resolution radio maps

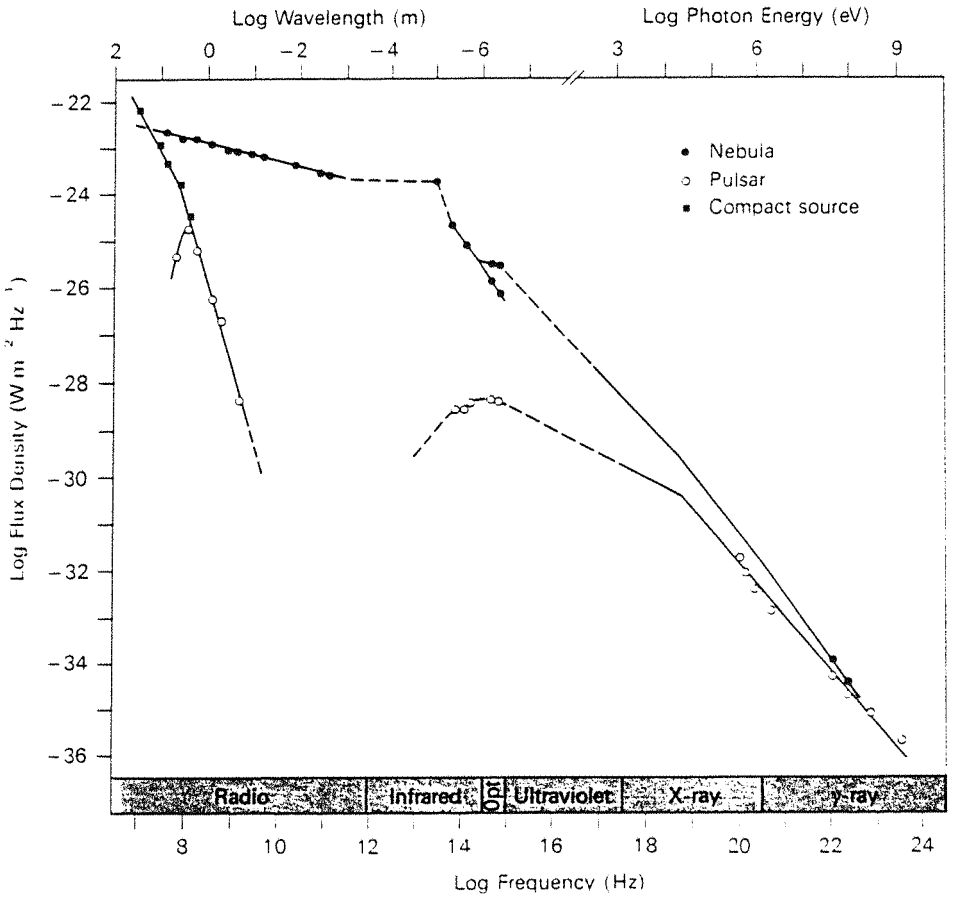

Fig.1.5. Spectra of the Crab Nebula and its pulsar over the range 10^7 to 10^{24} Hz. Two lines are drawn for the nebula spectrum in the optical region: the lower is the observed spectrum and the upper is corrected for interstellar extinction. From Manchester and Taylor, 1977.

show a roughly elliptical shape of the nebula, see Fig.1.6. Half-intensity widths are 3.5' arc for the major axis and 2.3' arc for the minor axis. Assuming a distance of 2kpc to the nebula, the corresponding linear dimensions are about 2.0pc and 1.3pc respectively.

There is considerable structure within the nebula, the most prominent features being the 'bays' in the southeast and northwest edges of the nebula. Because of these bays, the continuum emission forms an S-shaped ridge along the major axis; there is no evidence for the shell-like structure seen in most supernova remnants. Several of the ridges seen in the radio map coincide with line-emitting optical filaments, this has been attributed to synchrotron radiation in stronger magnetic fields surrounding the filaments (Wilson, 1972). These stronger fields probably result from currents flowing along the filaments and may confine the filaments by means of the pinch effect. Although the optical continuum is often called 'amorphous', the highest resolution photographs show that it consists of a mass of very fine filaments that may be aligned with the magnetic field of the nebula.

Polarization studies of the X-ray emission have found that the integrated linear polarization of the nebula emission is about 15%, with a position angle similar to that of the optical emission in the central region. This is strong evidence that synchrotron emission is responsible for the nebula X-rays as well as the radio and optical emission (Weisskopf et al., 1976). This is a unique feature of the Crab Nebula, as in other supernova remnants X-rays are most probably generated by the thermal bremsstralung process.

From considerations of the lifetime of relativistic electrons, the lifetime of the electrons producing the radio emission from the nebula is approximately 6000 years; it is thus possible that these electrons were produced at the time of the supernova explosion. However, for the optical and X-ray emissions the lifetime of the electrons is much less than the age of the nebula, for example, for X-rays the electron lifetime is 10 weeks. Clearly, such electrons cannot have been produced at the time of the supernova explosion and still be radiating. So, if the optical

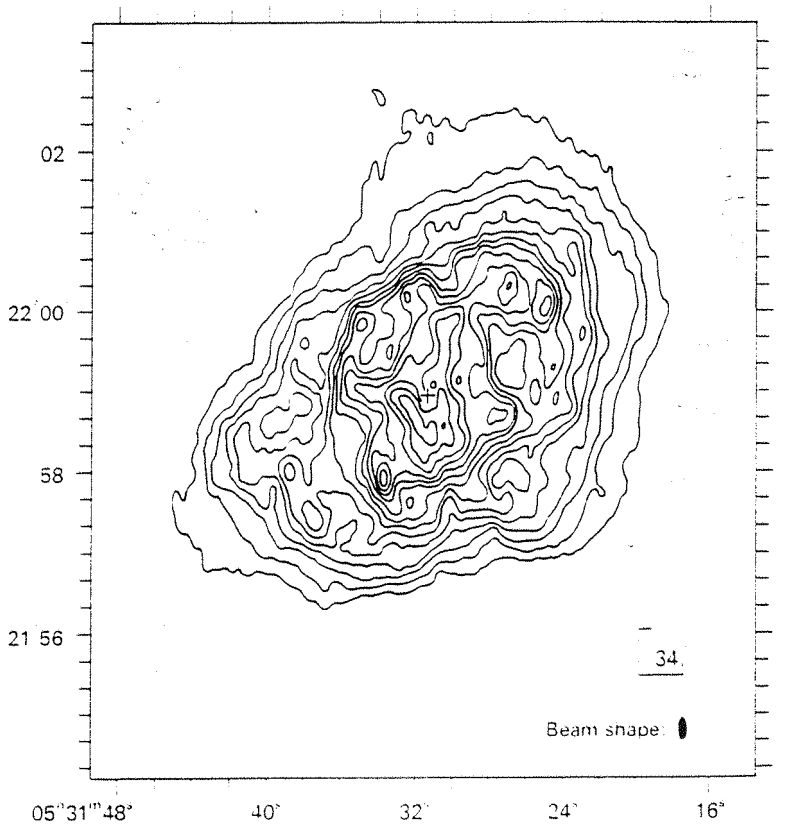

Fig.1.6. High resolution radio map of the Crab Nebula at 5 GHz. The Crab pulsar is located in the centre of the map (marked with a cross). From Manchester and Taylor, 1977.

and X-ray emission is to be interpreted as synchrotron emission, continuous injection or acceleration of relativistic electrons is required.

Before the discovery of the Crab Pulsar this represented a major problem in understanding the physics of the Crab Nebula. It is likely that pulsars are efficient in accelerating particles to ultra-relativistic energies. The X-ray source at high energies (100keV) has a diameter of about one light year. Because of the short lifetime against radiation losses, the radiating electrons cannot be accelerated at the pulsar. Furthermore, it has been pointed out (Tademaru, 1973 and Cocke, 1975), that, because of curvature radiation losses, electrons injected into the nebula by the pulsar will have an upper energy limit of about $3x10^{12}$eV, corresponding to a synchrotron frequency of about 10^{16}Hz. It has been proposed (Cocke, 1975) that further acceleration occurs by a Fermi process in a small region (radius 0.2pc) surrounding the pulsar. This model provides a natural explanation for the extended nature of the hard X-ray source and its steep spectrum. The total rate of particle injection from the pulsar required to account for the observed luminosity is about 10^{38} particles per second.

If the nebula continuum radiation is interpreted as arising from synchrotron radiation, then strong magnetic fields are required to exist throughout the nebula. The field strength and particle energy are related by the observed synchrotron luminosity. For equipartition, the field strength is about $5x10^{-4}$G. Polarisation measurements show that the magnetic field is a regular, large-scale structure, and it is not obvious where the field came from. Expansion of the stellar field with the supernova explosion is not possible because the ratio of gravitational to magnetic energy is too small.

Recent developments in observations of the Crab Nebula include near- infrared high resolution (0.5") photographs of the nebula taken with the Canada-France-Hawaii telescope (van den Bergh and Pritchet, 1989), see Plate 1.1. This shows the fibrous structure of the

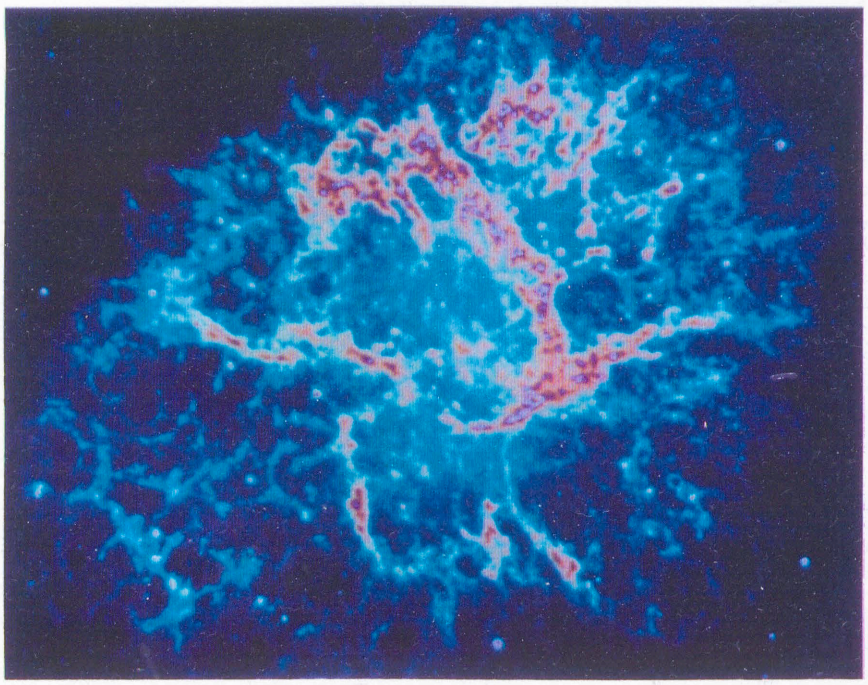

Plate 1.1. Near-infrared image of the Crab Nebula with images having a FWHM= 0.52".The use of a near-infrared filter and computer processing resulted in a view of the pulsar and its surroundings that emphasises the nebulosity shining by synchrotron emission relative to light from more familiar emission lines. (Pritchet, private communication).

synchrotron nebulosity and wisps near the pulsar with unprecedented clarity, and suggest that the wisps are synchrotron-emitting fibers that have been pushed outward, and become more luminous, as a result of interaction with particles emitted by the pulsar.

1.3 The Crab Pulsar

Two pulsars were discovered near the Crab Nebula (Staelin and Reifenstein, 1968), and in the following year observations that one of the pulsars was within the nebula and had the short period of 33ms (Comella et al., 1969) heralded a new dimension to the investigation of the system. With the observation of the regularly increasing period of the pulsar (Richards and Comella, 1969), a likely solution to the energy-supply problem for the nebula had been found. Later the same year, optical pulses were discovered with the same period as the radio pulses (Cocke et al., 1969). The spectrum of the pulsar emission was further extended by the discovery of X-ray pulses (Fritz et al., 1969) and of gamma-ray pulses (Hillier et al., 1970).

Fig.1.8 shows integrated pulse profiles of the Crab Pulsar from radio through to gamma-rays. All show the same shape, with a primary and a secondary pulse separated by an interpulse region. (Note that some authors refer to the interpulse rather than the secondary pulse). The separation of the primary and secondary pulse is 13.37±0.03ms. or 0.404 in phase. At radio frequencies below about 700 MHz a forth component known as the precursor can be detected immediately preceeding the primary pulse.

The primary pulse has a very sharp peak at both radio and optical frequencies. At 430 MHz the width of the peak in the integrated pulse profile is less than 300 μs. (Rankin et al., 1970), while the peak is unresolved with a sampling interval of 32μs. at optical frequencies (Papaliolios et al., 1970). Measurements of the pulse arrival times show the peaks of the radio and optical primary pulses emitted simultaneously to within 200μs., furthermore, the X-ray primary pulse is coincident with the optical main pulse to within 500μs. (Kurfess and Share,

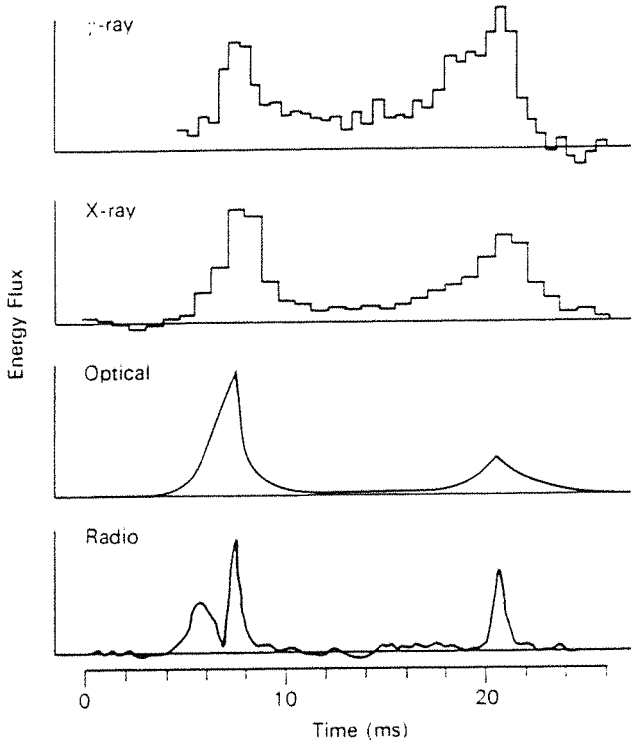

Fig.1.8. The integrated pulse profiles of the Crab Pulsar from radio through to gamma-rays.From Manchester and Taylor. 1977.

1973). The existence of such sharp features implies that the extent of the emission region is small, less than 10km for δt less than 30 μs. This small size in turn implies brightness temperatures of the order of 10^{29}K or more at radio frequencies.

From a three-year observation programme carried out at Arecibo Observatory (Rankin et al., 1974) it was found that at 430 MHz the pulsar intensity varied by a factor of three, with a characteristic fluctuation time of about 30 days. At 196 MHz the characteristic fluctuation time is about 77 days, while at 74 MHz the intensity has declined steadily over the three years. More recent observations at 408 MHz (Lyne and Thorne, 1975) show that the pulsar intensity increased by a factor of four between November 1974 and January 1975.

The variation in intensity at radio wavelengths contrasts with the behaviour of the pulsar emission at optical wavelengths. Here both pulse shape and intensity are stable over long timescales. Searches were conducted over a three-year period and concluded that no change was apparent (Horowitz et al., 1972). Another search, this time over a five year period, found that the average shape from 1969 to 1974 changed by less than one percent of the peak intensity of the primary pulse (Groth, 1975a).

The spectral continuity and similarity of pulse shapes for the optical and X-ray emission suggests that they share the same underlying emission mechanism. Thus the increase in size of the secondary pulse at X- ray frequencies suggests that a small change in shape should exist across the optical band. It was found that the leading edge of the secondary pulse was about 1% brighter in the U band than in the V band, an effect of about the expected magnitude (Muncaster and Cooke, 1972).

Considerable linear polarisation has been detected in the integrated pulse profile at both radio and optical frequencies. The radio precursor is essentially 100% polarised, but the primary and secondary pulses only about 10% polarised. The polarisation angle is difficult to determine in these components, but it is probably constant and about equal to the position angle of the

precursor. At optical wavelengths the polarisation of the pulsed components is quite different. The fractional polarisation has a maximum value of about 20% near the leading edge of the main pulse and reaches a minimum of a few percent near the leading edge of the main pulse peak. The polarisation angle variation is an S-shaped curve with a total swing of about 160^o. The variation across the secondary pulse is similar to that of the primary pulse.

The position angle of the radio pulse is $145^o \pm 20^o$ (Manchester, 1972), this is close to the value at the peak of the optical primary pulse. It has been suggested (Ferguson et al., 1974) that the actual variation of position angle near the polarisation minimum of the optical pulse may be more complicated. These authors also find some evidence for long-term variability in the polarisation.

Another feature of the radio emission from the Crab Pulsar is the occasional occurrence of very strong radio pulses. It was these strong pulses that were first discovered by Staelin and Reifenstein in 1968. A plot of the relative flux densities against the relative number of strong pulses reveals a power law with exponent -2.5. Pulse widths are typically 100μs. or less, implying a brightness temperature in excess of 10^{31}K. However, despite these large intensities the strong pulses are sufficiently infrequent that they contribute only a few percent of the pulsed radio energy. These pulses are not observed above 500MHz and in general are only weakly polarised.

Clearly there is a great deal of information to be gained from studying the Crab Nebula and Pulsar at any wavelength, from radio through to the highest energy gamma-rays. One of the least explored regions is the hard X-ray regime, to be found between the soft X-ray and low energy gamma-ray areas. It is this region that motivated the design and construction of the *MIFRASO* telescope which provided the observations analysed in this thesis. A description of the design of the *MIFRASO* telescope provides the material for the next chapter.

CHAPTER 2 : THE *MIFRASO* BALLOON-BORNE HARD X-RAY TELESCOPE

2.1 Introduction.

The *MIFRASO* telescope is a large area, multitechnique experiment designed to make highly sensitive measurements of celestial X-ray sources over the energy range 15 to 300 keV, with a timing resolution of typically 0.3 ms for observations of the Crab Pulsar (Baker et al., 1984). The telescope is the result of an Anglo-Italian collaboration between the Department of Physics, Southampton University, Istituto di Fisica Cosmica, Milano, Italy and Istituto Astrofisica Spaziale, Frascati, Italy. The telescope employs a combination of 3200 cm^2 of sodium iodide crystals for the high energy detectors covering the range 20-300 keV together with 1800 cm^2 of xenon gas-filled proportional counters covering the energy range 15-150 keV. The proportional counters provide a higher energy resolution, typically less than 14% full-width half maximum at 60 KeV, while the scintillation array provide a higher sensitivity with somewhat poorer energy resolution of about 18% fwhm at 60 Kev. Directionality is achieved with a passive collimator with a field of view of about 2 square degrees with a steering system having a pointing noise of approximately 6 arc minutes peak to peak.

The arrangement of the various components of the telescope is shown in Fig.2.1. There are three main sections comprising the telescope. The central gondola contains all of the detection modules and electronics. The steering module is located immediately below the central gondola and contains the reaction wheel used for steering in azimuth. Finally, the outer gondola has been designed to absorb most of the impact on landing using the four legs which collapse on landing.

Plate 2.1. (top) The *MIFRASO* balloon-borne hard X-ray telescope during pre-flight calibration at the launch site of Trapani, Sicily.
(bottom) The *MIFRASO* telescope just before the ill-fated 1989 launch.

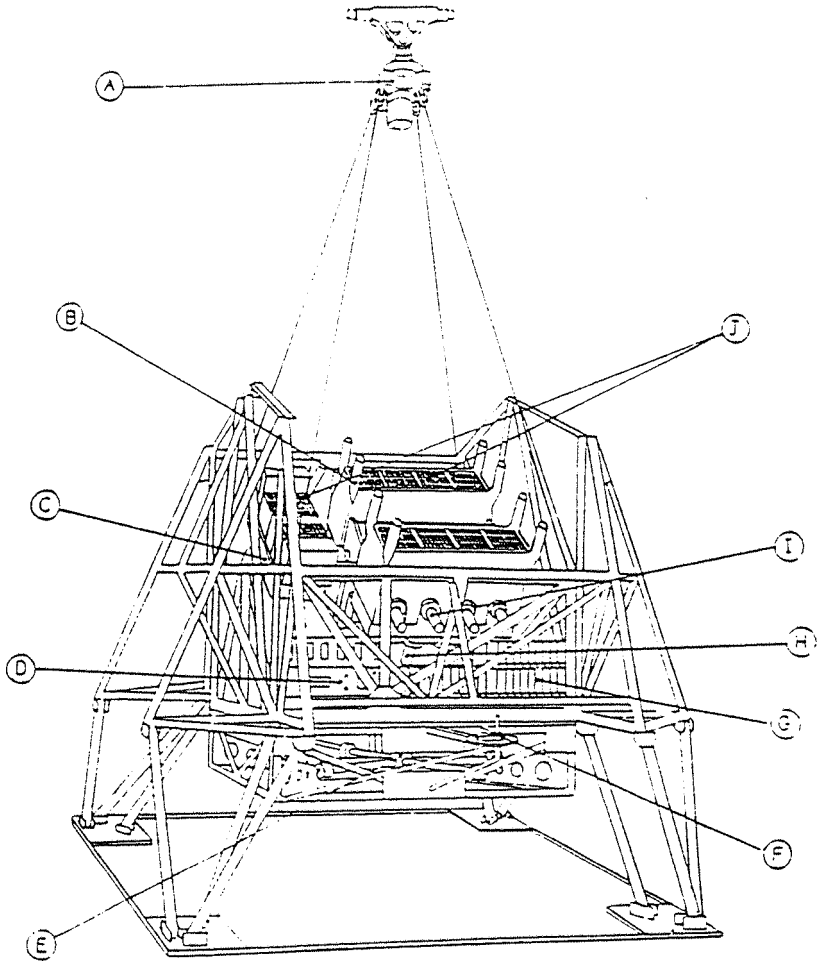

A. Upper steering gear.
B. Plastic anticoincidence.
C. Proportional Counter.
D. Steering electronics.
E. Reaction wheel.
F. Magnetometers.
G. P.S.M. electronics.
H. NaI anticoincidence unit.
I. NaI primary unit.
J. Collimators.

Fig.2.1. The *MIFRASO* hard X-ray telescope. From Lewis, 1984.

2.2 The Detection Systems

2.2.1 The Scintillator Array

The high energy detectors consist of an array of eight NaI(Tl) crystals of dimension 200 by 200 mm, each with a thickness of 6mm. Plan and cross-section views are shown in Fig.2.2. Light from each of the primary crystals is collected with a diffusive light-guide system placed above the crystal but below the collimators. Unlike conventional designs, the optical window also acts as the X-ray entrance window, and consists of a thin (1.5mm) sheet of Pyrex glass. The light diffusion boxes are formed from a thin plastic sheet of low X-ray attenuation, coated with a highly reflective white paint. Each of the eight modules is viewed by two 90mm photomultiplier tubes set in coincidence by the detection electronics. The use of two photomultiplier tubes to view each primary module was necessitated by the large spatial non-uniformities in the light collection. The tubes were individually chosen for their good spectral resolution and their dynode chains optimised for use in scintillator light collection.

Active shielding over the lower 2π steradians is provided by a 5cm thick NaI(Tl) crystals of the same area, each viewed by a single 127mm diameter photomultiplier tube. The primary and veto crystals are optically isolated from each other and set in anticoincidence by the detector electronics.

The eight individual modules are organised into two blocks of four detectors. Each block is further shielded by a passive graded shield of lead(1mm), tin(1mm) and copper(1mm) with a high efficiency for absorbing photons outside the field of view. On top of each block is a passive collimator consisting of an array of hexagonal copper tubes defining a field of view of about 2 square degrees. In order to reject events derived from the interaction of charged particles in the collimator material and/or the primary crystal, the collimators and the upper half of the diffusion boxes are surrounded by a 10mm thick plastic scintillator anti-coincidence shield. Each of the anti-coincidence systems is viewed by four 52mm diameter photomultiplier tubes.

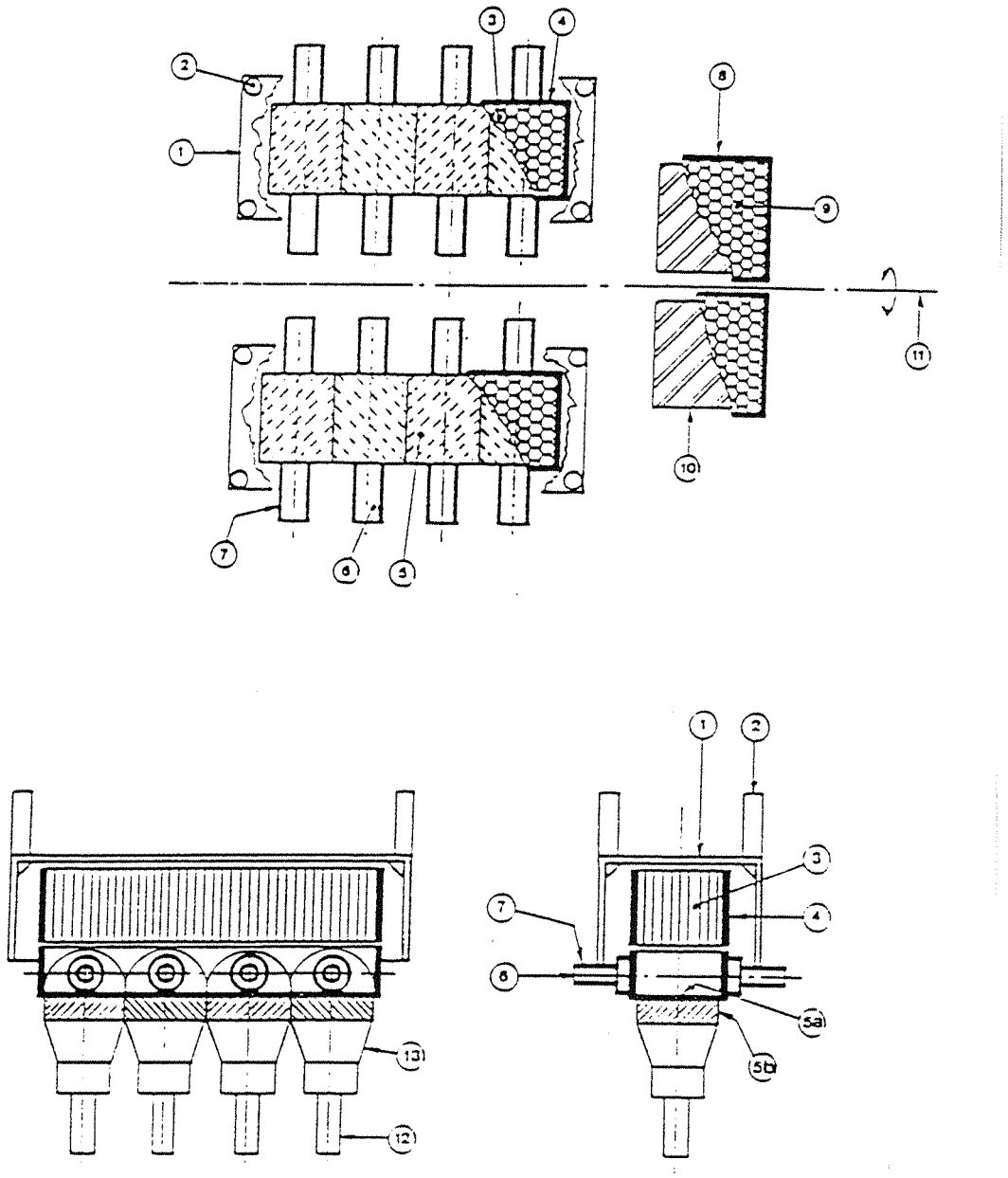

Fig.2.2.The detector configeration of the *MIFRASO* telescope. (a)(1) Plastic anti-coincidence shield,(2) 52mm PMTs for plastic shield, (3),(9) copper collimators,(4),(8) passive graded shield, (5) detector unit (HED),(6) 90mm PMTs for HED primary NaI crystal,(7) passive lead shield, (10) proportional counter detector (LED), (11) zenith rotation axis, (b) (5a) primary HED 6mm NaI crystal unit,(5b) NaI anti-coincidence shield, (12) 127mm PMTs for NaI anti-coincidence shield,(13) white diffusive light guide. From Baker et al., 1984

2.2.2 The Gas Proportional Counters

To provide higher spectral resolution than that offered by the scintillation detectors over the lower half of the energy range of the telescope, two multi-wire spectroscopic proportional counters are included in the detector array. These lower energy detectors operate over the energy range 15-150 keV with an identical field of view to the scintillator array. Each proportional counter consists of a square stainless steel container with a total volume in excess of 10^4 cm^2 with an aluminium sandwich honeycomb entrance window. The window is 50% transparent to 15 keV X-rays and withstands the internal gas pressure of 10 atmospheres. The internal volume of each detector is divided into 50 cells, at the centre of each cell is a 20μm diameter gold plated molybdenum anode wire maintained at a high positive potential.

Each proportional counter is filled with a gas mixture of xenon-argon-isobutane in the ratio 63% – 28% – 9% at a combined pressure of about 3 bar. This high pressure of filling gas ensures a high an X-ray detection efficiency as possible is provided. A detailed description of the proportional counters is provided elsewhere (Ubertini et al., 1981, Bazzano et al., 1983). In order to minimize the background noise rate, the volumes immediately ajoining the walls and the base of each detector are used as anti-coincidence sections. Furthermore, the anodes of the active volume are placed in anti-coincidence with each other in order to reject all double and multiple events due to Compton scattering of higher energy photons or charged particle interaction. Lastly, the 'escape gate' technique is used to recover the double event due to the K-fluorescence photon emitted by the xenon filling gas (Ubertini et al., 1983).

2.3 The Detector Electronics

2.3.1 Scintillator Electronics

The signals from the two photomultipliers on each of the eight scintillator units are individually shaped and descriminated and then summed and stretched before being discriminated again by a window equivalent to the energy range 15 to 300 keV. 'Good' events are defined by a triple coincidence between the two original discriminator pulses along with the signal from this last discriminator. The events are then further gated by pulses from the relevant plastic scintillator shield. The signals from the anti-coincidence crystals generate two pulses for each event. One is used for the rejection of unwanted Compton events and this pulse length may be varied over the range 0 to 70μs by telecommand in order to optimize the rejection of such events. The second pulse is of fixed length and used to select certain Compton events for analysis. These two Compton pulses, together with the good event strobe and the analogue stretched signal, are sent to the digital electronics system for the selection of both Compton and photo-electric events and for pulse height analysis.

2.3.2 Proportional Counter Electronics

The signals from each anode of the two gas proportional counters are fed into separate low-noise charge sensitive pre-amplifiers. A total of ten amplifiers for each detector as the anodes of each plane are alternatively grouped together in order to have only two amplifiers for each plane. The signals then pass through a pulse shaping circuit before being used to trigger the event selection logic that decides on the validity of each individual pulse. The signals from the groups of anodes are summed before being sent to the pulse height analysis (PHA) electronics.

2.3.3 PHA Electronics

Three types of event from the detector array are selected for pulse height analysis : photo-electric events (total energy deposit) in the scintillators, Compton events (partial energy deposit) in the scintillators and total energy deposit in the proportional counters. Each event is tagged in order to identify from which of the ten detectors it originated. A small number of Compton events from the scintillators are analysed in order to study the effects of instrumental background activity in the scintillators.

After initial selection the amplitude of the various events are analysed by 7-bit analogue-to-digital converters providing 128 channels of pulse height data. A unique 5-bit arrival time is associated with each event providing 32 channels of timing data. The rate at which data is telemetered to the ground is set by telecommand in 6 steps between 24 and 72 kbits per second, providing respective timing resolutions of 0.7 ms and 0.2 ms. The telemetry format also contains housekeeping data which include steering data and monitors of high tension voltage, temperature, pressure and so on. Data security is provided by a single parity bit contained within each 16-bit word.

2.3.4 Ground Support Equipment

The ground support equipment (GSE) consists of a pulse code modulation decoder and an HP 9845 computer for data aquisition, recording and display. The GSE performs two major functions : the pre-flight testing and calibration of the telescope and real time decoding and preliminary analysis of data during the balloon flight. The system provides graphical display of the detector performance, hard copy output and bulk memory storage.

2.4 The Steering System

The steering system of the *MIFRASO* telescope consists of azimuth and elevation drives for the inner detection structure and an active tortion release system to avoid twisting the suspension cables during azimuth maneuvers.

The scintillators and proportional counters are mounted on the detector plane which provides a simultaneous elevation drive for both sets of detector. A resolver-synchro device provides measurement of the elevation angle relative to the gondola frame. Two such devices are used.

Azimuth control is provided by a reaction wheel mounted beneath the central structure together with a 2 axis magnetometer. The magnetometer provides signals proportional to two orthogonal components of the local geomagnetic field. Error signals derived from the magnetometers are used to control the angular velocity of the reaction wheel which in turn produces the torque that is used to control the azimuth angle of the payload.

In order to avoid twisting the suspension cables during movements in azimuth, and twisting due to balloon rotations, a motor is used to drive the suspension through a decoupling bearing in such a way that movement of the reaction wheel is not opposed. The same magnetometer signals are used for this.

A Larse Corporation standard data encoder is used to decode the data received on board the telescope via the telecommand up-link from the ground. This uplink enables the observer on the ground to update on- board steering information (balloon geographical coordinates, source sky coordinates and so on), select the mode of observation (drift or track scans) and to send all necessary commands to both the steering and the detector modules. The on-board processor uses this information, together with its own sidereal clock, to calculate the target angles for both the azimuth and elevation drives. All control of the platform from the ground is performed by a dedicated set of GSE (see section 2.3.4). This system continuously displays steering and housekeeping information that is telemetered to ground separately from the PCM bitstream.

The complete steering system was designed to provide a pointing accuracy of $1/3^{o}$ and a stability better than $10'$ with a payload weight of up to 2000 kg. New sky positions were able to be acquired in typically one minute. The final gondola flight configuration weighed approximately 1600 kg. and the above characteristics were confirmed during the first flight of the telescope in June 1982, and again on subsequent flights.

2.5 Detector Response

The efficiencies of both detector systems have been measured using several radioactive sources over their full operating ranges and the results are shown in Fig.2.3. For the scintillators, the efficiency below 40 keV is reduced by the combination of absorbtion in the material in the field of view and the low energy electronic threshold. The proportional counters have less material in the field of view and hence a higher efficiency at lower energy. At higher energies the efficiency of both detectors falls due to the decreased probability of photon absorbtion in the detector.

The energy resolution has been measured at various energies for both types of detector and is shown in Fig.2.4 for an incident spectrum of 241Am a calibration source. Gain values have been normalised. To demonstrate the superior resolving power of the proportional counters, Fig.2.5 shows the separation of peaks due to ^{109}Cd at 22 keV and ^{133}Ba at 33 keV.

During the flights of the balloon, the gains of each detector were periodically checked by moving ^{214}Am sources into the field of view of the detectors by telecommand. The sources normally resided in lead shields and did not contribute significantly to the background counting rate. Gain stabilities can be measured to better than 1% using this arrangement.

The first flight of the payload took place from Palestine, Texas, U.S.A. in June 1982, dur-

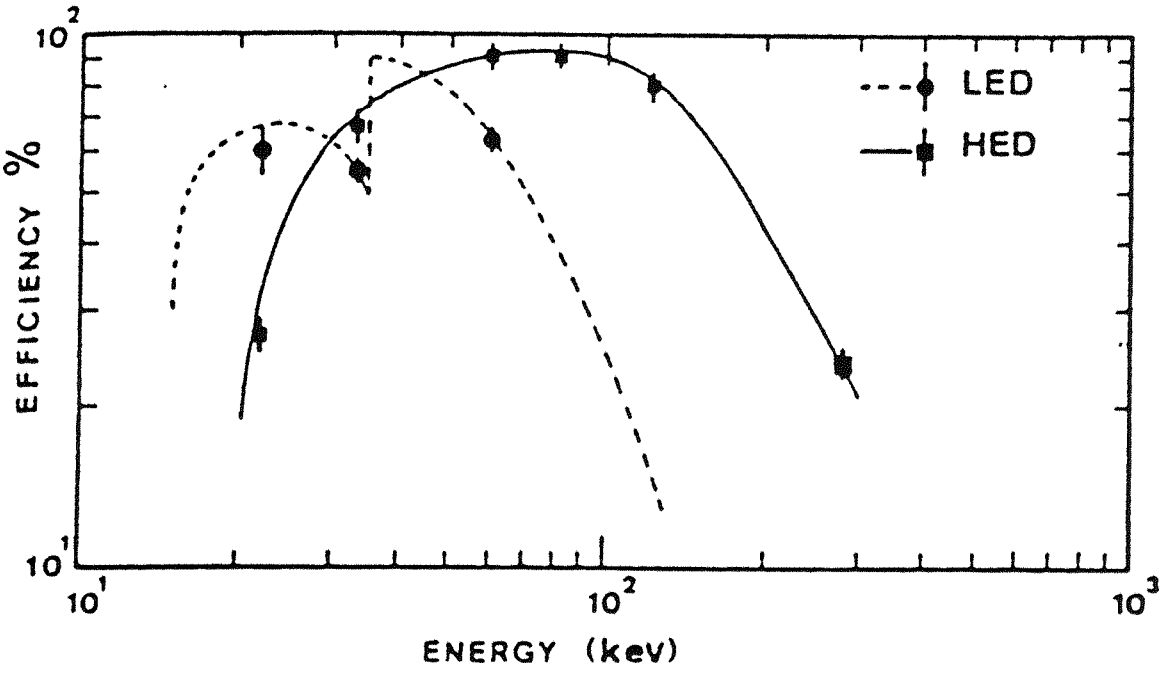

Fig.2.3. Efficiencies of both the high energy (HED) and low energy (LED) detectors of the *MIFRASO* telescope. From Baker et al., 1984.

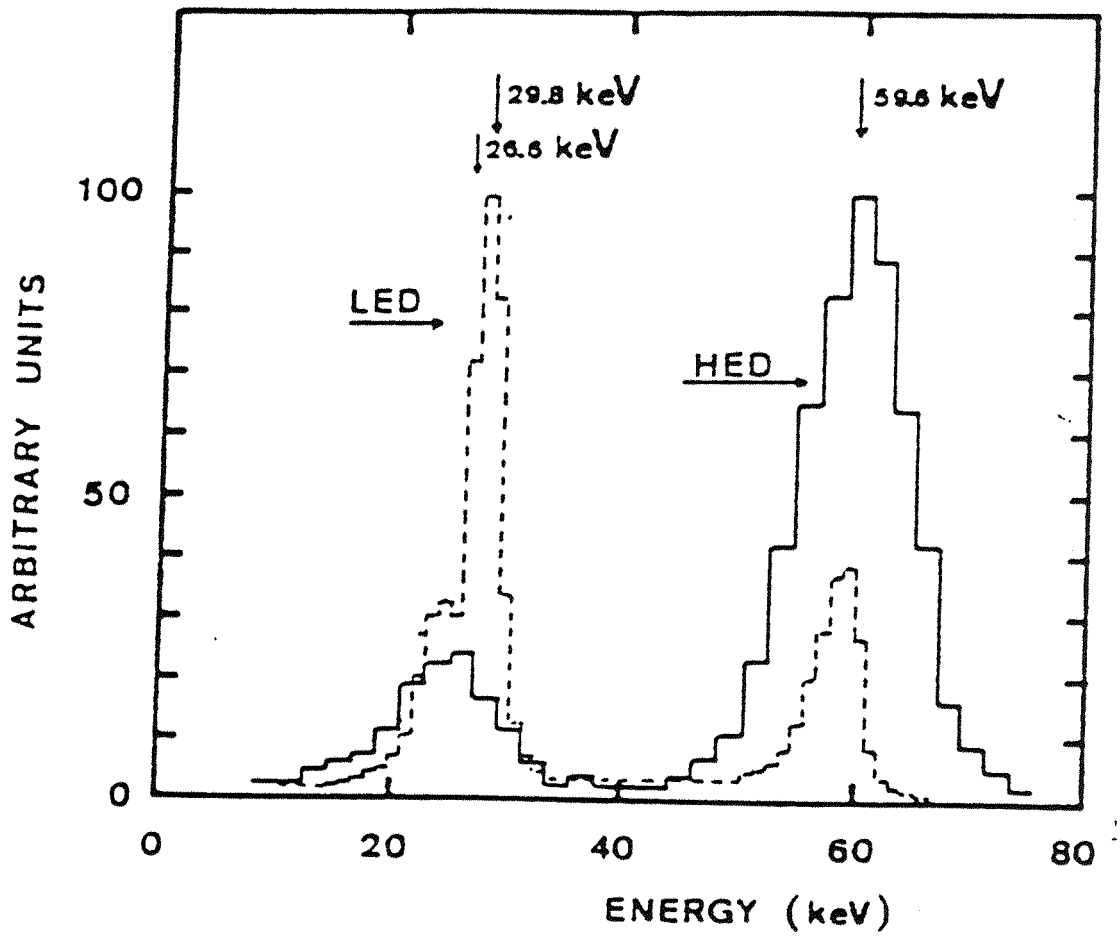

Fig.2.4. Energy resolution of both the high energy (HED) and low energy (LED) detectors of the *MIFRASO* telescope. From Baker et al., 1984

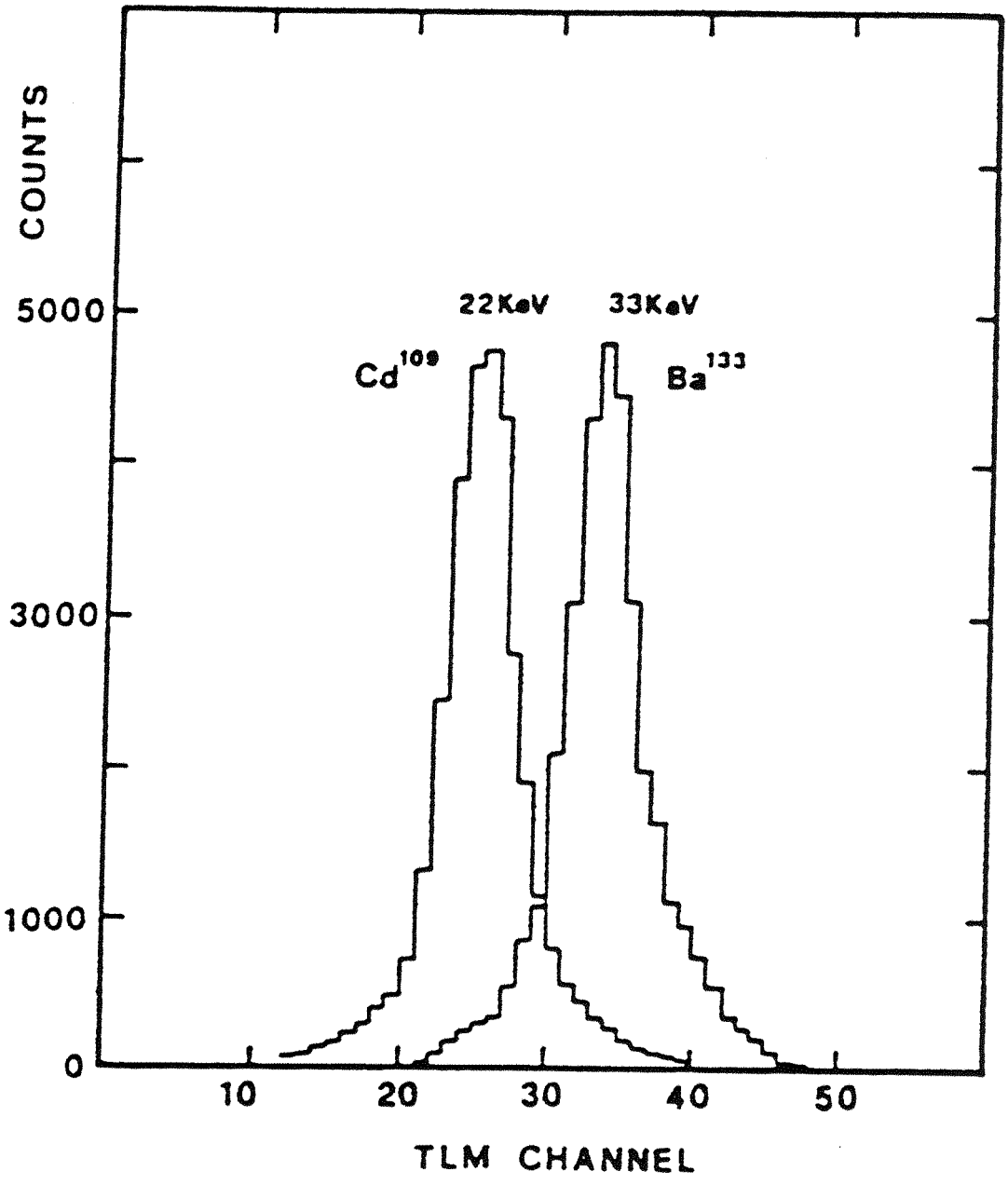

Fig.2.5. The spectra of ^{133}Ba (33 keV) and ^{109}Cd (22keV) measured by the low energy *MIFRASO* detectors shown superimposed to demonstrate the quality of the LED resolution at low energies. From Baker et al., 1984.

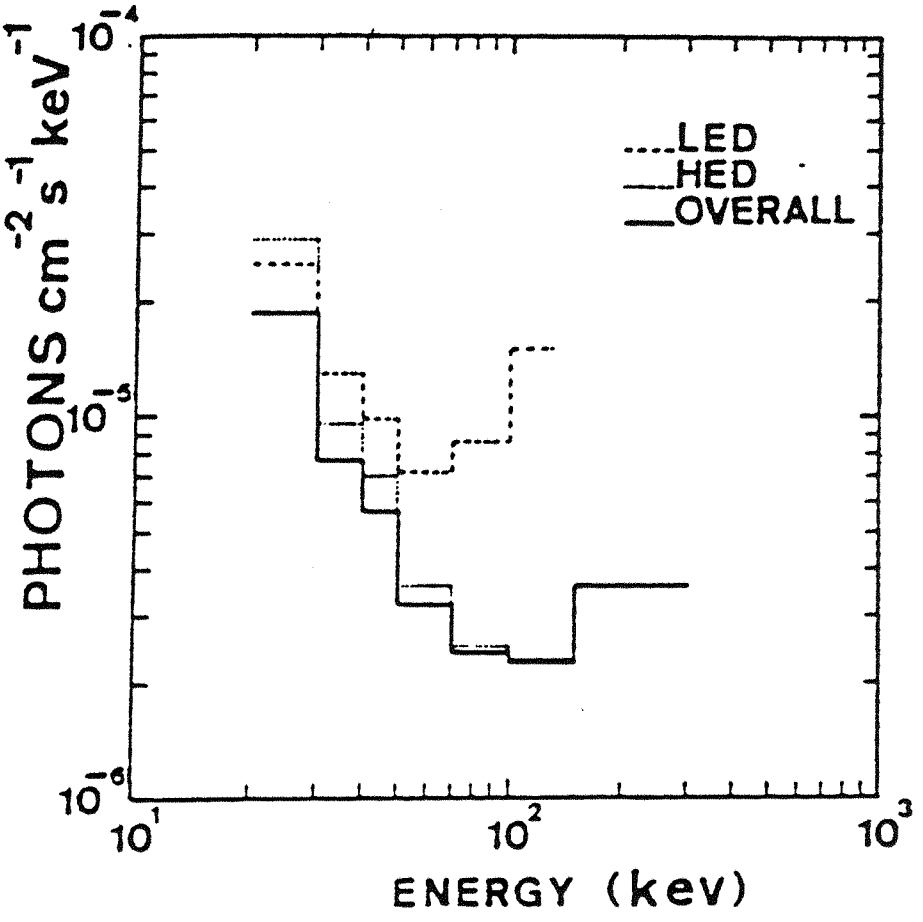

Fig.2.6. Sensitivity curves for both the high energy (HED) and low energy (LED) detectors on the *MIFRASO* telescope. From Baker et al., 1984.

ing which the *MIFRASO* telescope reached a ceiling altitude of 3.5 mbar and made substantial measurements of the background instrumental hard X-ray flux. Using these measurements, overall sensitivity curves for both the high and low energy detectors were calculated and are shown in Fig.2.6. The curves represent the 1 standard deviation minimum flux level that can be detected during a tracking mode observation of 2 hours on source together with an equal time on background measurement, at an altitude corresponding to 3.5 mbar residual atmospheric pressure. For comparison, Fig.2.7 shows spectra of some typical galactic and extragalactic sources superimposed on the *MIFRASO* sensitivity curve.

2.6 Pre-Flight Calibration

2.6.1 Magnetometer Calibration

The two flux-gate magnetometers perpendicularly mounted on the *MIFRASO* payload provide signals which are proportional to the horizontal component of the Earth's magnetic field. A magnetic map of the area of the flight path stored digitally on the payload enables absolute measurements of geographic north to be made. However, the magnetometer signals have to be calibrated before launch with correction curves derived from the interaction of the payload with magnetic north. To this end the payload is rotated through 360^o in steps of 5^o from magnetic north at the launch site and the offset signals from each magnetometer recorded and stored in the steering software. The signals from the corrected magnetometers are also used to define the azimuth pointing direction of the payload. The signals are converted into a digital angle which is compared to the demand angle calculated by the steering software and a position error signal is produced. Rotation of the payload beneath the balloon is achieved using this error signal to drive the reaction wheel mounted in the steering module. In addition, the error signal is fed to the upper tortion relief motor to prevent twisting of the suspension cables.

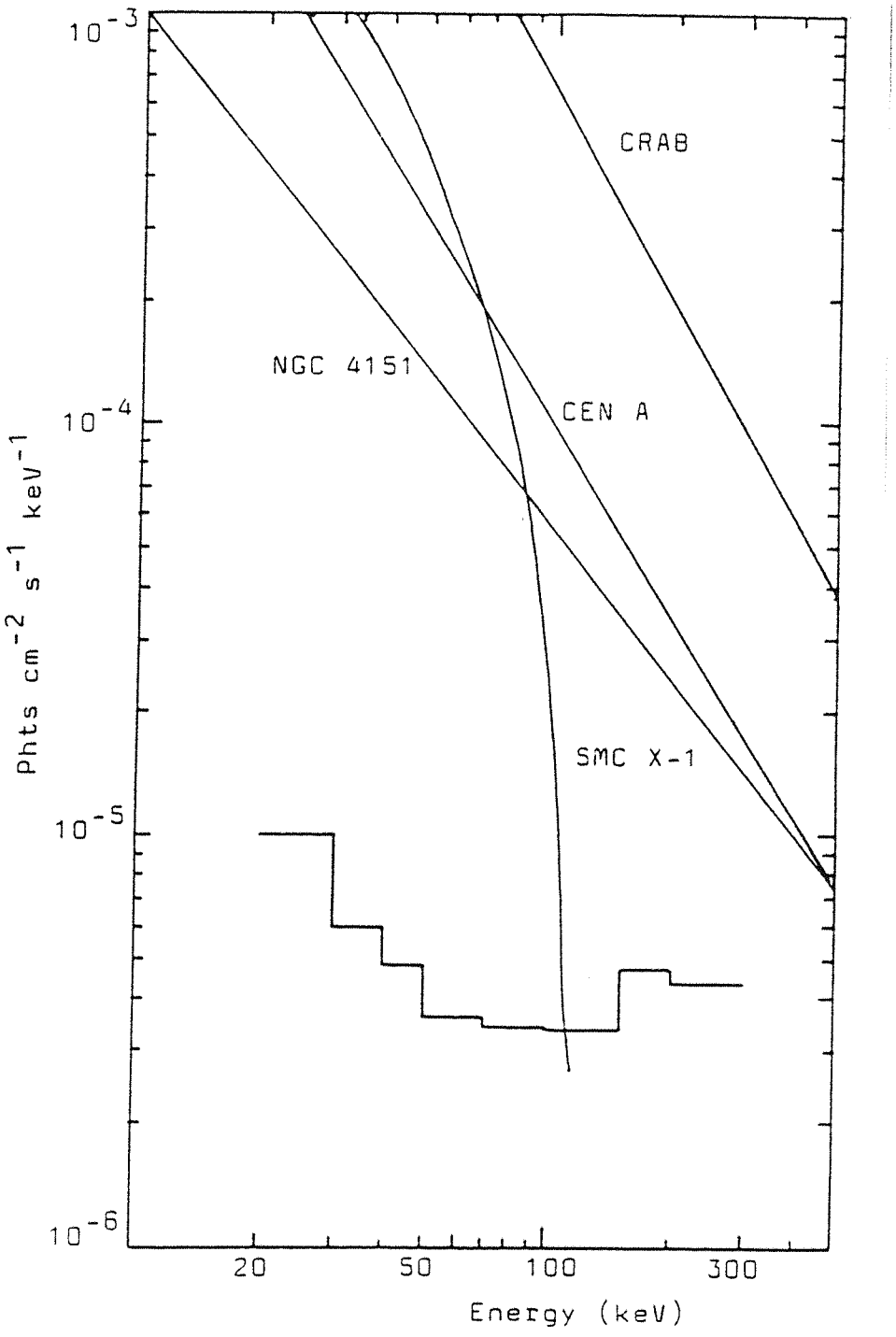

Fig.2.7. The 1 standard deviation minimum detectable flux for the total *MIFRASO* telescope for 10^4 seconds on source. Several sample source spectra are shown for comparison. From Lewis, 1984.

2.6.2 Detector Calibration

The detectors are calibrated prior to launch using six radioactive sources of known line emission. This provides calibration over the entire range of the detectors. Further in-flight calibrations using single ^{214}Am sources are made during the flight of the *MIFRASO* telescope. Fig.2.8. shows a calibration curve that enables the PHA values to be converted into energy for one of the scintillator detectors.

2.7 Balloon and Groundstations

The balloon used to lift the *MIFRASO* payload was a 830000m^3 balloon manufactured by the French *ZODIAC* company. Total mass of the payload was 2060 kg.

For the flights in 1986, 1987 and the unsuccessful launch of 1989 the balloon was launched from the Milo-Trapani base, Sicily (38^o 01'N, 12^{o}35'E) under the auspices of the French ballooning project *ODISSEA* which is run from the CNES, Toulouse, France. The flight path of the balloon took it across the Mediterranean to cutdown over Spain. Groundstations en route were located at La Palma (39^{o}36'N, 02^{o}41'E) and El Arenosillo, Spain (37^{o}06'N, 06^{o}44'W). Recovery of the payload was carried out by INTA, Spain.

The author played no part in the construction of the *MIFRASO* telescope, that had been completed several years earlier, but instead played a major role in the analysis of flight data that were to arrive after the successful flights of the telecope that took place during 1986 and 1987. A suite of data analysis programs were written by the author to access the fine timing capabilities of the telescope. The operation of these programs is described in the following chapter.

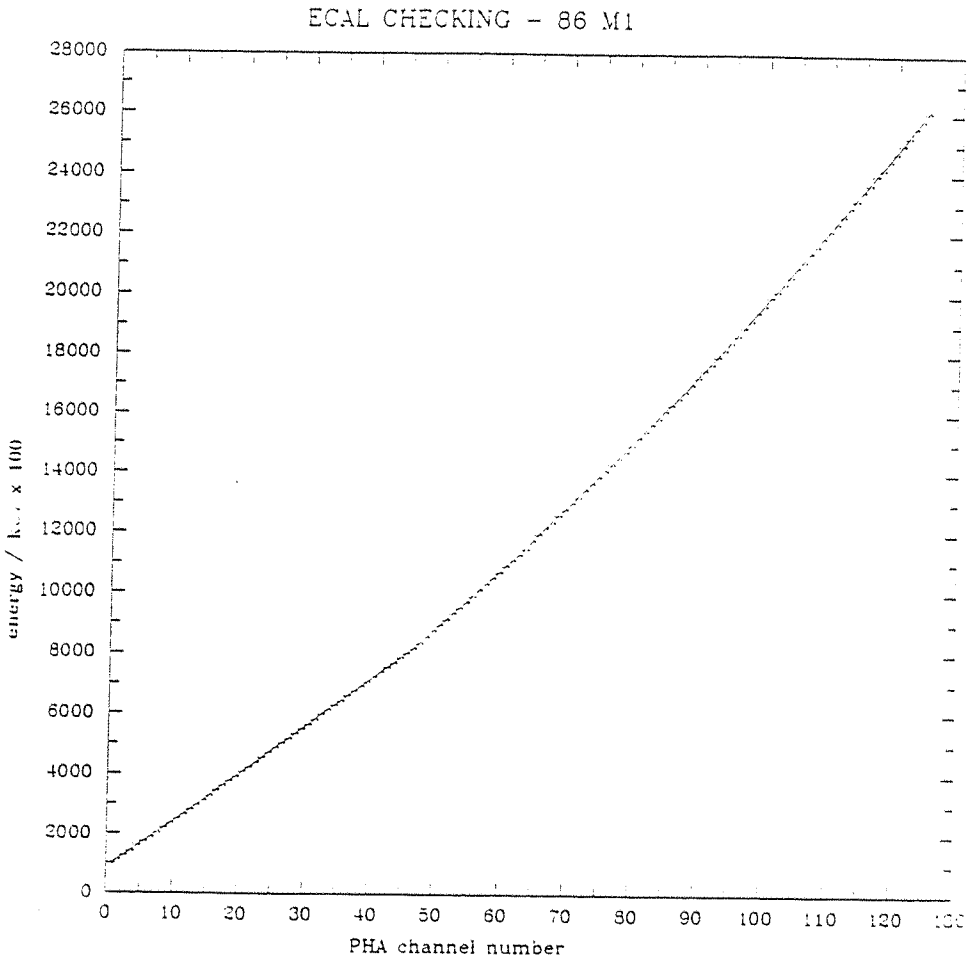

Fig.2.8. A calibration curve for one of the high energy detectors on the *MIFRASO* telescope (detector number 1).

CHAPTER 3 : THE REDUCTION OF *MIFRASO* DATA

3.1 Introduction

This chapter describes the initial process of reducing the *MIFRASO* data from the raw flight tapes in order to extract the event timing and spectral information. The author was primarily responsible for the timing analysis of the *MIFRASO* observations, in particular the observation of the binary X-ray source A0535+26 together with, of course, the Crab Pulsar. Original timing routines written by the author were used by Coe in the analysis of the A0535+26 observation (Coe et al., 1990) to search for the pulsed signature and to derive the pulse profile (see section **4.2**). Other, more sophisticated routines were developed by the author in order to extract the fast timing (0.33ms) information recorded by the *MIFRASO* telescope during the observations of the Crab Pulsar. Results of this work are presented in Chapters 7 and 8.

3.2 Data Aquisition and Recording Format

The *MIFRASO* telescope uses a hard-wired pulse coded modulation (PCM) system for data formatting. CMOS technology is used throughout due to its low power requirements and subsequent saving of battery weight on board the payload. The PCM system can operate at several bit rates between 30 and 72 kbit/s which can be set by telecommand. The higher rates are used for strong sources or cases where high time resolution is required, such as the Crab Pulsar. For this observation, the bitrate was set at 48 kbit/s which then defines the length of the data format and assigns a time resolution of 0.333ms for the recording of individual X-ray events.

The PCM system collects scientific information from each section of the telescope and formats it along with housekeeping information from the steering system into the telemetry format, known as a 'subframe' of data. The subframe format is shown in Fig.3.1. It consists of

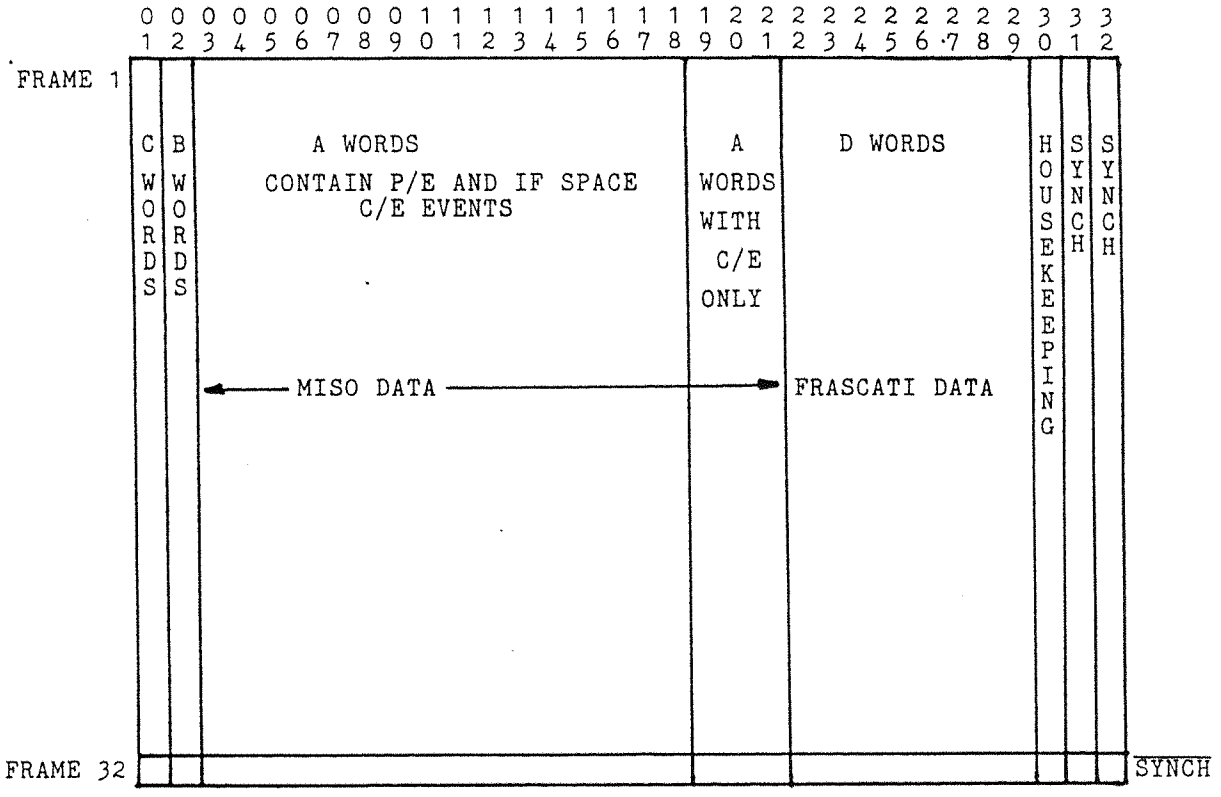

Fig.3.1. The subframe format of the *MIFRASO* datastream. From Lewis,1984.

32 'frames' of data which are, in turn, composed of 32 16-bit words. The principal word formats are shown in Fig.3.2. The least significant bit of each word contains a parity bit so that the quality of each word can be verified before further analysis takes place. Words 3 to 21 of each frame contain the timing and pulse height analysis (PHA) data from the scintillation ('MISO') channels. There are 128 PHA channels for each event. Words 3 to 18 are preferentially filled with photoelectric events and words 19 to 21 contain Compton events. Similar timing and PHA data is recorded in words 22 to 29 for the proportional counters. The first two words of a frame, the C and the B words, record count rates for the proportional counters and the number of each type of event counted and analysed for the scintillation detectors. Word 30 of each frame contains various housekeeping data, such as the anode potentials for the photomultiplier tubes together with temperature and magnetometer readings. The last two words of a frame contain the synch pattern which is used by the computer receiving the data stream to 'lock in' on the formats.

The PCM format is received by two computers at the groundstation. Real time information is available from a Hewlett Packard computer that provides various types of data needed during the flight, for example, energy spectra from the various detectors can be displayed in order to check calibrations. Together with the HP computer, a PDP-11 unit decodes the bit stream and writes all data to magnetic tape for later analysis. The format of the data written to tape is shown in Fig.3.3. Each of the scientific subframes are preceeded by a ground frame record of 4 16-bit words that contain a record counter, which labels each subframe and enables data dropouts to be located, together with a stamp of Universal Time that records the arrival time of the record. This UT stamp is written to a precision of 1ms.

3.3 Data Reduction

Initial data reduction for both spectral and temporal analysis is performed using the

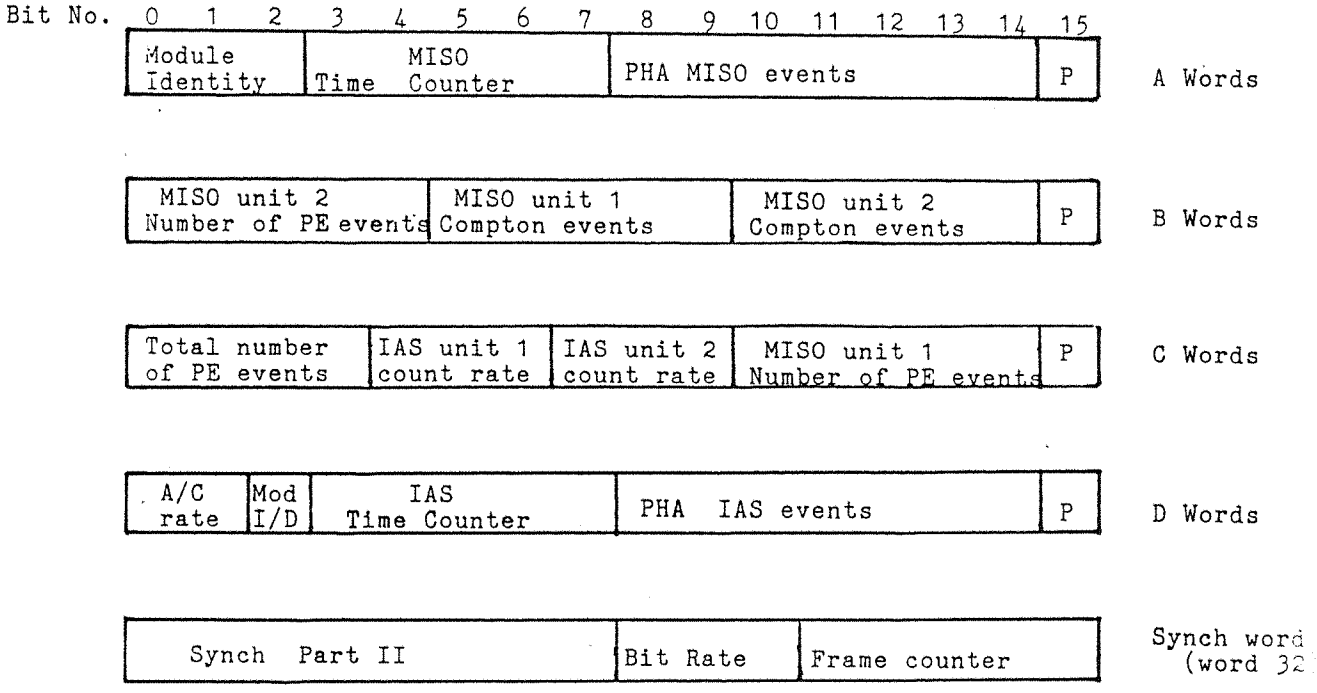

Fig.3.2. Principal word formats of the *MIFRASO* datastream. From Lewis, 1984.

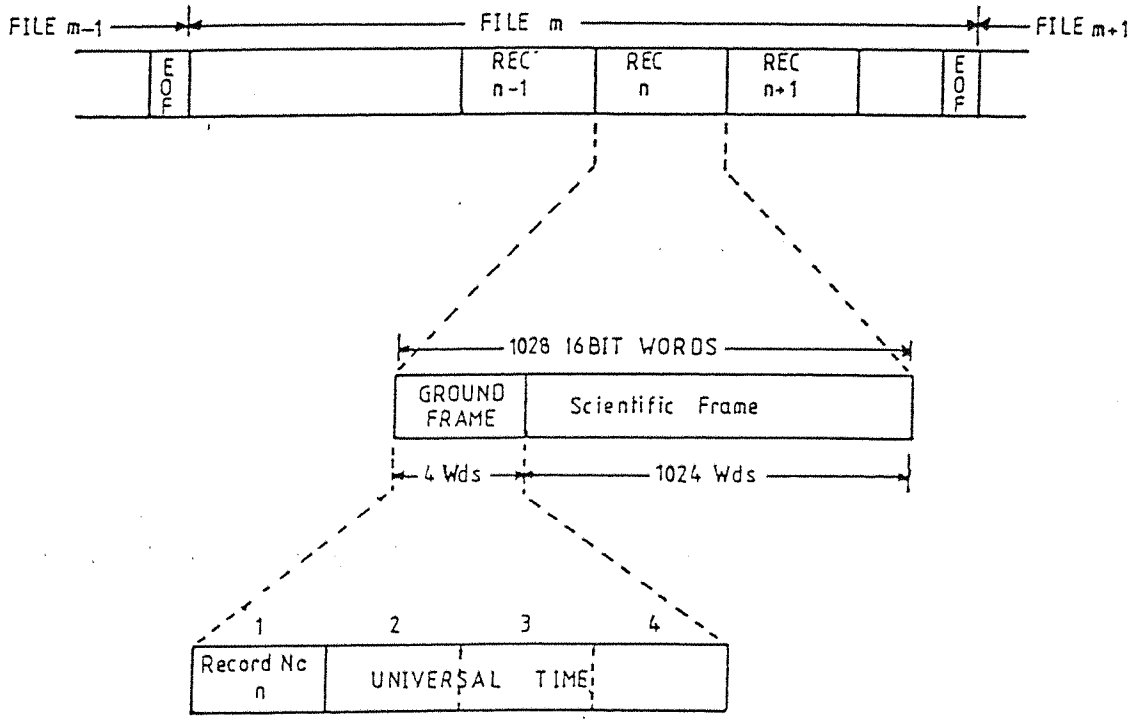

Fig.3.3. Format of the *MIFRASO* datastream written to tape. From Court, 1987.

program FRANZ. This enables blocks of data of the order of hundreds of subframes to be read in and 131 parameters averaged over a specified number of subframes. These flight parameters include the time, altitude, position, countrate of all detectors and the pulse height analysis of each event and the resulting readings are outputted into two files, a texted and an untexted file for subsequent analysis. The averaging facility allows complete observations lasting tens of minutes to be analysed in one program run. A typical run would use 500 subframes, averaging 100 subframe blocks to produce 5 files of averaged flight parameters. The spectral information is then used for deconvolution with the corresponding background measurements. A second program, STRIP, is used to strip out of the untexted file parameters of interest, plot them against time and to allow a graphical display of, for example, altitude against time to be made. Other displays of interest include countrate against time, right ascension-declination plots (to check pointing) and latitude and longitude verses time plots to check the position of the balloon. Fig.3.4 shows the ascent curve of the *MIFRASO* balloon during the 1986 tracking scan of the Crab.

The first step in the analysis of the Crab Pulsar observations is to establish the overall features of the scans, and this is done using the FRANZ and STRIP routines. Fig.3.5a-d show countrate, right ascension-declination, and latitude-longitude plots for the 1986 Crab track observation. FRANZ also has the capacity to reject corrupted subframes when, for example, the parity bit is in error. Data dropout rates during the above observation were of the order of 4%, reflecting the excellent telemetry quality at the start of the flight.

A simple model using detector response and atmospheric attenuation functions was developed to predict the countrate increase expected for an observation of the Crab region. This is presented in Appendix 1.

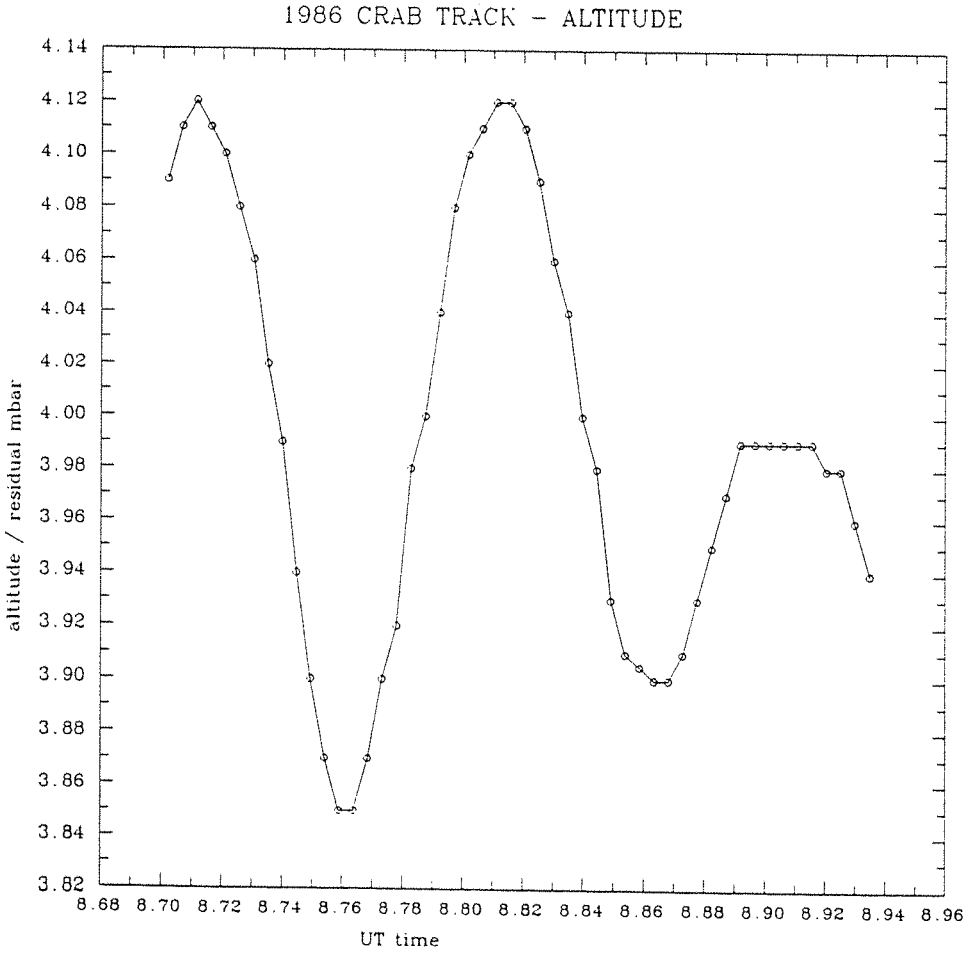

Fig.3.4. Altitude profile during the 1986 tracking scan of the Crab.

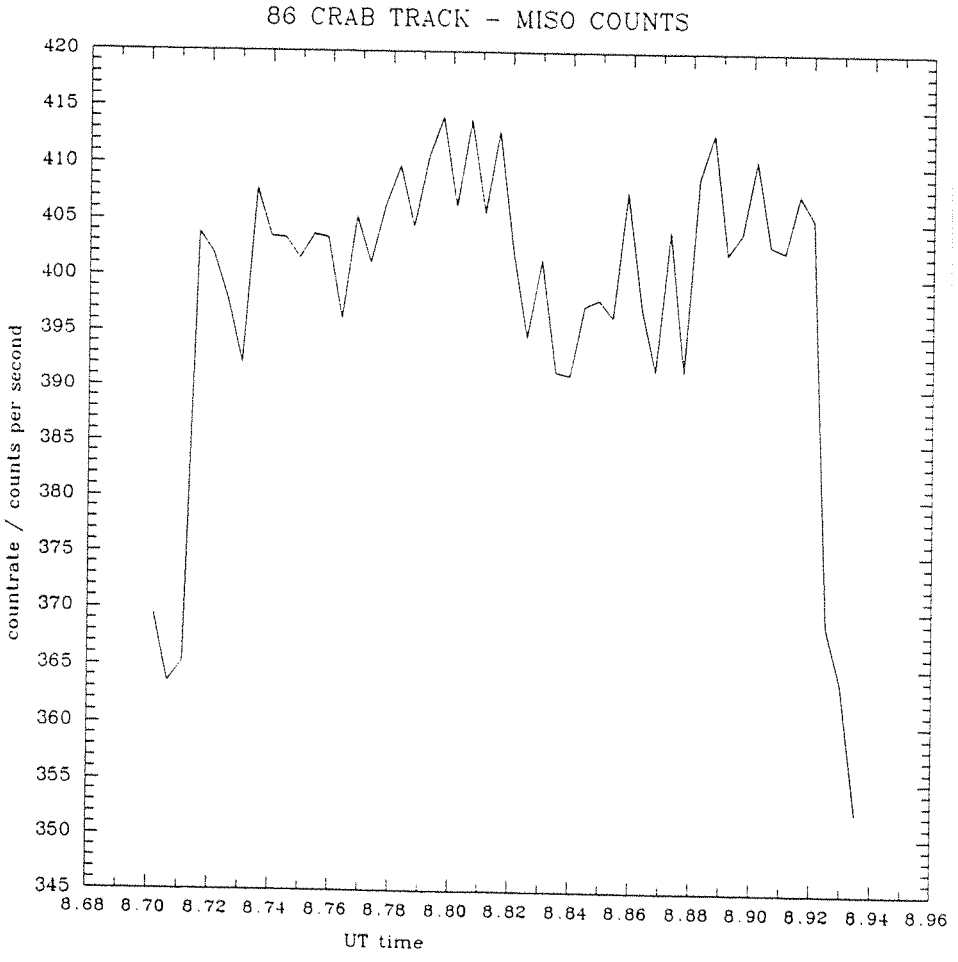

Fig.3.5(a). The countrate profile from one module (four units) of the high energy detectors for the 1986 tracking scan of the Crab.

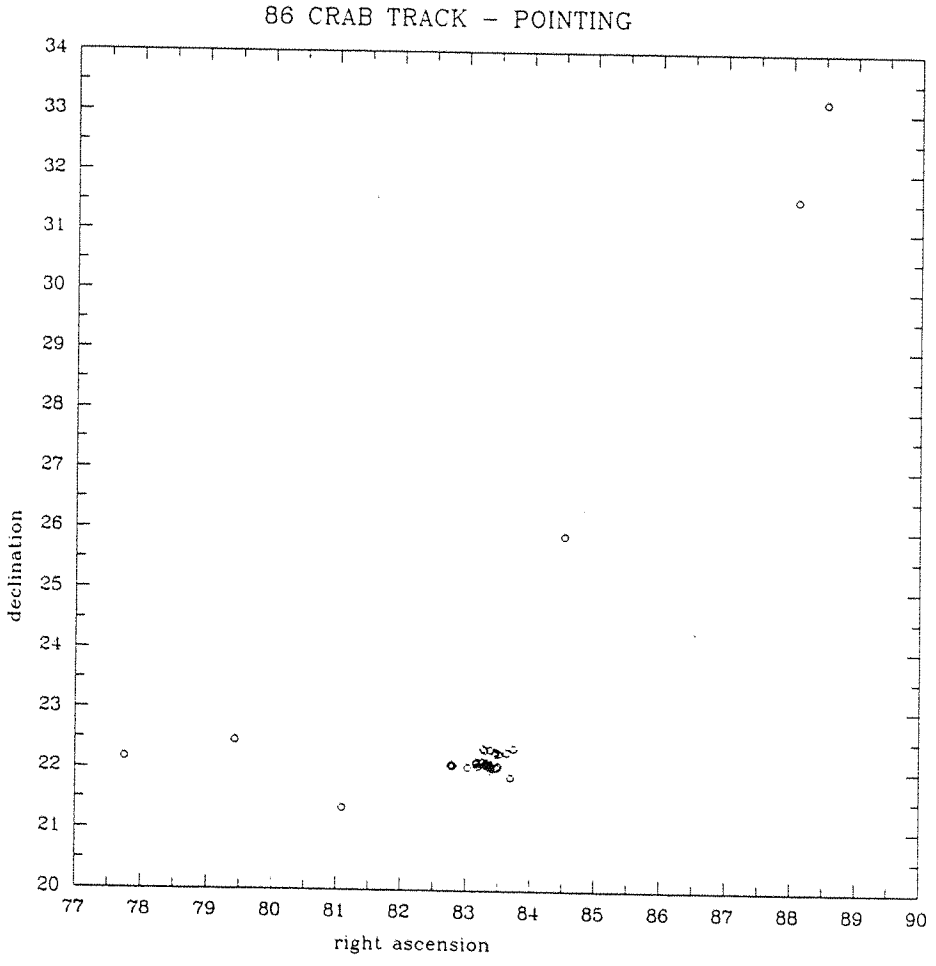

Fig.3.5(b) The right ascension-declination (pointing) plot from the 1986 tracking scan of the Crab.

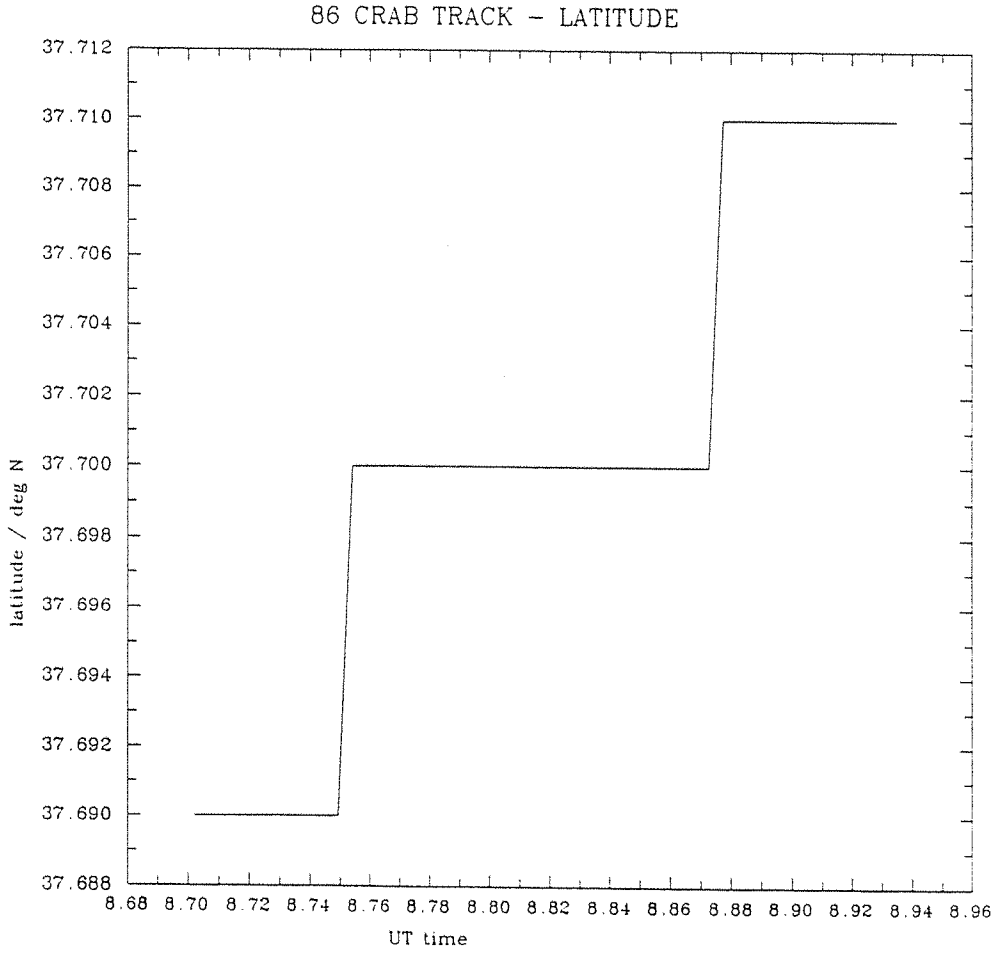

Fig.3.5(c). The latitude profile from the 1986 tracking scan of the Crab.

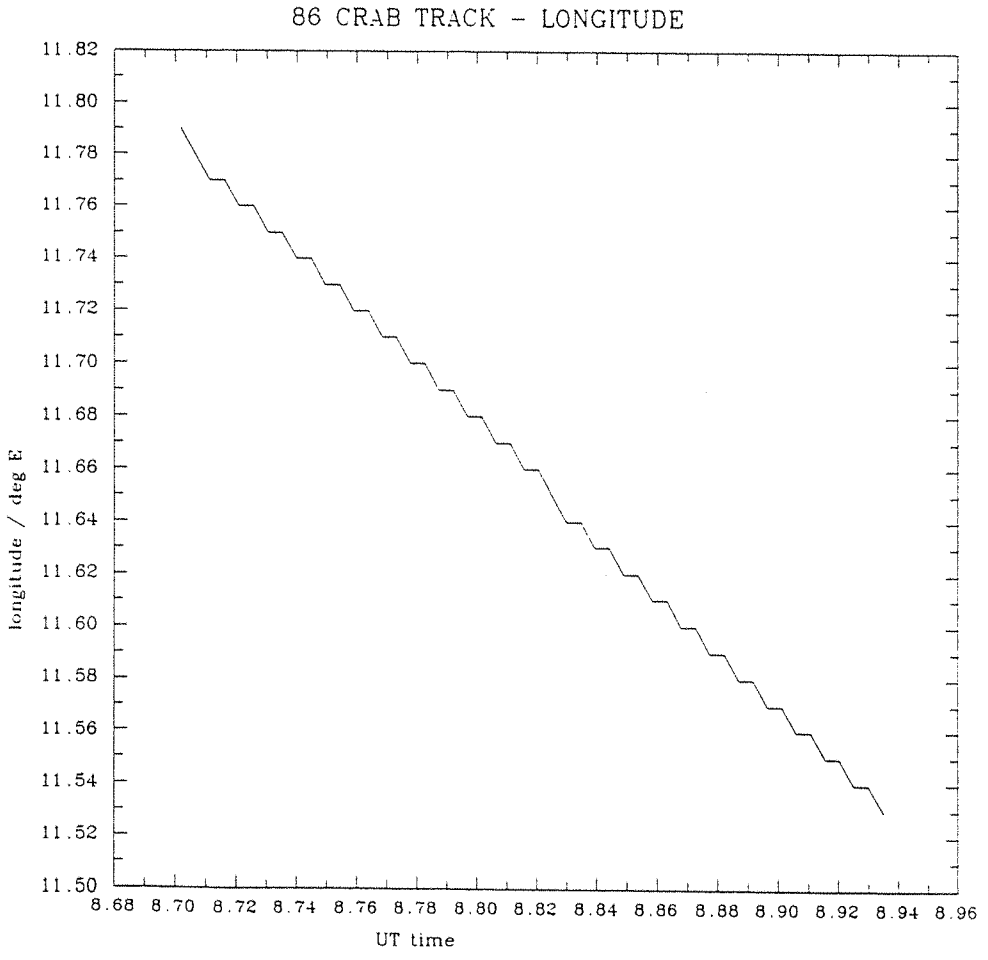

Fig.3.5(d). Longitude profile from the 1986 tracking scan of the Crab.

3.4 Spectral Analysis

All of the spectral analysis for the scintillator detectors was carried out by Dr.F.Perotti of the C.N.R. institute, Milan, Italy, using the conventional techniques of spectral reduction. A response matrix was formed from calibration data of the detectors that converts PHA values from individual detectors into the incident energy of the X-ray photon. The X-ray background is measured before and after the observation and interpolated to a spectrum during the observation by fitting with variations in altitude, position and time. Results from the MIFRASO observations of the Crab Pulsar will be presented in Chapter 8.

3.5 Temporal Analysis

Timing on-board the *MIFRASO* payload is derived from an oven-controlled crystal clock, whilst timing on the ground is derived from a rubidium frequency standard that has previously been calibrated from a national standard atomic clock.

For timing observations of the Crab Pulsar to be successful, the series of events of the arrival times of the X-ray photons on a ms timescale must be reconstructed. This involves examining the data format on its highest temporal resolution, that is, extracting the individual words from the subframe format. From knowledge of the position of the word within the frame, and the length of each word derived from the telemetry bit-rate, the correct arrival sequence can be reconstructed. The C word of each frame contains the total number of photoelectric events analysed within the frame and so by extracting this information the correct number of A words can be read out in reverse sequence, as those photons arriving last are stored first in the A words, see Fig.3.2. After checking the subframe and frame counters, an arrival sequence can be formed from

$$T_{event} = UT + S \times T_{subframe} + F \times T_{frame} + W \times T_{word}$$

where

UT = Universal time read from ground frame record

S = number of subframes incremented

F = number of frames incremented

W = number of words incremented.

The length of a subframe is derived from the telemetry rate of 48 kbit/s:

$$T_{subframe} = \frac{32 \times 32 \times 16}{48 \times 10^3}$$

which equals 0.341s. The frame times and word times are simply divisions of this value. Thus arrival times in UT can be assigned to the individual X-ray photon events. Temporal analysis of the proportional counter data proceeds in the same manner as outlined above. All the above analysis is performed within the routine GET. A second routine, CRAB, takes the raw event times and barycenters them ,that is, removes the effect of the Earth's motion around the Sun (see Chapter 7). Two avenues are now open for temporal analysis, either folding the event times at a known period to produce a series of event phases from which to derive a pulse profile or else outputting the arrival times directly on which to conduct a periodicity search for unknown period (or to confirm a known one). The routine CRAB can perform either one of these tasks. Finally the routine SLICE converts the HDS-stored CRAB data into unformatted records for further analysis.

This chapter has outlined the structure of the timing data analysis software. The following chapter reviews each of the sources from the two flights that the $MIFRASO$ telescope observed, and details the contributions that $MIFRASO$ has made to our understanding of those sources.

CHAPTER 4 : THE SOURCES OBSERVED BY *MIFRASO*

4.1 Introduction

To date there have been two successful flights of the *MIFRASO* balloon-borne hard X-ray telescope: the 29th July 1986 and the 15th July 1987 trans-Meddittерranean flights from Milo-Trapani, Sicily to Spain. A total of nine separate sources have been observed, and the analysis of the data from each observation is now complete. The sources comprise a galactic pulsar (the Crab), galactic binary X-ray sources (Hercules X-1, Cygnus X-1, A0535+26), Seyfert galaxies (NGC 4151, MCG 8-11-11), a quasar (3C273), a galactic cluster (the Coma cluster) and the unusual binary source SS 433. Summary tables of the observations showing the target, start and finishing time are given in Tables 4.1 and 4.2.

This chapter contains a brief discussion of the sources observed (except the Crab Pulsar which is discussed more fully elsewhere), together with a review of the *MIFRASO* observations of each source.

4.2 A0535+26

The X-ray binary system was discovered serendipitously by the Ariel V satellite in 1975 (Rosenberg et al., 1975). It is a pulsating compact object orbiting the Be star HDE 245770 in a highly eccentric orbit. Accretion is believed to be stellar-wind powered with regular X-ray outbursts occurring at periastron passage of the neutron star every 111 days. An ephemeris for these outbursts has been derived from 10 years of monitoring by the Vela 5B satellite (Predhorsky and Terrell, 1983) . The high energy emission (E>20keV) is characterised by a thermal spectrum with a kT value of between 10-20 keV.

A0535+26 was observed in three 15-minute runs between 09h56m and 11h39m UT during the 1986 flight of the *MIFRASO* telescope. The intervening periods were spent tracking two

target	UT start	UT end
Crab track	07.30	07.44
Crab drift	08.55	09.37
A0535+26	09.57	10.11
A0535+26	10.39	10.53
A0535+26	11.25	11.39
NGC 4151	11.55	12.12
NGC 4151	12.47	13.04
NGC 4151	13.43	14.00
3C273	14.35	14.48

Table 4.1. The targets for the 1986 flight of the *MIFRASO* telescope. Launch date was 29th July 1986.

target	UT start	UT end
Crab drift	08.02	09.52
MCG8-11-11	09.54	12.28
NGC 4151	12.30	15.14
3C273	15.16	18.24
Coma	18.26	20.18
Her X-1	20.20	22.30
SS 433	22.32	01.16
Cyg X-1	01.16	02.19

Table 4.2. The targets for the 1987 flight of the *MIFRASO* telescope. Launch date was 15th July 1987.

blank parts of the sky 3.5 degrees away in right ascension from the target, but having the same declination, and using the same sequence of steering maneuvers used to track the source. This method of observation is designed to minimise possible systematic background variations related to changes in telescope azimuth or elevation. The background observations were used to monitor the instrument's background counting rate as a function of altitude, latitude, longitude and photon energy. From knowledge of the off-source background measurements and their variation with altitude, latitude and longitude, on-source background measurements were interpolated and subtracted from the on-source count-rate, leaving a count- rate measurement of the source. In addition, there was a small amount of collimator leakage above 100keV from the Crab. The amount was estimated from the known collimator response and the Crab energy spectrum, which had been obtained just prior to the A0535+26 observation, and subtracted from the observed spectrum.

Fig.4.1 shows the deconvolved photon energy spectrum, interpreted as originating from the direction of A0535+26. Also shown is the corresponding flux from the Ariel V observation, taken whist the source was undergoing a major outburst (Coe et al, 1975). The *MIFRASO* observation shows a weak flux detected in the scintillation counters at a level of just under 4σ. Due to the smaller sensitive area, no excess signal was found in the proportional counters. Model-fitting to the data gave acceptable fits either for a power-law spectrum of photon index $-2.1^{+1.7}_{-1.1}$ or thermal bremsstrahlung of temperature given by $kT=66^{+101}_{-31}$ keV. Errors are given at the 1σ level for the joint variation of two parameters (Avni 1976).

A conventional timing analysis was also performed to search for a pulse signature in the energy window 32-52 keV (Coe et al., 1990).

Using the ephemeris of Priedhorsky and Terrell (Priedhorsky and Terrell 1983) it may be calculated that the *MIFRASO* observations took place at binary phase 0.25 ± 0.08 where phase 0.0 is periastron and the brightest point in the average 3-12 keV X-ray flux profile. The

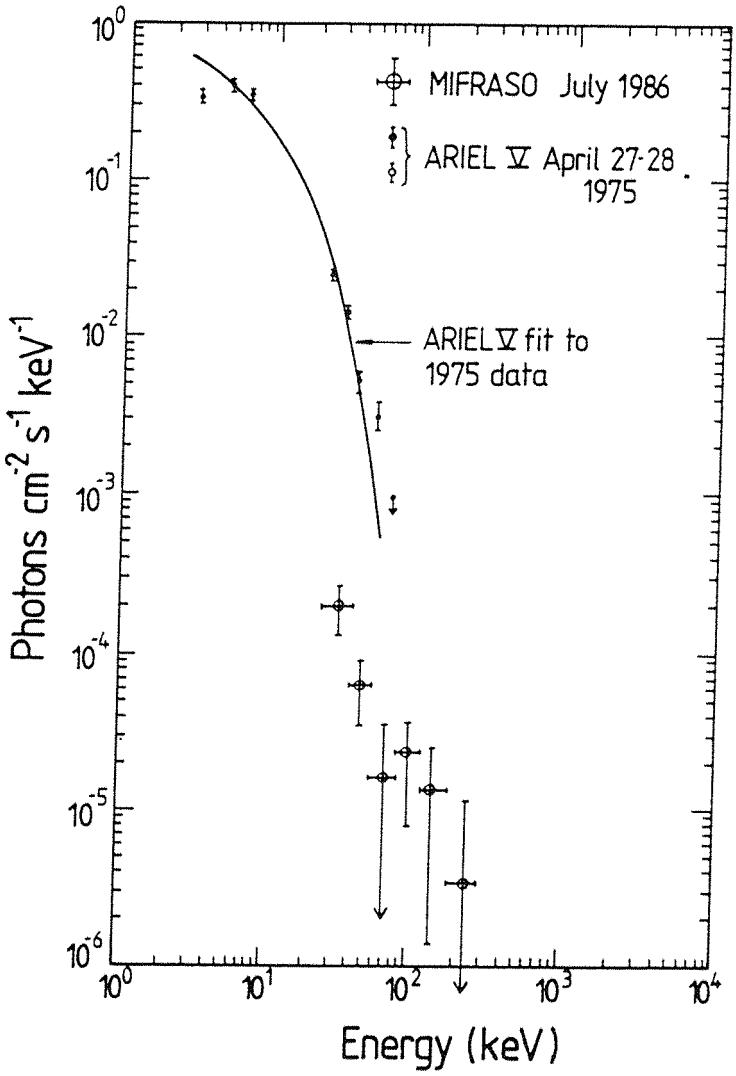

Fig.4.1. The deconvolved energy spectrum from A0535+26. Also shown is the corresponding flux from the Ariel V observation. From Coe et al., 1990.

flux level recorded by the *MIFRASO* telescope is two orders of magnitude lower than that reported by the Ariel V observation in 1975 and is an order of magnitude beneath that reported by all other observers in the 30-100 keV band - except the detection by Polcaro et al. in 1983. Since the neutron star was well past periastron during the *MIFRASO* observations, it is to be expected that the amount of material available for accretion would be very low. The spectral parameters derived from the *MIFRASO* observation suggest a hotter temperature than usual, but the large uncertainties mean that lower, more normal values cannot be excluded.

4.3 NGC 4151

The Seyfert galaxy NGC4151 was observed between 11.58 and 14.20 UT during the 1986 flight of the *MIFRASO* telescope, the observation time being divided into three segments (Perotti et al., 1990) . In order to minimise possible background variations related to changes in elevation and/or azimuth, for each of the three segments, the background spectrum was evaluated before and after the observation of the source. A point having the same declination but a right ascension alternatively 4.2 degrees lower and higher than of NGC 4151 was tracked using the same sequence of steering manoeuvers as was used to track the source. Thus the time devoted to the background evaluation was twice the time devoted to study the galaxy. The total integration time of useful data on source was 2700 s.

The stability of the energy response of the instrument was found to be within ± 0.8 % during the course of this observation. Correlations between the background counting rate and potential sources of systematic variations such as altitude, longitude, latitude, azimuth and elevation were investigated so that an appropriate correction to the background noise subtraction was possible for each period of on-source observation time. The only source of systematic background variation was found to be related to the residual atmospheric depth changes between 4.0 and 4.4 g/cm^2. This effect was correspondingly reduced to a level considerably below the level

of statistical fluctuations.

An excess count-rate spectrum, interpreted as originating from the direction of NGC4151, was detected in the energy band 27-80 keV of the scintillator detectors with a statistical significance of 5.5σ and a corresponding signal-to-noise ratio of about 1.5%. No detectable changes in the source countrate spectrum were found during the observation. Due to the smaller sensitive area, no significant excess above the background was found in the proportional counters.

The corresponding photon spectrum, evaluated using the same procedure as for the other sources and under the assumption of a power-law emission from the source, is given by

$$\frac{dI}{dE_x} = (8.6 \pm 2.2) \times 10^{-5} (E_x/50)^{-1.5 \pm 0.6} \text{ photons cm}^{-2} \text{ s}^{-1} \text{ keV}^{-1}$$

with a reduced chi-squared value of 0.3 for 10 degrees of freedom. Errors given are at the 1σ level for the joint variation of two parameters. A single parameter estimation at the same confidence level gives an error of 0.27 on the spectral slope and of 8×10^{-6} on the intensity constant.

Fig.4.2 shows the *MIFRASO* photon spectrum from the 1986 flight together with two other representative hard X-ray measurements of the source.

Most of the hard X-ray observations from 1972 up to 1979 have been recently reviewed (Baity et al., 1984), from that year up to the *MIFRASO* observation in 1986 only one hard X-ray measurement has been performed by the HXR-81 balloon borne telescope in 1981 (Ubertini et al., 1984). A comparison of all available data indicates that *MIFRASO* observed NGC4151 during a period of normal activity. The *MIFRASO* observation gives a 100 keV flux value of $(3.0 \pm 1.1) \times 10^{-5}$ ph cm^{-2} s^{-1} keV^{-1}, where the single parameter variation best fit has been used to extrapolate to high energy for the sake of consistency with all other data. The weighted average of all 100 keV flux values from past observations gives $(2.9 \pm 0.13) \times 10^{-5}$ ph cm^{-2} s^{-1} keV^{-1}. Despite the source intensity changing substantially (a factor of 4.6 ± 2.4 maximum to minimum and a factor of 1.8 ± 0.5 over a six month period), the pattern of the variability is not

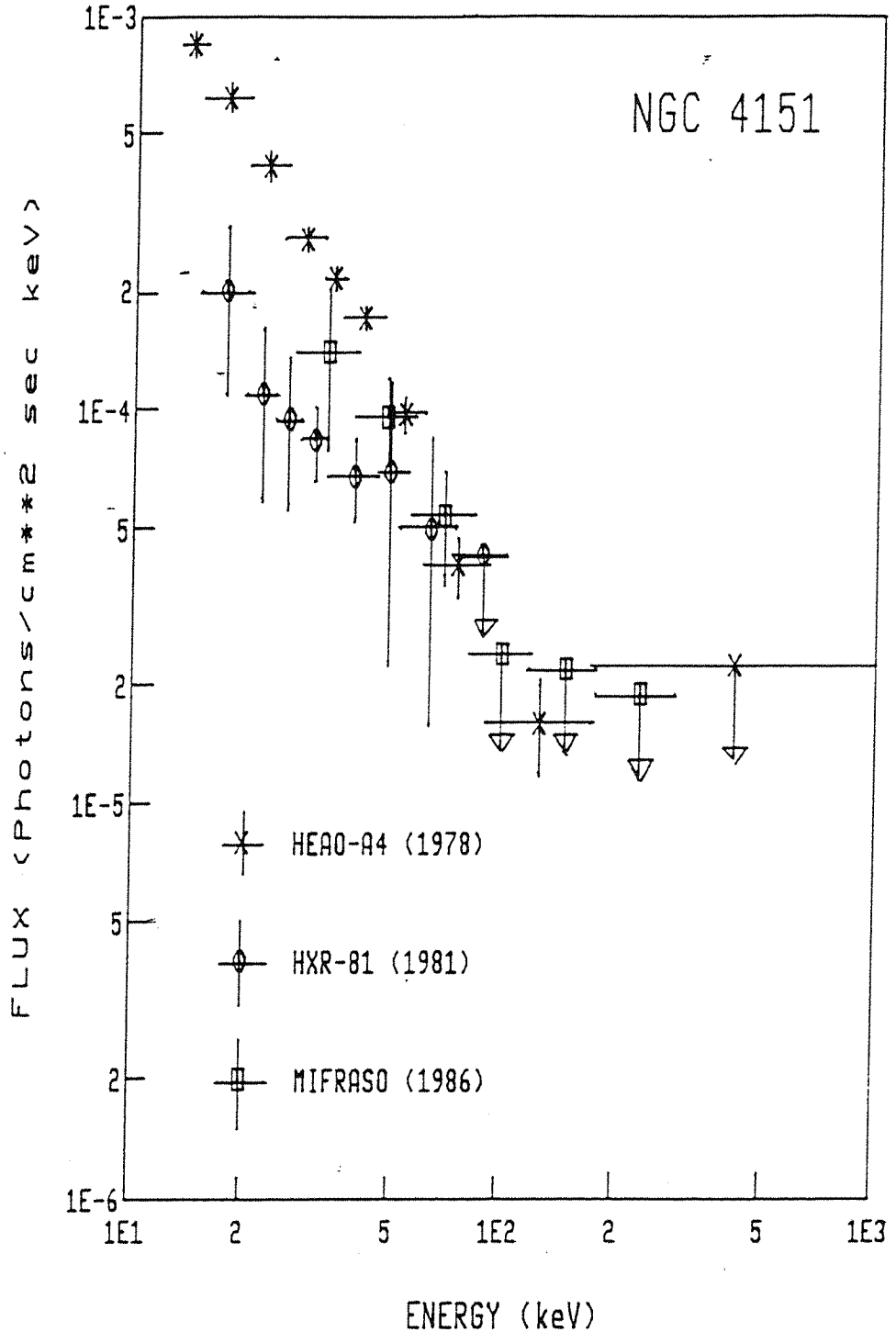

Fig.4.2. The deconvolved energy spectrum from NGC 4151 as observed from the 1986 *MIFRASO* flight. Also shown are two other representative measurements of the source. From Perotti et al., 1990.

yet clear. There is some evidence in the data that the source jumps between two discrete levels as opposed to a continuum of intensity levels.

Above 20 keV the spectrum of NGC4151 is dominated by a hard power law continuum, the intensity of which can vary by a factor of 2-5 with a possible bimodal pattern. The time averaged spectral slope is 1.37 with evidence for occasional departure from this value. This behaviour is slightly different from that found in the soft/medium X-ray range (3-20 keV) where the observations are far more numerous and detailed: a factor of up to 10 variations in intensity have been observed whereas the spectral index remains close to a weighted average value of 1.55 ± 0.04 (Yaqoob et al., 1989). The two sets of data indicate a tendency for the mean spectrum of the source to flatten going from soft to hard X-ray energies. It is interesting to note that earlier *MISO* observations of this source (Perotti at al., 1979 and 1981), which covered a wide energy band up to a few Mev, are in substantial agreement with this picture. If the spectral slope change is a result of two power law mechanisms at work, the flatter of which dominates at higher energies, then it is not surprising that a different behaviour in the two energy bands is seen. Alternatively, an intrinsic change of slope is being witnessed, probably due to the onset of high energy related processes. In any case, observation of a pivot point may help to distinguish between the two alternatives.

4.4 MCG 8-11-11

The Seyfert galaxy MCG 8-11-11 was observed for a total of 3200 seconds of useful on-source data between 10.40 UT and 12.40 UT during the 1987 flight of the *MIFRASO* telescope. Corresponding background measurements were made for a total period of 2900 seconds. These background measurements were made using the same sequence of steering manoeuvers as those used to track the source, but performed on a region of sky 4.6 degrees in right ascension away from the source but having the same declination. This method has the advantage of minimising

systematic errors due to elevation and azimuthal changes. During the course of the observation, the atmospheric depth varied between 4.0 and 4.3 g/cm^2 with a mean value of 4.1 g/cm^2 during the source tracking period. The variation of the background noise with atmospheric depth was not more than 1% during the course of a single observational segment. A series of calibration checks using the on-board Am^{241} sources found the energy response of the telescope to be stable to within $\pm 0.8\%$ during the course of the observation.

The observation sequence was arranged so that approximately equal time periods were devoted to source and background measurements. The total period was split into 3 segments of background and 3 source observation intervals. Correlations between the background counting rate and potential sources of systematic variations such as position or altitude were investigated. During the background periods the count rate correlation with residual depth was carefully estimated so that an appropriate correction to the background noise subtraction could be made for each on source period, thus reducing this, the major source of systematic error, to below the statistical level. The only measurable source of error was found to be related to altitude changes, but the effect was at a level considerably below statistical fluctuations. The orientation axis of the telescope with respect to the direction of MCG 8-11-11 was estimated and found to be less than 0.1 degree. The precision of the orientation platform pointing was verified during the course of the balloon flight by means of drift scan observations of the Crab and Cygnus X-1.

An excess power law spectrum was obtained from the observation of MCG 8-11-11 and is shown in Fig.4.3. The statistical significance of the observation was found to be 3.2σ in the 31-95 keV band. The photon spectrum was produced under the assumption of a power-law emission from the source. Deconvolution of the atmospheric attenuation with the detector response function has been checked and its precision confirmed by observations of the Crab region. The best power law spectrum was found to be

$$\frac{dI}{dE_x} = 6.1^{+3.0}_{-2.8} \times 10^{-5} E_x^{-1.94+1.56}_{-1.26} \text{ photons cm}^{-2}\text{ s}^{-1}\text{ keV}^{-1}$$

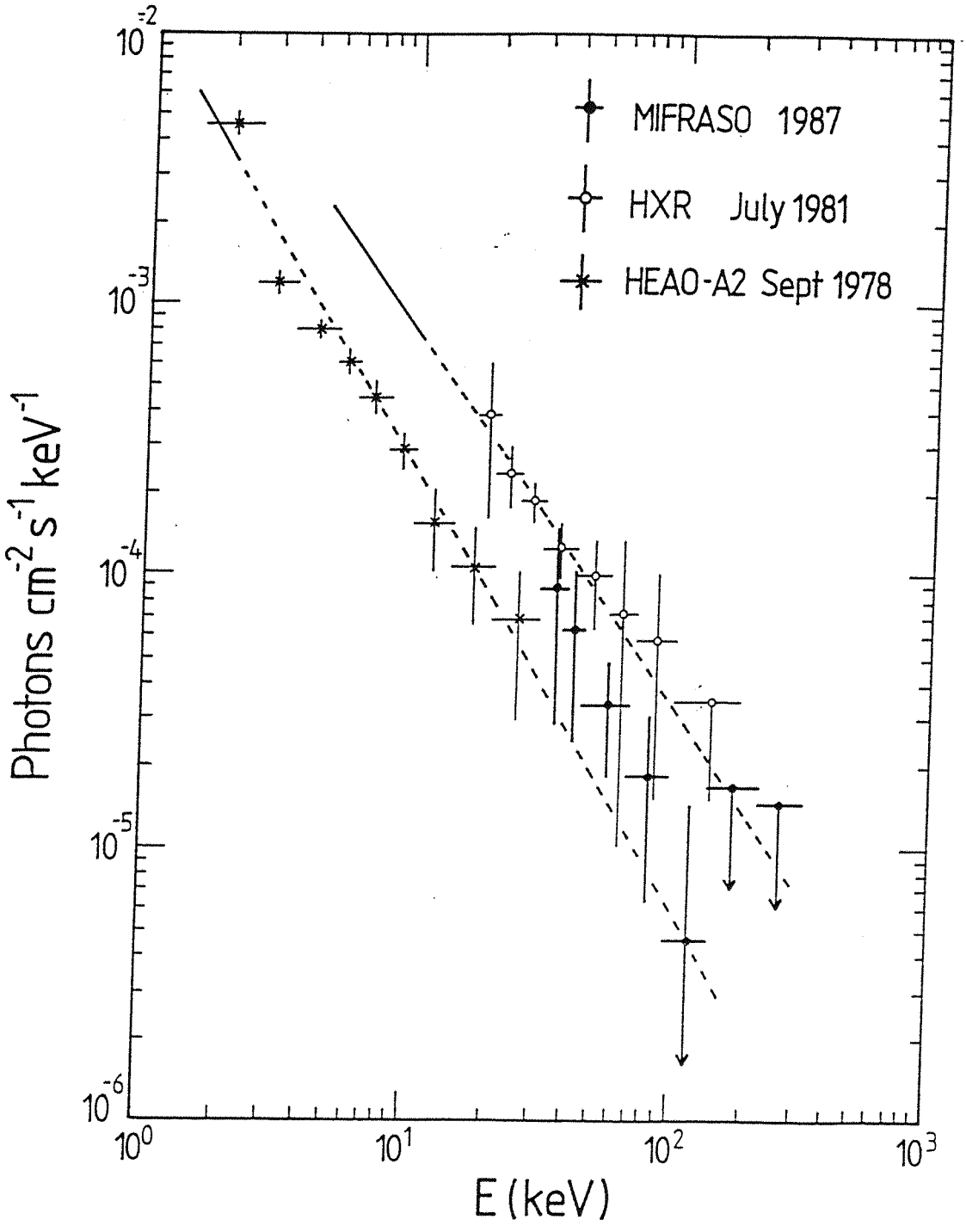

Fig.4.3. The deconvolved energy spectrum from MCG 8-11-11. Also shown are two other representative measurements of the source. From Perotti et al., 1990.

with a reduced chi-squared of 0.36 with 9 degrees of freedom. Errors given are at the 1σ confidence level for the joint variation of two parameters.

Fig 4.4 shows an $\nu F\nu$ plot of available data covering the electromagnetic spectrum from radio to gamma-rays for emission from MCG 8-11-11.

It is immediately clear from Fig.4.3 that the X-ray emission from this Seyfert galaxy has undergone considerable change over a period of years. From a study of other observations of the source it is clear that the maximum power output from this object, at least for high energy photons, occurs in the low energy gamma-ray region of the spectrum around 1 MeV. The excess power output in the X/gamma-ray region of the spectrum is visibly demonstrated in Fig.4.4 which shows the emission from MCG 8-11-11 from radio wavelengths to the SAS-2 upper limit around 100 MeV. For convenience the errors on the X-ray measurements are not included. The values corresponding to the radio as well as the infra-red to ultra-violet emissions have been taken from Spinoglio et al., (1985) and references therein. The power spectrum is dominated by the hard X/low gamma-ray emission peak, with a rise towards the far infra-red as measured by the IRAS satellite. Whereas the radio emission is suppressed, presumably by synchrotron self-absorption, it is interesting to note that there appears to be a minimum in the power output in the UV to X/UV. Future X/UV missions such as the wide field camera on the *ROSAT* spacecraft should be able to demonstrate the existence or otherwise of reduced power output at these frequencies. At other wavebands, however, MCG 8-11-11 is classed as one of the more luminous Seyferts having, for example, a 2-10 keV luminosity of typically twenty times that of the mean value for NCG 4151 as measured by EXOSAT over the period 1983-4 (Pounds et al., 1986).

Despite the immense X/gamma-ray luminosity of this object, and due to the relative infrequency of the observations, it is impossible to draw any firm conclusions as to the compact nature of the source from the high energy measurements alone. Although the source emission

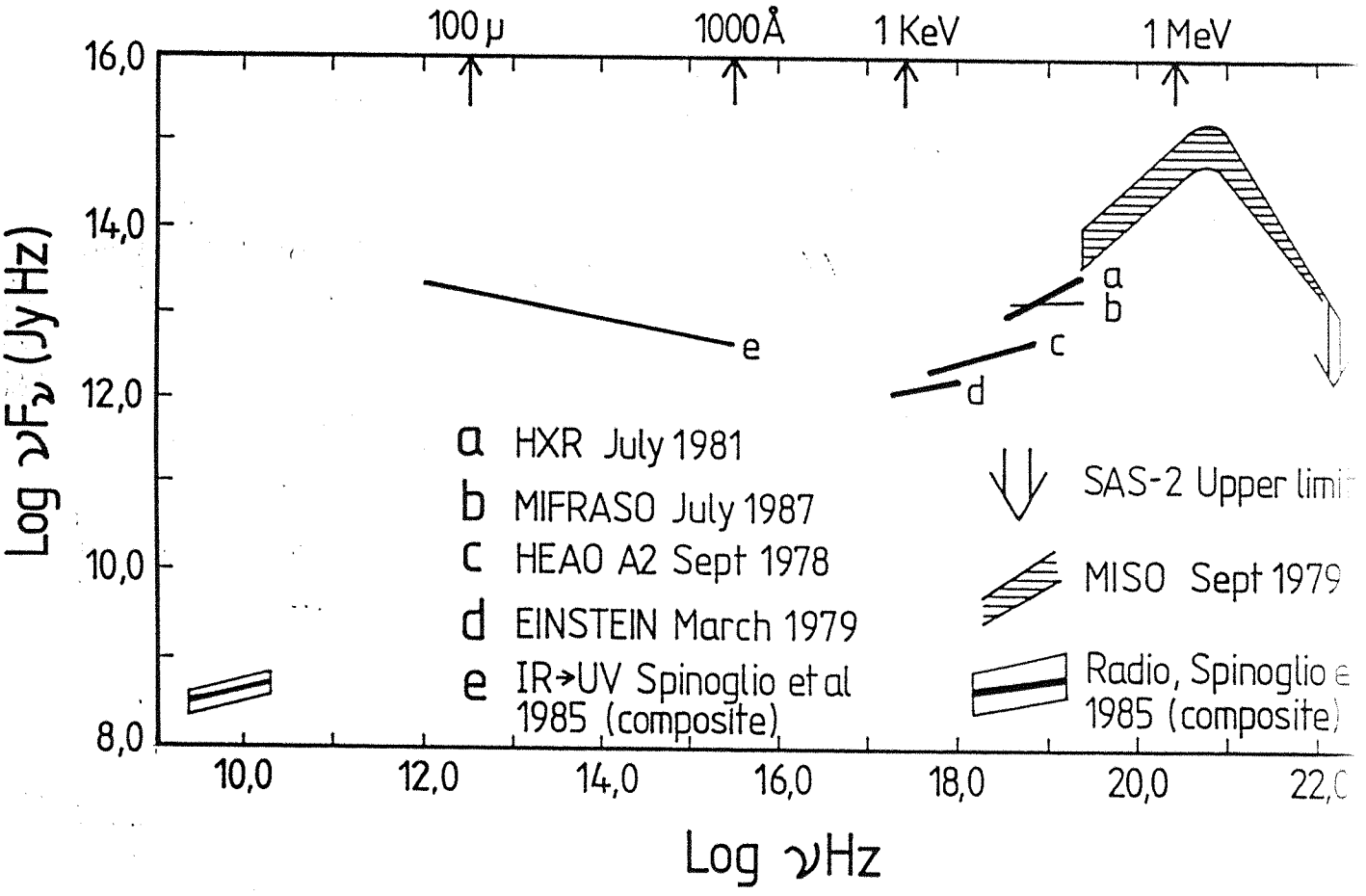

Fig.4.4. An $\nu F\nu$ plot of data taken from measurements of MCG 8-11-11. From Perotti et al. 1990.

undergoes dramatic changes, the long periods between measurements render an estimate of the compactness parameter meaningless. The flux changes of about 2 over one month measured by Ariel V (Ward et al.,1977) and about 2.75 as measured by HEAO over a period of 180 days (Mushotzky et al., 1980) are insufficient to identify the origin of the emission with a compact nuclear zone. A search for short term variability in the X-ray emission spectrum based on the 9 hours of HEAO-A2 data failed to detect any large-amplitude short-term variations from MCG 8-11-11.

4.5 3C273

The quasar 3C273 was observed for a total of 3842 seconds on source useful data between 15.10 UT and 18.25 UT during the 1987 flight of the *MIFRASO* telescope. Corresponding background measurements were made for a total period of 4161 seconds. These background measurements were made using the same sequence of steering manoeuvers as those used to track the source performed on a region of sky 3.5 degrees away from 3C273 having the same declination but different right ascension. This method has the advantage of minimising systematic errors due to elevation and azimuthal changes. During the course of the observation, the atmospheric depth varied between 4.1 and 4.3 g/cm^{-2} with a mean value of 4.2 g/cm^{-2} during the source tracking period. The variation of the background noise with atmospheric depth was not more than 1% during the course of a single observational segment. A series of calibration checks using the on-board Am^{241} sources found the energy response of the telescope to be stable to within $\pm 1\%$ during the course of the observation.

The observational sequence was arranged so that approximately equal time periods were devoted to the on source and the background measurements. The total period was split into 7 segments of on source and 7 segments of background intervals. Correlations between the background counting rate and potential sources of systematic variation such as position or

altitude were investigated. During the background periods the count rate correlation with residual depth was carefully estimated in order that an appropriate correction to the background noise subtraction could be made for each on source period, thus reducing this, the major source of systematic error, to below the level of statistical fluctuations. The orientation axis of the telescope with respect to the direction of 3C273 was estimated and found to be less than 0.1 degree. The precision of the orientation platform pointing was verified during the course of the balloon flight by means of drift scan observations of the Crab and Cygnus X-1.

An excess count-rate spectrum was obtained from the observation of 3C273 and is shown in Fig.4.5. The statistical significance of the observation was found to be 5σ in the 30-54 keV band, 3.3σ in the 54-110 keV band and 3.1σ in the 110-315 keV band.

The photon spectrum was produced under the assumption of a power law emission from the source. Deconvolution of the atmospheric interaction (mean value 5.31 g/cm^2 along the line of sight to 3C273) together with the detector response function has been checked and its precision confirmed by observation of the Crab region. The resulting spectral points are presented in Fig.4.6, together with other hard X-ray measurements of 3C273. The best fit power law spectrum was found to be

$$\frac{dI}{dE_x} = 3.9^{+1.0}_{-1.4} \times 10^{-2} E_x^{-1.61^{+0.75}_{-0.60}} \text{ photons cm}^{-2}\text{ s}^{-1}\text{ keV}^{-1}$$

with a reduced chi-squared value of 0.36 with 9 degrees of freedom. Errors given are 1σ confidence for the joint variation of two parameters.

4.6 The Coma Cluster of Galaxies

The Coma cluster was observed by the *MIFRASO* telescope between 18.50 and 20.43 UT during the 1987 flight. The observational time was divided into three on source segments

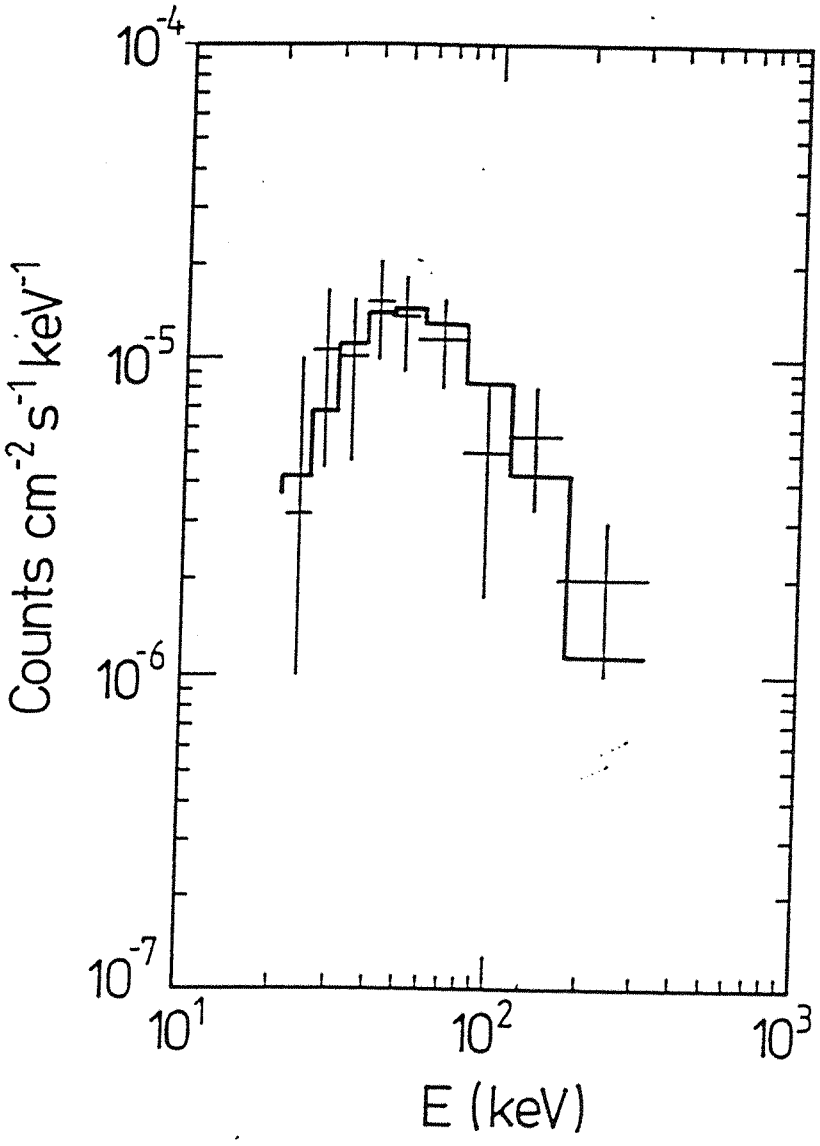

Fig.4.5. The excess countrate spectrum obntained from the observation of 3C273 (Dean, private communication).

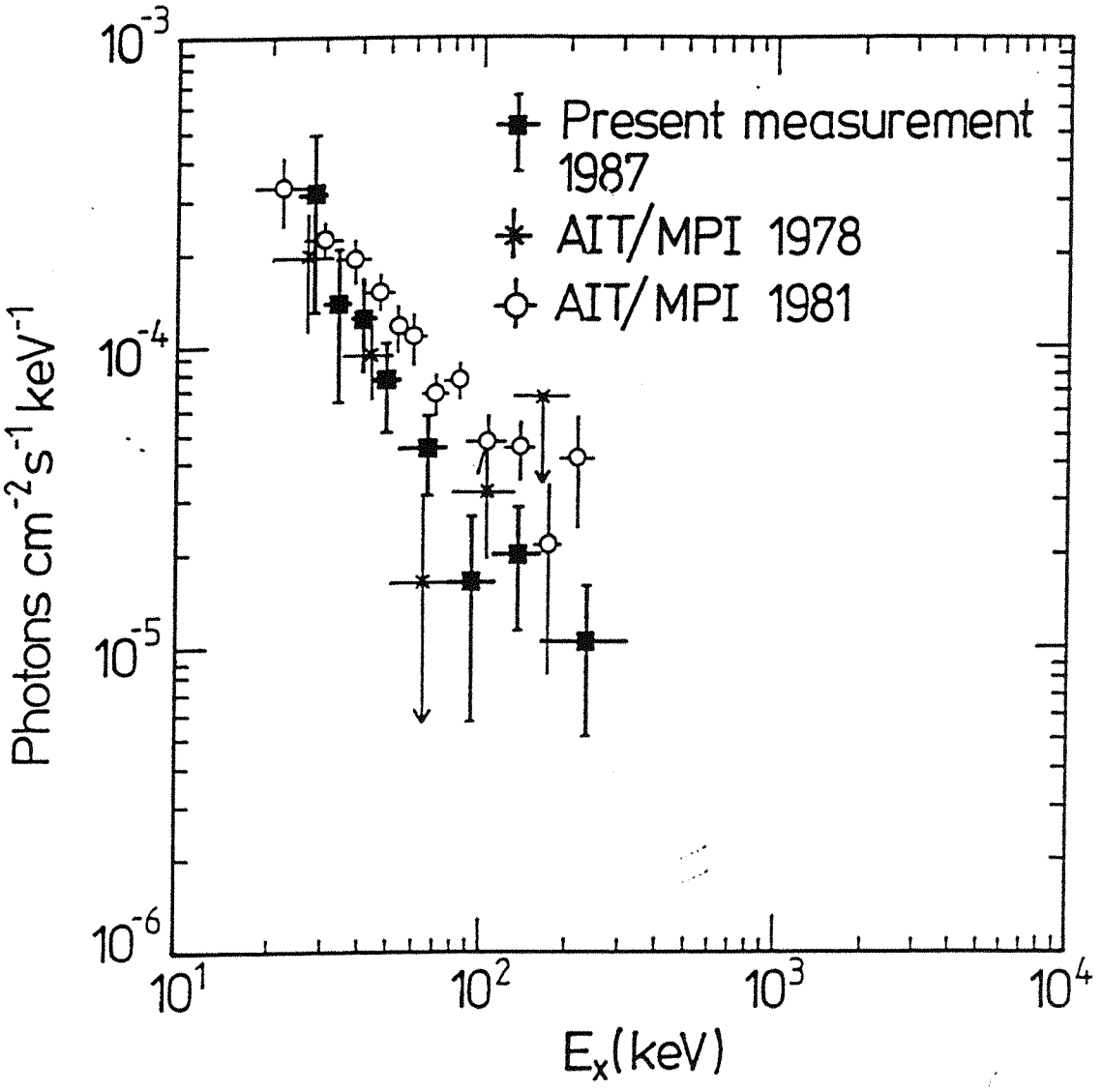

Fig.4.6. The deconvolved energy spectrum of 3C273 together with two other measurements of the source (Dean, private communication).

separated by background measurements. The total time for on source observation was 2725 s. and 3319 s. off source, at a mean float altitude of 4.25 mbar. The exposed area of scintillation detectors was 2268 cm^2. Analysis of data from the proportional counters is still in progress. Variations in the background counting rate arising from systematic variations in altitude, latitude, longitude and position were investigated and the necessary corrections applied to the three sets of observations.

An excess countrate spectrum interpreted as originating from the direction of the Coma cluster was detected in the energy band 30-130 keV with a statistical significance of4.4σ. Assuming a single power law emission for the photon spectrum and folding through the response function of the detector and the atmospheric transmission function the best fit power law was found to be :

$$\frac{dI}{dE_x} = (8.6 \pm 2.8) \times 10^{-5} E_x/50 \text{ keV}^{-1.82\pm1.1}$$

which has a reduced chi-squared value of 0.36 with 5 degrees of freedom.

A thermal fit with kT=68.6 is also acceptable with a reduced chi-squared of 0.26 with 5 degrees of freedom. The errors were computed with a joint variation of two parameters corresponding to a confidence level of 1 σ. Fig.4.7 shows the power spectrum obtained from the *MIFRASO* observation, together with previous hard X-ray measurements of the source.

The presence of hard X-ray emission from the Coma cluster was first suggested by the OSO-8 satellite observations, and then confirmed from observations made with the HXR balloon experiment. A recent re- analysis of data taken from the HEAO A-4 satellite have set upper limits to the emission above 30 keV that are inconsistent with the OSO-8 and HEAO A-4 results. The lack of spatial resolution of the cluster does not permit unequivocable interpretation of these high energy observations. AGN intensity variations may account for the hard X-ray tail seen from the OSO-8, HXR and *MIFRASO* observations, inconsistent with upper limits from the

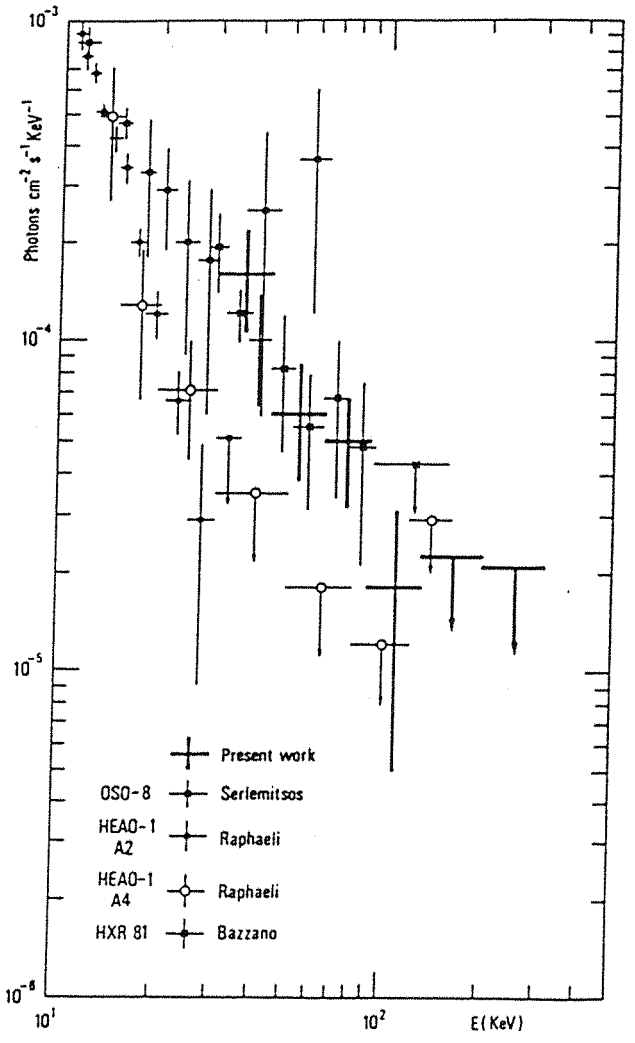

Fig.4.7. The deconvolved energy spectrum of the Coma cluster observation, together with four other measurements of the source (Dean, private communication).

HEAO-4 observation of the Coma cluster. However, the absence of any compact field object or active galaxy associated with the cluster would seem to rule out this hypothesis (Henriksen et al., 1985).

Conclusions from the *MIFRASO* observations are that a hard X-ray tail is emitted within 2 degrees of the centre of the Coma cluster, possibly with variable emission. Furthermore, if the high energy photons are produced by an inverse-Compton process (as suggested by the presence of a radio halo) then these photons may significantly contribute to emission from the cluster down to 20-30 keV. Open questions that still remain include the question of is the hard X-ray tail really variable, and is the variability timescale consistent with the inverse-Compton scenario that has been proposed (Bazzano et al., 1984). Furthermore, is the flux detected above 30 keV emitted from an extended process (as it would be in an inverse-Compton production site), or rather is it due to a single point source ? If the latter is the case, then is the compact source physically associated with the cluster and what kind of emission mechanisms are responsible for hard X-ray production ?

4.7 Cygnus X-1

Cygnus X-1 is the archetypal member of the class of binary X-ray sources that may contain a black hole as the compact object. It displays an orbital period of 5.6 days and the mass of the secondary has been calculated from optical measurements to be in the range 8-16 solar masses. The emission from Cygnus X-1 varies on a wide variety of time scales from milliseconds to several seconds, and also displays long term variability over periods of months.

The differential spectrum of the object from 20 to 200 keV may be described by a power law of spectral index -1.8 to -2.0, with a steepening at higher energies. There is considerable long term variability with three distinct states of emission, known as 'high', 'low' and 'super-low' being evident. The average energy spectrum of the low state is quite stable. Below 20 keV

the spectrum is much stronger and steeper than in the low state while above 20 keV it also steepens but becomes weaker as if the entire spectrum is pivoted above a fixed point (Nolan 1982). The super-low state reported on the basis of HEAO-3 data appears to have a similar spectral shape to the low state and is characterised by low X-ray flux in both the soft and the hard regions (Ling et al., 1983).

The most widely accepted theories of Cyg X-1 all use an accretion disc. The observed rapid variability of the system may arise from random variations in the accretion flow or turbulence in the disc (Nolan 1982). The 'high' and 'low' spectral states are probably caused by the accretion disc having two semi-stable states. Which state the disc assumes is determined solely by the accretion rate. It is not clear that the 'super-low' state is anything other than a low luminosity 'low' state and may not represent a change of structure in the accretion disc. The spectral shape of Cyg X-1 can be explained by a Comptonized spectrum in which the emitted photon spectrum is only weakly dependent upon the original source distribution (Nolan 1982) and has the form of a power law at low energy, with a steepening occurring around 3kT. This model provides a natural explanation of the 'high' and 'low' states. In the 'high' state an extra component with an effective temperature of approximately 1 keV begins to radiate strongly, possibly due to increased accretion. Some of the extra photons pass through the very hot region, thereby increasing the efficiency of Compton cooling and causing the temperature to drop with associated softening of the observed spectrum.

The *MIFRASO* telescope observed Cygnus X-1 from 1.32 UT to 2.30 UT during the 1987 flight. About 900 seconds of useful on source data were recorded. The photon spectrum was well described either by a single power law with a photon index of $\alpha = 1.90 \pm 0.07$ or by a Comptonised model characterised by an electron temperature of kT=55±10 keV and an optical depth of τ=2.4±0.4. Errors given are at the 1 σ level for the joint variation of two parameters, with a reduced chi-squared of 1.0 for 19 degrees of freedom. The measured flux values suggest

that during the *MIFRASO* observation the source was in a intermediate position between the so-called 'low' and 'super-low' states.

Fig.4.8 shows the fit by a power-law to the deconvolved energy spectrum of Cygnus X-1. Fig.4.9 shows the fit by a Compton model and Fig.4.10 shows corresponding measurements made by the *MISO* telescope in 1979 and 1980.

A timing analysis of the Cygnus X-1 observation was made in order to search for pulsations from the compact object. The results of this search are presented in Chapter 7.

4.8 Hercules X-1 and SS433

The *MIFRASO* telescope observed both these sources during its 1987 flight. The X-ray binary Hercules X-1 was observed from $20^h\ 20^m$ UT to $22^h\ 30^m$ UT with a total on-source exposure time of $1^h\ 4^m$. The unusual binary system SS433 was observed from $22^h\ 32^m$ to $01^h\ 16^m$ with a total on-source exposure time of $1^h\ 18^m$. Both sources are known to be highly variable in their X-ray emission, the flux observed dependent upon their orbital phase. No excess hard X-ray flux was seen from either of these sources by the *MIFRASO* telescope. A possible explanation is that both of these sources were at an orbital phase corresponding to a low state of X-ray emission at the time of the *MIFRASO* observations, and no further analysis was attempted.

Although this chapter has concentrated on the spectral results of a number of astronomical objects, this thesis is primarily concerned with timing analysis of periodic sources such as the Crab Pulsar. The next chapter outlines the conventional approach to fast timing analysis and shows how the disadvantages in using these conventional methods paves the way for new techniques.

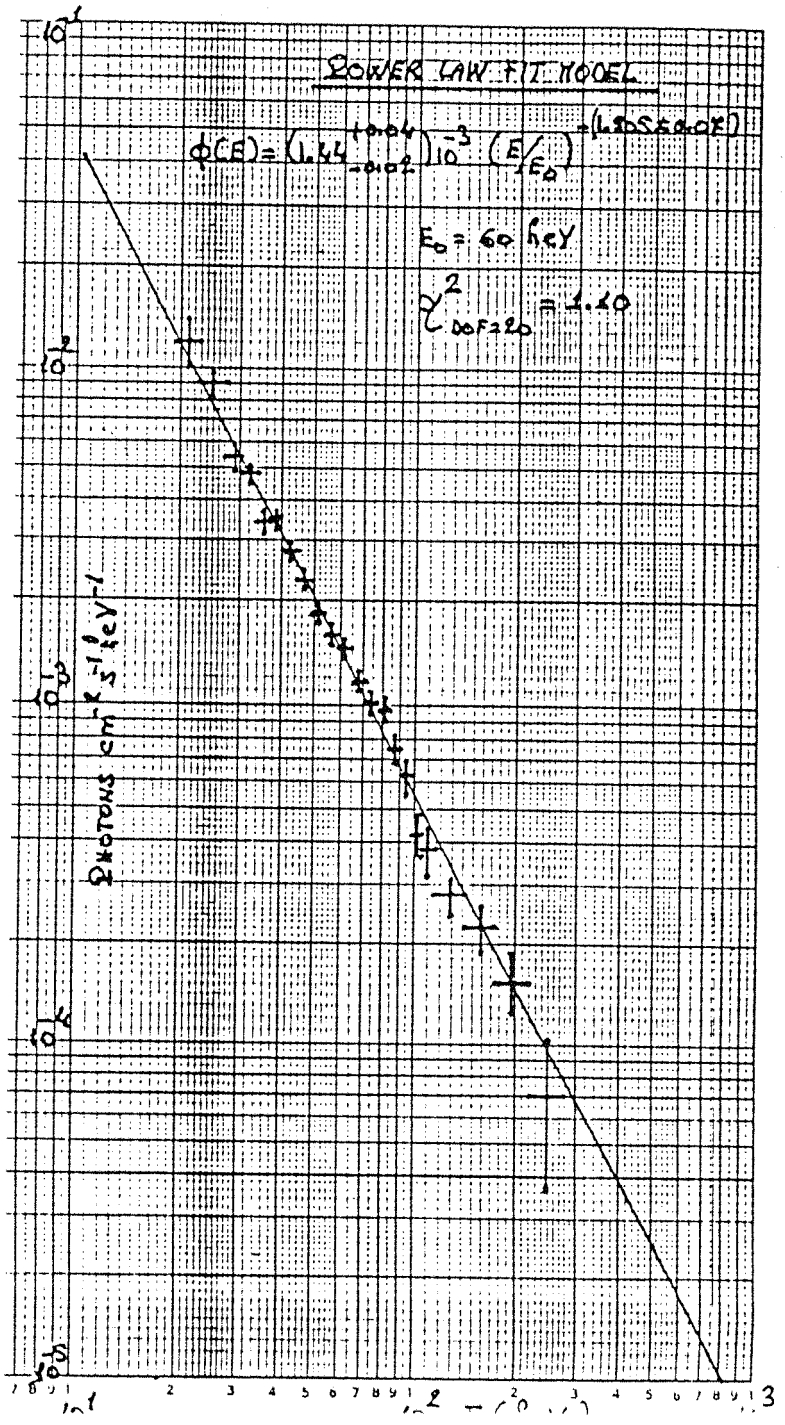

Fig.4.8. A power-law fit to the deconvolved energy spectrum of Cygnus X-1 (Perotti, private communication).

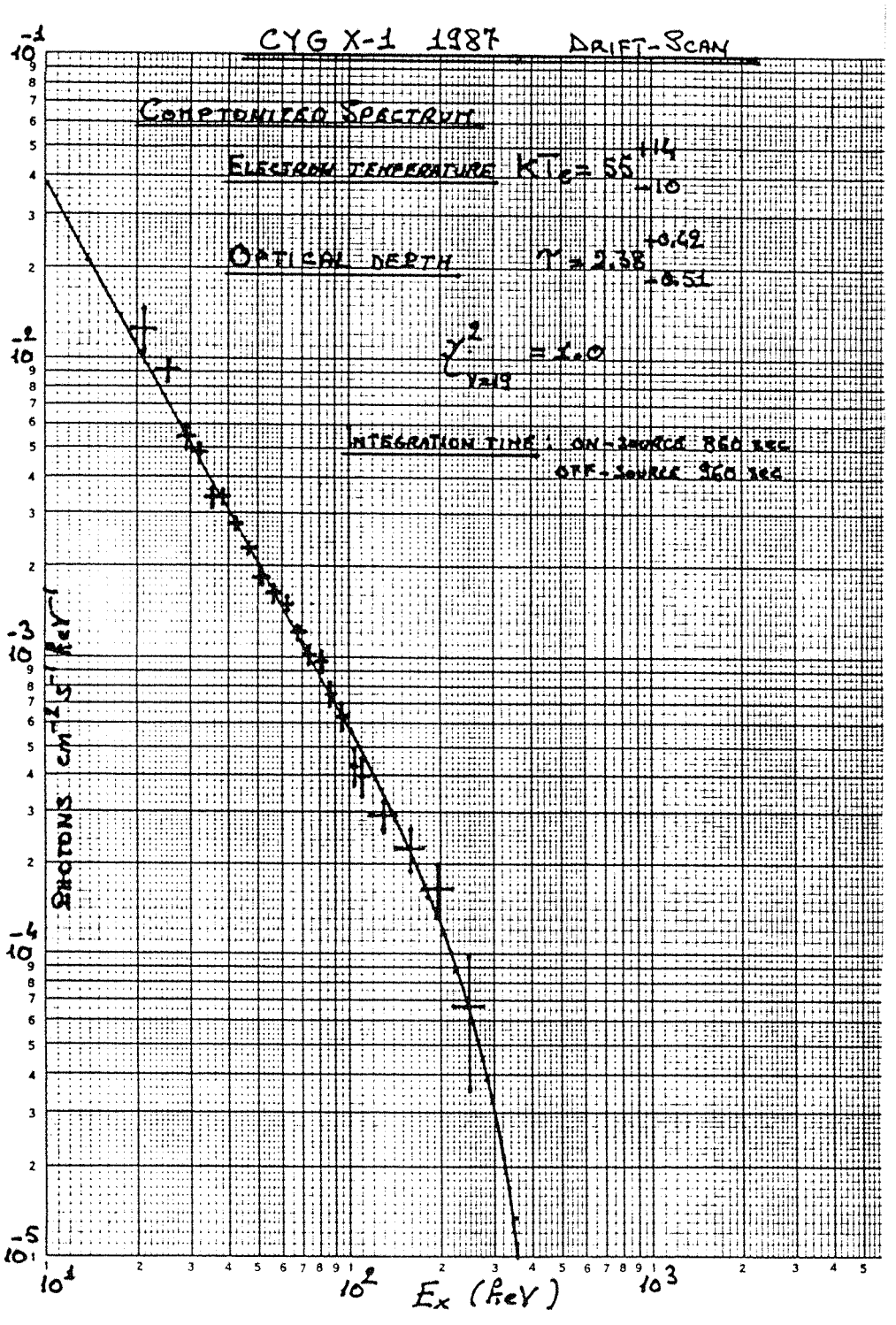

Fig.4.9. A Compton model fit to the deconvolved energy spectrum of Cygnus X -1 (Perotti, private communication).

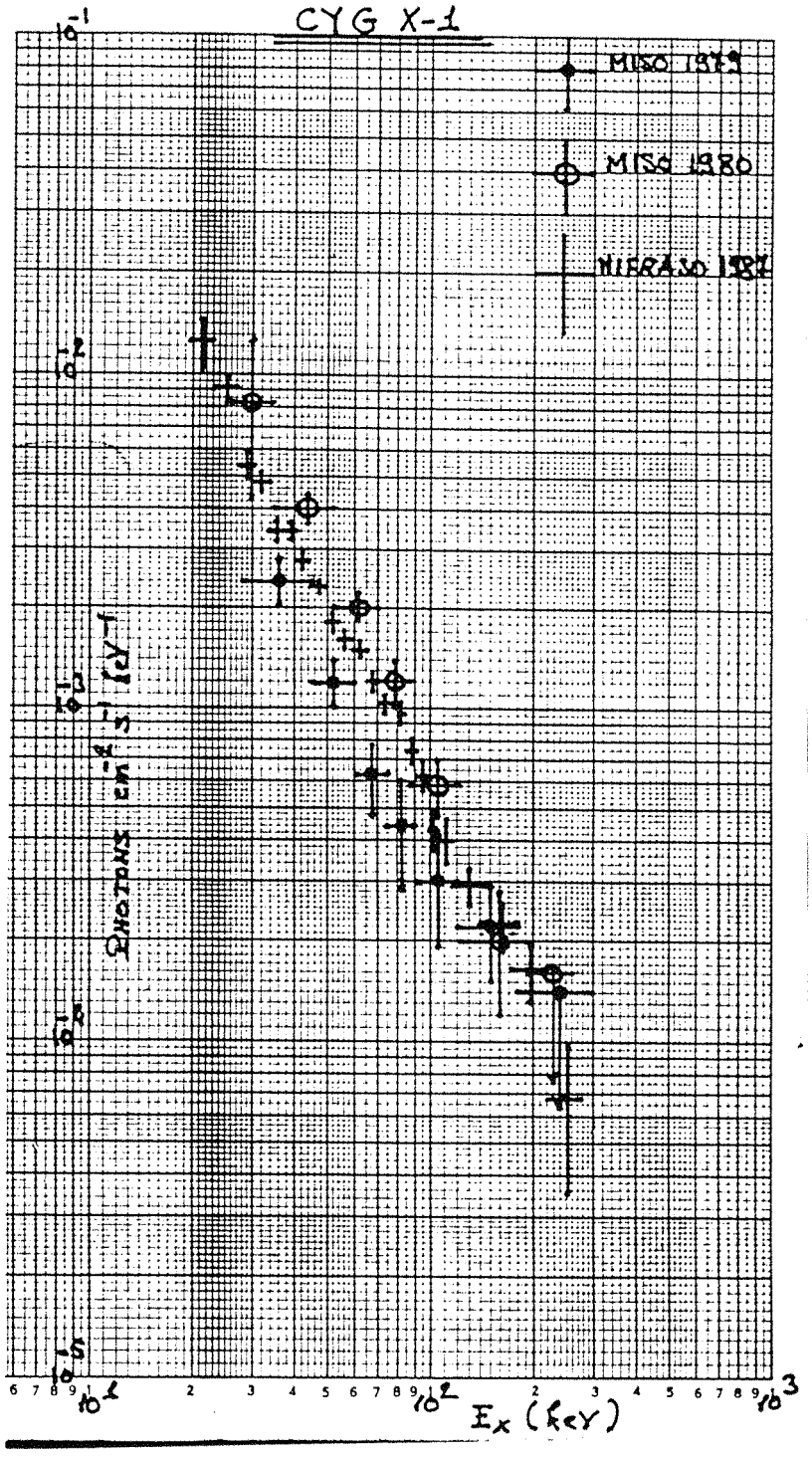

Fig.4.10. Measurements of Cygnus X-1 made by the *MISO* telescope in 1979 and 1980 compared to those made by *MIFRASO* in 1987 (Perotti, private communication).

CHAPTER 5 : THE ANALYSIS OF FAST TIMING OBSERVATIONS USING CONVENTIONAL TECHNIQUES

5.1 Introduction

There are two questions that arise when a search is made of data from a pulsating source: firstly, the question 'are pulsations present?' must be answered, and a statistical significance attached to any pulsed emission found. Secondly, if a significant pulsed effect is found then the question 'what does the pulse profile look like?' arises. The first question is known as testing the set of observational events against the hypothesis of uniformity (no pulsations present), whilst the second question is known as parameter estimation of the light-curve. This chapter introduces the traditional statistical tests used to test against uniformity and also the traditional method of light-curve estimation.

Tests for pulsed emission in X and γ-ray astronomy fall into two groups: parametric tests, where the shape of the periodic signal is assumed, for example, to be a pure sinusoid and event arrival times may be binned then Fast Fouriet Transform techniques applied, and non-parametric tests, where nothing about the shape of the signal is assumed. A periodicity search using the latter class of test is conducted by first folding the event arrival times with an appropriate trial period and possible period derivative to form a set of phases. The resultant phase density distribution, an estimation of which forms the 'light-curve' or 'pulse profile', is then tested against the null hypothesis of phase uniformity, $\mathcal{H}_o$. If $\mathcal{H}_o$ is rejected with a confidence greater than some chosen significance level, the alternative hypothesis, $\mathcal{H}_1$, is accepted: that is, that there is a periodic signal present within the data. Care must then be exercised in distinguishing a true source from an artefact of the experiment, for example, dead-time or sampling clock effects. There is a wide variety of statistical procedures with which to test $\mathcal{H}_o$ against $\mathcal{H}_1$. The problem with most such tests is that they are powerful in detecting only certain kinds of phase density distributions, whilst other distributions may pass unnoticed. The subjective choice and use of a

test statistic preferentially biased towards a particular form of phase distribution known *a priori* seems unsatisfactory, but is relevant and useful when studying sources of known periodicity.

5.2 Conventional Statistical Approaches

The two statistical tests most commonly used are the Pearson test and the Rayleigh test for uniformity.

5.2.1 The Pearson Test

The Pearson test (Pearson 1905) defines an origin for the phase domain and then divides the domain into a number of equal bins. The number of bins chosen acts as a smoothing parameter and all information within a bin is lost. If the number of bins chosen is b, the sample size is n and the number of events in bin i is $x_i(o)$ for a given phase origin o where $0 \leq o < \frac{1}{b}$ and $1 \leq i \leq b$, then the resulting test statistic is defined as

$$\chi^2_{(b-1,o)} = \sum_{i=1}^{m} \frac{(x_i(o) - n/b)^2}{n/b} \tag{1}$$

which is distributed as χ^2_{b-1} for a given o under the null hypothesis. The test is an example of a (smoothed) non-parametric test for uniformity because no assumption is made concerning the underlying form of the phase density distribution. The Pearson test is easy to invoke (hence its popularity) but has a number of disadvantages. A narrow peak may be split between two bins, reducing the power of the test, and the choice of the number of bins to use is arbitrary. The statistic is not invariant under a global phase-change of origin o, and narrow features may be 'massaged' into one bin, subjectively increasing the power of the test. Finally, the sign of the

deviations in (1) are not taken into account, so the test is powerful in detecting $\frac{b}{2}$ frequency oscillations which, for large b, are unlikely to correspond to a physical source, thus $\mathcal{H}_o$ may be falsely rejected, which is known as a type **I** error. This last difficulty may be solved if the Pearson test is followed by the Runs test (Eadie et al., 1971, Buccheri 1985). The Runs test tests for a dependency of the signs of $(x_i(o) - n/b)$ and will give a small probability if the light-curve is source-like (that is, when the signs are not randomly distributed), thus increasing the power of Pearson's test. The Pearson test is powerful in detecting narrow pulses of duty cycle $\sim \frac{1}{b}$ and is thus popular for the analysis of Crab or Vela-type light curves with 20-40 bins per phase domain.

5.2.2 The Rayleigh Test

The Rayleigh statistic (Rayleigh 1894, Mardia 1972) is one of the most basic tests for uniform distribution on a circle. It is a parametric test for power in the fundamental harmonic of the trial period, although it may be used non-parametrically, for example, in Fast Fourier Transform techniques. For a sample of size n, the test statistic is defined as

$$2n\bar{R}_1^2 = 2n(\hat{\alpha_1^2} + \hat{\beta_1^2}), \tag{2}$$

where

$$\hat{\alpha_1} = \frac{1}{n}\left\{\sum_{i=1}^{n} \sin 2\pi\phi_i\right\} \tag{3}$$

and

$$\hat{\beta_1} = \frac{1}{n}\left\{\sum_{i=1}^{n} \cos 2\pi\phi_i.\right\} \tag{4}$$

The Rayleigh power $n\bar{R}_1^2$ is χ_2^2 distributed if n is large and the resultant probability may be calculated from

$$Pr = Pr(> n\bar{R}_1^2 | \mathcal{H}_o) = e^{-n\bar{R}_1^2}. \tag{5}$$

If the phase density distribution contains one or more narrow peaks the sensitivity of the test is lowered as significant power is contained in higher harmonics away from the fundamental. In such cases other tests such as Pearson's are more powerful. There is one important case where the Rayleigh test fails: if the density distribution is bimodal, as seen in the double-peaked Crab and Vela pulsar light curves, the resultant vector of the trigonometric moments defined in (3) and (4) will cancel out as the phase angle between the two peaks approaches π, and the Rayleigh test may falsely reject $\mathcal{H}_1$. This is known as a type **II** error.

The Rayleigh test was first advocated for the use in VHE γ-ray astronomy by Gibson et al. (1982), who referred to it as 'the uniformly most powerful test for the uniformity of a circular (phase) distribution'. The phrase 'uniformly most powerful' (UMP) has a precise statistical definition and implies that the test under consideration has the largest power of all possible tests for all possible types of phase density distribution (see Leahy et al., 1983, for formal definitions and discussion). As pointed out by those authors, and noted above, there are circumstances under which the Rayleigh test may falsely reject $\mathcal{H}_1$ in the presence of a periodic signal. Furthermore, because one test is UMP it does not follow that another is not. It may be shown through the Neyman-Pearson lemma that both the Pearson and Rayleigh tests are both UMP under certain conditions (Korn and Korn 1968; Hoel 1971).

The Rayleigh test is powerful in detecting broad, unimodal phase density distributions such as those seen in the high energy emission of accreting X-ray binary systems. An example of successful use of the Rayleigh test is the discovery of a 12.6 ms pulsar in the binary system Cygnus X-3 by the Durham Ground Based Cerenkov group (Chadwick et al., 1985). Fig.5.1 shows the results of the Rayleigh test from this experiment.

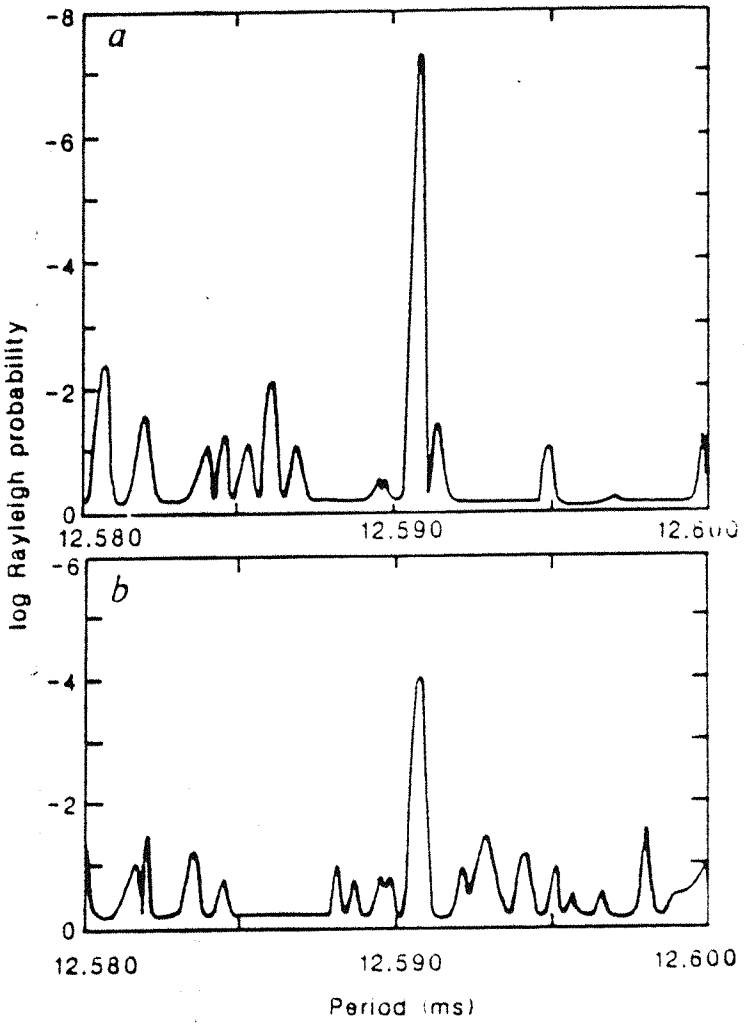

Fig.5.1. An example of use of the Rayleigh test by the Durham VHEGRA group : the discovery of a 12.59ms pulsar in Cygnus X-3.(a) The chance probability verses trial period for September 12, 1983 (b) for October 2, 1983 at the same phase of the orbital period. From Chadwick et al., 1985.

5.2.3 Fourier Analysis

The analysis of time series has often been carried out using Fourier methods. Consider some quantity, $X(t)$, which varies with time, t. Information about periodicities in this quantity could be found from the Fourier transform of $X(t)$:

$$F(\omega) = \int_{-\infty}^{\infty} X(t) \exp(i\omega t) dt \tag{6}$$

or from the 'power' at angular frequency ω, $|F(\omega)|^2$.

In the case of a stochastic process, where one may expect to find correlations in the data on certain timescales,r, the 'power spectrum' may be used to obtain this information:

$$P(\omega) = \int_{-\infty}^{\infty} r_X \exp(i\omega r) dr \tag{7}$$

where r_X is the autocorrelation function,

$$r_X(r) = \int_{-\infty}^{\infty} X(t) X(t+r) dt. \tag{8}$$

The autocorrelation theorem (eg, Bracewell, 1978) can be used to show that $P(\omega) \propto |F(\omega)|^2$, that is, that the power spectrum and the Fourier power are identical.

In practise, data are often taken at discrete time intervals instead of continuously over an infinite time, forming a 'time series', that is, a series of measurements of some quantity $X(t_i)$ made at a series of times $t_i, i = 1, ..., N$. For such data there are many techniques for estimating $F(\omega)$ and $P(\omega)$.

For a continuous observation over a time T, one can obtain the 'finite Fourier transform' defined as

$$F_T(\omega) = \int_{-T/2}^{T/2} X(t) \exp(i\omega t) dt, \tag{9}$$

and in the case of a time series one can obtain the 'discrete Fourier transform' as

$$F_N(\omega) = \sum_{j=1}^{N} X(tj) \exp(i\omega tj). \tag{10}$$

$F_N(\omega)$ are often computed using Fast Fourier Transform algorithms.

5.2.4 The Z_m^2 Test

The Z_m^2 test was introduced by the COS-B collaboration in the analysis of gamma-ray data (Buccheri et al., 1983). The test is an extension of the Rayleigh test and the test statistic is defined as

$$Z_m^2 = \sum_{k=1}^{m} n\bar{R}_k^2 = \frac{2}{n} \sum_{k=1}^{m} \left[\left(\sum_{j=1}^{n} \sin 2\pi k\phi_j \right)^2 + \left(\sum_{j=1}^{n} \cos 2\pi k\phi_j \right)^2 \right] \tag{11}$$

which is χ_{2m}^2 distributed for a fixed value of m under uniformity. This test sums the power in the first m harmonics of the trial period. For $m = 1$ the test reduces to the Rayleigh test, powerful for detecting broad peaks, whilst a choice of $m \succeq 10$ makes the test powerful in detecting narrow peaks. However, the subjective choice of m remains an unsatisfactory feature, for if the form of light-curve is not known a priori then one either oversmooths or undersmooths the data with a specific choice of m. The test shares the disadvantage of the Pearson test in that the test will also be powerful for m oscillations, while one expects only a few source- like peaks to be shown even if m is large.

However, the advantages of Z_m^2 over Pearson's test are important: this test statistic is not dependent upon a bin width, so there is no danger of splitting a peak between two bins.

The next advantage is that the distribution of Z^2_m is known even for very small sample sizes. This has been shown for n>100 by means of simulations (Gerardi et al., 1982).

5.2.5 Choosing the best test for Uniformity

In most cases, the phase distribution of events due to X-rays or gamma-rays is expected to be uniform and so it is only necessary to test the null hypothesis, $\mathcal{H}_o$, and see if the observed phase distribution is significantly different from uniform. Many statistics, including those discussed above, could be used to do this. However, some statistics are more powerful than others and it is sensible to choose a test statistic which is powerful against alternatives to the null hypothesis of the form one might expect from previous observations of the source under examination .

Consider a particular statistic, S. At a chosen level of significance,α, for example, 5%, then if $\mathcal{H}_o$ is true (that is, uniform distribution), then S will exceed its critical value S_α in a fraction α of all trials, that is,

$$Pr(S > S_\alpha|\mathcal{H}_o) = \alpha \tag{12}$$

When used at the same level of significance then all statistics are equally safe (that is, all statistics will incorrectly reject $\mathcal{H}_o$ a fraction α of the time).

In cases where $\mathcal{H}_o$ is not true (that is, there is a periodic source present in the data), one would like S to exceed S_α as often as possible. If a particular alternative hypothesis $\mathcal{H}_1$ were true, one would like the probability of incorrectly accepting $\mathcal{H}_o$,

$$\beta = Pr(S < S_\alpha|\mathcal{H}_1) \tag{13}$$

to be as small as possible. The 'power' of the test is defined as (1- β) and is the probability of correctly rejecting $\mathcal{H}_o$. The power of a statistical test at a particular level of significance is a function of the true distribution and some statistics are more powerful than others against particular alternatives to $\mathcal{H}_o$, that is, differing phase density distributions.

Fig.5.2 shows the power of various statistical tests verses the duty cycle of the underlying phase density distribution of the simulation.U^2 refers to Watson's statistic (Mardia 1972) whilst Υ_n refers to Protheroe's statistic (Protheroe 1985). These are more advanced statistical tests, a discussion of which is beyond the scope of this thesis.H_m refers to a new statistical test which has been recently introduced (de Jager et al., 1989) and which will be fully discussed in the next chapter.

5.3 Estimating the shape of the emission

Once a periodic source has been identified using the statistical tests outlined above, the event arrival times are folded modulo a period (possibly with a period derivative) to produce a series of phases, just as for the period identification. The next problem is to estimate the shape of the emission, that is, estimate the phase density distribution. Such an estimate then forms the 'light-curve' or 'pulse profile' of the source.

Traditionally the phases were binned in a histogram to produce the light-curve. However, there are a number of problems associated with this. For a start, no physical source is likely to resemble a 20 or 40-bins per phase histogram which makes identification of the various components difficult. More importantly one runs into the kind of problems outlined in Section **5.2.1** above.

The error of an estimator at phase θ is defined by the Mean Squared Error (MSE) :

$$MSE = E|\hat{f}_h(\theta) - f(\theta)|^2 \tag{14}$$

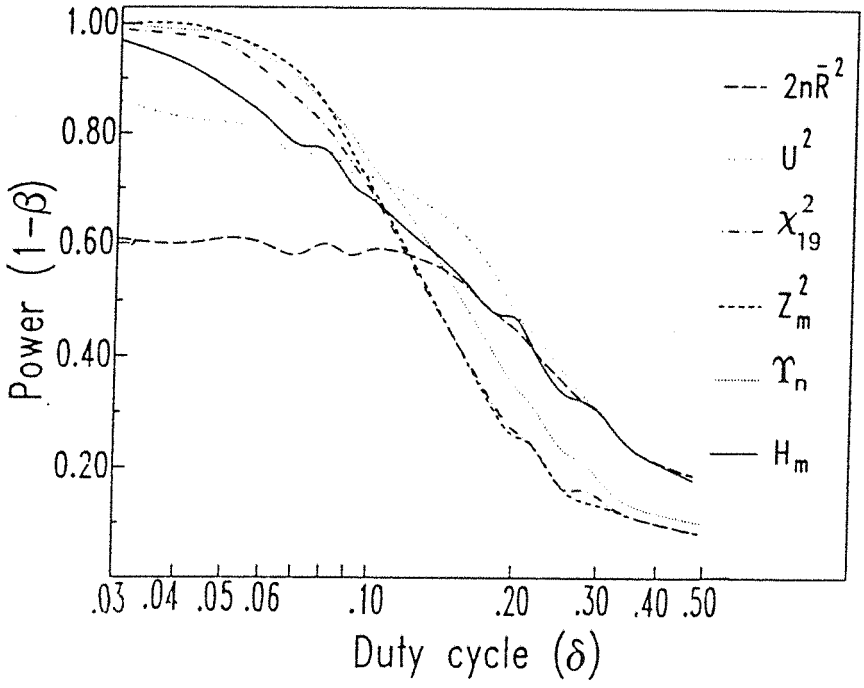

Fig.5.2. The power curve $(1-\beta)$ as a function of the duty cycle for different tests for uniformity. The source density distribution is a Gaussian peak, mixed with a uniform density. From de Jager, 1987.

where $\hat{f}_h(\theta)$ is the histogram estimate of the light-curve, and $f(\theta)$ is the true (unknown) source density distribution. Multiplying out,

$$MSE = E\hat{f}_h^2(\theta) - (E\hat{f}_h(\theta))^2 + (E\hat{f}_h(\theta) - f(\theta))^2 \tag{15}$$

That is,

$$MSE = \text{variance term} + (\text{bias term})^2$$

The variance term is well-known and used to construct confidence intervals on the histogram estimator, as it is easy to estimate from the data. However, the bias is a function of the true (unknown) light-curve and is thus difficult to estimate, and is usually ignored. Note that if the bias is comparable in magnitude to, or greater than the variance, then it would be unwise to construct a confidence band for the whole light-curve based solely on the variance. This is especially true for the histogram estimator due to its step-like nature, which results in a quite large bias.

The quality of an estimator can be evaluated in a global manner by evaluating its mean integrated squared error (MISE)

$$MISE = E\int_0^{2\pi} |\hat{f}(\theta) - f(\theta)|^2 d\theta \tag{16}$$

and it is hoped that

$$\lim_{n\to\infty} \hat{f}(\theta) = f(\theta) \tag{17}$$

with a probability of one.

The histogram estimator is the classical density estimator. After selecting the smoothing parameter (or bin width) h, one is led to construct the histogram

$$\hat{f}_h(\theta) = \frac{1}{nh} \sum_{i=1}^{n} I(h(j-1) \leq \theta_i < hj), \theta(h(j-1), hj), j = 1, ..., M \tag{18}$$

where $M = \frac{2\pi}{h}$ is the number of bins per phase and n the sample size. If one chooses too many bins, the variance component will be large with a small value of the bias. Conversely, if the number of bins is too small, then the bias will be large. Thus there exists a certain number of bins, depending on the shape of the light-curve and the sample size, for which the MISE will be a minimum. Since the MISE evaluates the estimator globally, one can find the number of bins which minimises the MISE, providing one knows the first derivative of the source wave function (Scott, 1979). For an unknown source phase density distribution this is clearly impossible.

The next section describes a conventional timing analysis of the *MIFRASO* observation of the binary X-ray source A0535+26 using the Pearson test to search for pulsations and a histigram to display the pulse profile.

5.4 A conventional timing analysis of the *MIFRASO* observation of A0535+26

From the time-averaged spectrum of A0535+26 (see Fig.4.1) an energy window of 32-52 keV was chosen to search for any pulse signature (Coe et al., 1990). The individual photon event times were extracted for all the periods when the object was on-source and these averaged to one-second time bins. This was done for the eight high-energy detector modules and the files added. This file containing the total event times was folded modulo a series of test periods in the range 100-110 s. and at each period step a χ^2 test was carried out on the folded light curve. No barycentring was necessary due to the relatively long test periods. The resulting period search is shown in Fig.5.3. The search shows a peak in the distribution at approximately 103.5 s. A

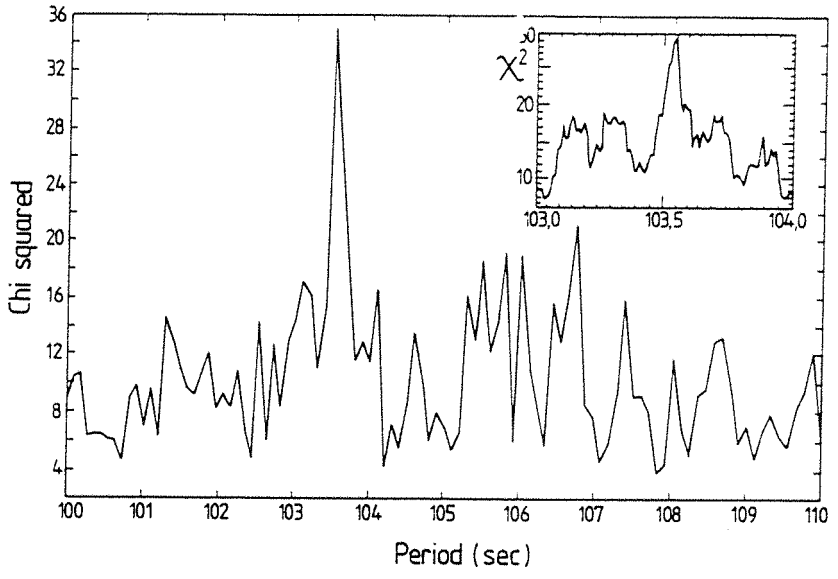

Fig.5.3. The period search of the A0535+26 data. The Pearson test with 10 bins was used. The insert shows the same test applied over a narrower range of trial periods. From Coe et al.. 1990.

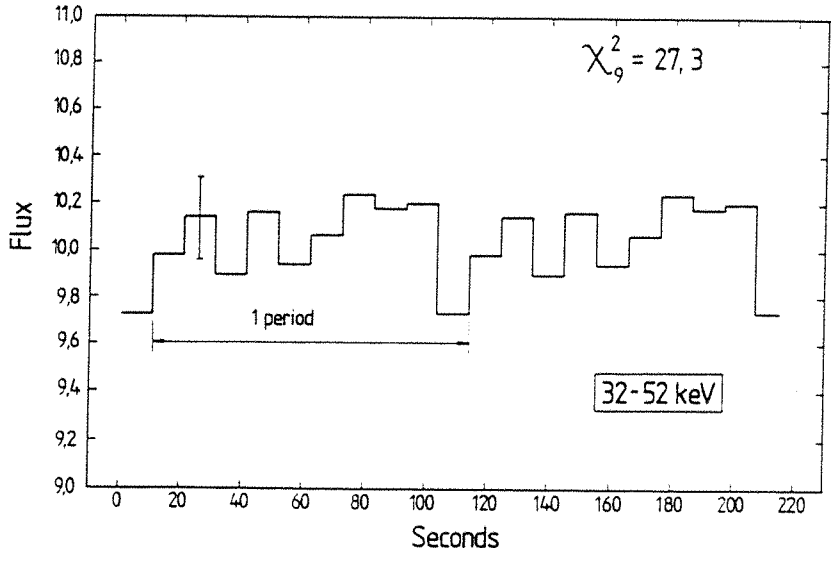

Fig.5.4. The light curve of A0535+26 detected in the energy range 32-52 keV from the *MIFRASO* observation of 1986. From Coe et al., 1990.

closer search over the period range 103-104 s. reveals that the peak was actually at 103.54 ± 0.04 s. The event times were folded at this period and binned in a histogram with 10 bins per phase to produce the lightcurve. This is shown in Fig.5.4. The resulting χ^2 for this profile is 27.3 for nine degrees of freedom, giving a probability of 10^{-3} that the data are consistent with the mean value. This level of significance is consistent with the time-averaged signal, considering that the modulation of the flux from A0535+26 is generally very broad and the pulse profile is expected to show no sharp peaks (Ricker et al., 1976, Bradt et al., 1976).

Note that the number of trial periods in this analysis were not taken into account (see section 7.5) which would further decrease the claimed significance of the result. The pulse profile is a shallow sinusoid which is expected to be weakly detected by the χ^2 test. It would have been instructive to repeat the periodicity search using the Rayleigh test, as this is more sensitive to the shape of the pulsed emission. Of course, this fact was not known before the χ^2 test was performed.

The next chapter discusses a new form of light-curve estimation together with its associated test statistic that has recently been introduced.

CHAPTER 6 : THE ANALYSIS OF FAST TIMING OBSERVATIONS USING THE $H_{\hat{m}}$ TEST AND THE KERNEL DENSITY ESTIMATOR TECHNIQUE

6.1 Introduction

This chapter introduces the concept of the new statistical approach known as 'kernel density analysis'. This comprises two analytical tools : a new statistic for phase uniformity that can be used in searching a dataset for pulsed emission and a new method for estimating the pulse profile, should pulsations be found in the data (de Jager, 1987). The routines were originally developed for the analysis of TeV gamma-ray data, to the author's knowledge this thesis represents the first time that the new techniques have been applied to hard X-ray data.

6.2 The $H_{\hat{m}}$ Test Statistic for Uniformity

From the discussions of the previous chapter it is clear that most tests are biased towards certain forms of light curves. The Rayleigh test is powerful for broad, sinusoidal light curves as seen in the high-energy emission of X-ray binaries. The Pearson test is powerful for narrow, bimodal light curves as seen from the Crab or Vela pulsars. The Z^2_m test combines the good features of both these tests because of the variable number of harmonics that are summed, $m = 1$ reduces to the Rayleigh test whilst $m = 10$ produces a powerful alternative to the Pearson test. What is needed is an extension to this test to vary the number of harmonics to be summed over. The choice of m should be an objective but optimal one. Such a method has been proposed in connection with the optimum choice of harmonics in a Fourier series estimation (Hart 1985). The method estimates the optimum value of m needed to minimise the MISE if the source phase density $f(\theta)$ is unknown. The estimator of the ideal value of m is that value, say $\hat{m}$, which minimises the expression

$$(n+1)\sum_{l=1}^{m}\overline{R}_l^2 - 2m \tag{1}$$

This is called the 'Hart rule' and may be re-written in terms of the Z_m^2 statistic as

$$\hat{m} = \underset{m}{MAXIMUM}\,(Z_m^2 - 4m) \tag{2}$$

Defining the Hart function as

$$F_m = Z_m^2 - 4m \tag{3}$$

we have

$$\hat{m} = \underset{m}{MAXIMUM}\,F_m \tag{4}$$

The use of the above is an example of a maximum likelihood estimation of the parameter m (Friedman 1986). The Hart function is easy to compute from the data itself and provides an optimal choice for m with a firm statistical justification.

With $m = \hat{m}$ the Z_m^2 statistic changes because $\hat{m}$ is now a random variable and thus the test is no longer $\chi^2_{2\hat{m}}$ distributed under uniformity. A new test statistic is required, and the one proposed (de Jager et al., 1989) is

$$H_{\hat{m}} = F_{\hat{m}} + 4 \tag{5}$$

The behaviour of $H_{\hat{m}}$ was investigated through 10^7 simulations for $1 \leq m \leq 20$ and the resultant

probability distribution parameterised, see Table 6.1. It is clear that H_1 is χ^2_2 distributed and is therefore just as powerful as the Rayleigh test if there is only power in the fundamental. From Fig.5.1 it is clear that for duty cycles greater than 20% $H_{\hat{m}}$ is one of the best tests. At smaller duty cycles it is comparable with the Z^2_{10} test (where the assumption of harmonic content had to be made) and the Pearson test with 20 bins (where phase information within a bin is lost).

The simulated distributions were fitted on twenty incomplete gamma functions. The conditional probability of finding a value greater than $k = H_{\hat{m}}$ given knowledge of $\hat{m}$ can be calculated from

$$P(H_{\hat{m}} > k | m = \hat{m}) = \frac{1}{\Gamma(r)} \int_x^\infty e^{-t} t^{r-1} dt \tag{6}$$

with

$$x = \frac{k\overline{H_{\hat{m}}}}{\sigma^2(H_{\hat{m}})} \tag{7}$$

and

$$r = \frac{\overline{H^2_{\hat{m}}}}{\sigma^2(H_{\hat{m}})} \tag{8}$$

with the relevant values of $H_{\hat{m}}$ and $\sigma(H_{\hat{m}})$ listed in Table 6.1. Also included in the table is a measure, cl(%), which signifies the goodness of the parameterization which is the maximum percentage deviation of the calculated probability for a given value of m.

There is one important advantage with the $H_{\hat{m}}$ test: if there is only power in the m^{th} harmonic which is sufficiently strong to be picked up by the Hart rule, the noise content of all $m-1$ harmonics will be added to $H_{\hat{m}}$ and the larger this m, the more likely it will be that $\mathcal{H}_o$

PARAMETERS OF THE H_M TEST

PARAMETER	M									
	1	2	3	4	5	6	7	8	9	10
$\bar{H}_M$	2.040	4.002	4.673	5.096	5.415	5.642	5.84	6.02	6.09	6.24
Δh^a	0.001	0.003	0.005	0.007	0.011	0.15	0.02	0.03	0.03	0.04
$\sigma(H_M)$	1.980	2.840	3.210	3.46	3.67	3.83	3.95	4.13	4.15	4.14
$\Delta\sigma^a$	0.002	0.005	0.008	0.01	0.02	0.02	0.03	0.04	0.05	0.06
cl(%)	17	17	17	17	10	10	5	10	10	10

PARAMETER	M									
	11	12	13	14	15	16	17	18	19	20
$\bar{H}_M$	6.33	6.43	6.57	6.62	6.66	6.87	6.94	7.27	6.98	7.55
Δh^a	0.05	0.07	0.08	0.10	0.13	0.17	0.20	0.24	0.32	0.36
$\sigma(H_M)$	4.30	4.42	4.48	4.53	4.73	4.91	4.87	4.86	4.76	5.71
$\Delta\sigma^a$	0.08	0.09	0.10	0.12	0.14	0.14	0.15	0.15	0.17	0.14
cl(%)	8	5	7	7	5	9	9	10	10	10

NOTE.—Δh is the error in $\bar{H}_M$ and $\Delta\sigma$ is the error in $\sigma(H_M)$.

[a] 90% confidence limits.

Table 6.1. Parameters of the $H_{\hat{m}}$ test. From de Jager et al., 1988.

will be accepted. If this m is large $m > 5$, which is unlikely for real sources, the value of $H_{\hat{m}}$ will be nearly consistent with the null hypothesis and the $H_{\hat{m}}$ test will act like a combination of the Runs test and Pearson's which is desired.

6.3 Kernel Density Estimators

6.3.1 The mathematical properties of kernel functions

The Kernel Density Estimator (KDE) method for the estimation of light curves is an alternative to the histogram estimator, which has a number of disadvantages as discussed previously. It is a smoothed general moving average procedure, the very important smoothing parameter is chosen from the data itself in order to minimise the MISE and requires no arbitrary choices (for example, the choice of the number of bins to use in the histogram estimator). Although the KDE estimates the true light curve with a smooth function, a complementary method based on cluster analysis has recently been proposed (Buccheri et al., 1988) to investigate the small-scale structure of the light curve. Although a full investigation of cluster analysis is beyond the scope of this thesis it is discussed in Appendix 2.

The mathematical-statistical concept of the KDE was introduced by Rosenblatt (1956) and Parzen (1962). It is the weighted average over the distribution function $F_n(x)$ of the sample of event phases. The concept of the KDE is introduced as follows : let $X = x_1, ..., x_n$ be the random sample of phases with a probability density function $f(x)$ where x is the random variable on the real line. The KDE at any point is given by

$$\hat{f}(x; X) = \frac{1}{n} \int_{-\infty}^{\infty} \mathcal{K}((x - y)/h) dF_n(y) \tag{9}$$

performing the integration over the finite sample size,

$$\hat{f}(x, X) = \frac{1}{nh} \sum_{i=1}^{n} \mathcal{K}((x - x_j)/h) \tag{10}$$

here $\mathcal{K}$ is the kernel function evaluated at the point $((x - x_j)/h)$ which does the weighting. The function will be assumed to satisfy the following conditions (Swanepoel 1987) :

- $\mathcal{K}$ is a bounded density function, symmetric around zero, with support on the interval [-x,x] for some constant $x > 0$ which can be infinity,

- the variance of $\mathcal{K}$ should be finite.

Table 6.2 lists some well-known kernel functions and some of their properties.

In order to arrive at expressions for the MSE, the MISE and the optimal smoothing parameter it is best to write equation (9) in terms of a Fourier expansion (Parzen, 1962)

$$\hat{f}(x; X) = \frac{1}{2\pi} \int_{-\infty}^{\infty} \exp(-ilx) k(hl) \hat{R}_l dl \tag{11}$$

where the Fourier transform of the kernel function $\mathcal{K}$(x) is given by :

$$k(hl) = \int_{-\infty}^{\infty} \exp(-i(hl)x) \mathcal{K}(x) dx \tag{12}$$

In the case of periodic data one is only concerned with periodic densities. Furthermore the variable x is substituted with $\theta \in [0, 2\pi]$, so that l can assume only integer values in equation (12). The latter reduces to a Fourier series expansion :

$$\hat{f}(\theta; \Theta) = (1 + 2 \sum_{l=1}^{\infty} k(hl)(\hat{\alpha}_l \sin l\theta + \hat{\beta}_l \cos l\theta))/2\pi \tag{13}$$

Table 2.1. Examples of kernel functions and related parameters.

Name of kernel function	Kernel function K(x)	positive/ negative	Fourier transform[2] k(u)	r	k_r	MISE/A [3]	relative CPU time [4]	$\int_{-\infty}^{\infty} K^2(y)dy$
Naive	$\frac{1}{2}$, $\lvert x\rvert \le 1$ 0, $\lvert x\rvert > 1$	+	$\frac{\sin u}{u}$	2	$\frac{1}{6}$	0,463	10^{10}	0.5
Picard	$\frac{1}{2} e^{-\lvert x\rvert}$	+	$(1 + u^2)^{-1}$	2	1	0,948	10^{5}	0.5
Normal	$(2\pi)^{-\frac{1}{2}} e^{-\frac{1}{2}x^2}$	+	$e^{-\frac{1}{2}u^2}$	2	$\frac{1}{2}$	0,454	7	0.282
Epanechnikov	$\frac{3}{4}(1-t^2)$, $\lvert t\rvert \le 1$ 0 , $\lvert t\rvert > 1$	+	$\frac{3}{u^2}\left(\frac{\sin u}{u} - \cos u\right)$	2	$\frac{1}{10}$	0,437	10^{10}	0.6
Fourier integral estimate	$\frac{\sin x}{\pi x}$	+/-	1 $\lvert u\rvert < 1$ $\frac{1}{2}$ $\lvert u\rvert = 1$ 0 $\lvert u\rvert > 1$	-	-	-	~ 6	-
Swanepoel	$\frac{1}{2}(\sin\lvert x\rvert + \cos x)e^{-\lvert x\rvert}$	+ +/-[1]	$\frac{4}{4 + u^4}$	4	$\frac{1}{4}$	0,436	316	0.375

(1) The Swanepoel kernel allows only slight negativity.

(2) $k(u) = \int_{-\infty}^{\infty} \exp(-iuy)K(y)dy$ with $u = ht$

(3) $A = \left(\int_0^{2\pi} (f^{(r)}(\theta))^2 d\theta\right)^{1/(2r+1)} n^{-2r/(2r+1)}$

(4) The relative CPU time is defined as the number of terms i necessary for k(ht) to decrease to 10^{-10} level if h = 1.

Table 6.2. Examples of kernel functions and related parameters. From de Jager, 1987.

where $\Theta = \theta_1, ..., \theta_n$ are the folded event phases, $\hat{\alpha}_l$ and $\hat{\beta}_l$ are the trigonometric moments and $\hat{f}(\theta; \Theta)$ is a normalised density function between 0 and 2π.

Equation (13) is easy to work with in terms of computing the KDE of the light curve. The first twenty harmonics are calculated from the data (and possibly used for the $H_{\hat{m}}$ test), the smoothing parameter estimated (see next section) and then the density function calculated from (13) in as many points θ as one wishes.

6.3.2 The optimal smoothing parameter

It can be shown (de Jager, 1987) how the MSE of the kernel estimator may be written in terms of a sum of the variance and bias terms. The variance depends on the amplitude of the density, while the bias depends on the absolute value of the derivative of the light curve. Thus, in regions where the light curve is flat (background) or where the slope of the density estimate is constant, one can trust the variance to be a sufficient indicator of the true error. However, where the slope of the KDE changes rapidly, for example, on the tip of a narrow peak, the bias can be expected to be larger than the variance. Integrating the MSE, the MISE is also the sum of the variance and bias components. Fig.6.1. shows the behaviour of the variance and bias components as a function of smoothing parameter h. The variance is inversely proportional to the smoothing parameter while the bias increases with h. Thus there exists an optimal choice for h, say h^*, such that the MISE is a minimum. This value can be obtained by differentiating the expression for the MISE with respect to h. By setting the result equal to zero, the optimal value of h is obtained. An estimate of the smoothing parameter, $\hat{h}$, is given by

$$\hat{h} = \underset{h}{MINIMUM} \sum_{l=1}^{\infty} [(k(hl))^2 \overline{R_l^2} - 2k(hl)(n\overline{R_l^2} - 1)/(n-1)] \qquad (14)$$

This minimisation therefore yields a value $\hat{h}$ such that $E(\hat{h}) = h^*$.

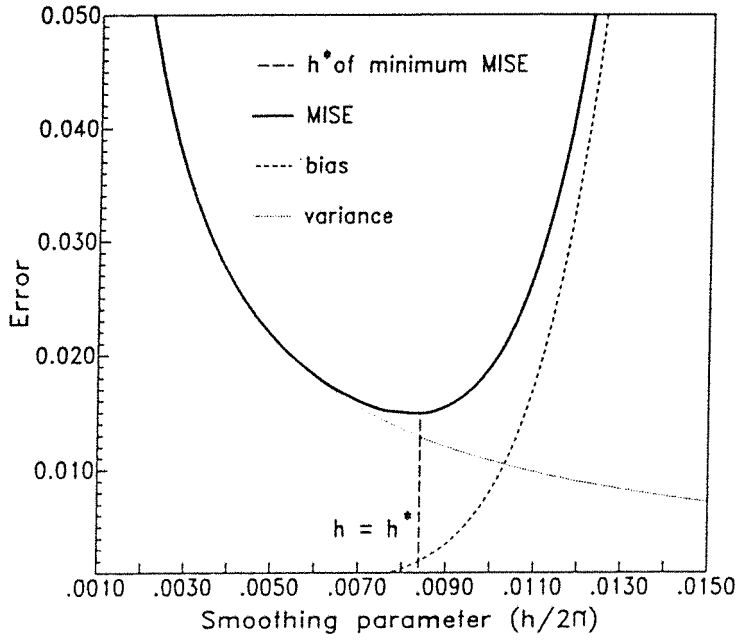

Fig.6.1. The behaviour of the varience and bias terms as a function of smoothing parameter h showing there exists a unique minimum error term. From de Jager, 1987.

6.3.3 Choice of Kernel

Clearly there are a great number of different kernel functions to choose from. Recently the kernel function

$$K(x) = \frac{1}{2}(\sin|x| + \cos x)\exp(-|x|) \tag{15}$$

was proposed (Swanepoel 1987) and it was shown that this kernel function yields the best KDE with respect to all other kernels. It was also shown that the MISE decreases to zero faster than the other kernels and faster than the histogram estimator. Thus the Swanepoel kernel is asymptotically the best to use for all possible light curves.

6.3.4 Confidence bands for Kernel Density Estimators

An approximate confidence interval for the KDE can be estimated from the standard error of the KDE and use of the consistency property (de Jager 1987). The standard error of the KDE is approximated by the variance component of the MSE, however, this cannot be said to form a confidence band. An inflationary factor has to be taken into account (Bickel and Rosenblatt 1973) which increases the magnitude of the confidence band. For the Swanepoel kernel, this yields the confidence band

$$\hat{f}(\theta;\Theta) = f(\theta;\Theta) \pm 3(0.375 f(\theta;\Theta)/h)^{1/2} \tag{16}$$

for a $\pm 3\sigma$ confidence band around the KDE. Note that the error bars found on histogram estimators are confidence intervals and not a true confidence band. They will always be larger than the corresponding confidence band associated with a KDE due to the large bias associated with the histogram estimator.

6.3.5 Examples of the use of Kernel Density Estimators

Fig.6.2. shows an estimate of the Vela pulsar light-curve at energies $E_\gamma > 50$ MeV. The Swanepoel kernel was used. The sample size is 3462 and the optimal smoothing parameter is $\hat{h}$= 0.0085 with a 2σ confidence band (de Jager 1987).

Fig.6.3. shows a KDE of very high energy gamma rays from PSR 1509-58 and a histogram estimator for comparison (de Jager et al., 1988). The differential number is defined as the density estimate times the sample size. The KDE clearly shows the surprising triple peaked density associated with the pulsar light-curve.

Fig.6.4. shows a gaussian kernel function used to determine the modulation curve for solar flares observed on board the ISEE-3 spacecraft (Droge, private communication). The confidence band is 1σ.

6.3.6 Disadvantages of the KDE technique

The kernel density estimator technique is clearly an advantage over the traditional histogram technique. However, it does have the slight disadvantage of only estimating global smoothing and a global confidence band. The smoothing and confidence band should really reflect the density at a particular phase region. Work is presently underway to modify the KDE technique to incorporate this improvement, that is, to have a KDE with a phase dependent smoothing and confidence band estimator (de Jager, private communication).

The theoretical aspects of the KDE technique having been discussed in this chapter, it is now time to put them into practise. Fortunately, the *MIFRASO* observations of the Crab Pulsar made in 1986 and 1987 provided an ideal opportunity on which to try out the new techniques. The motivation to do so was entirely the author's, and the results form the basis of the next chapter.

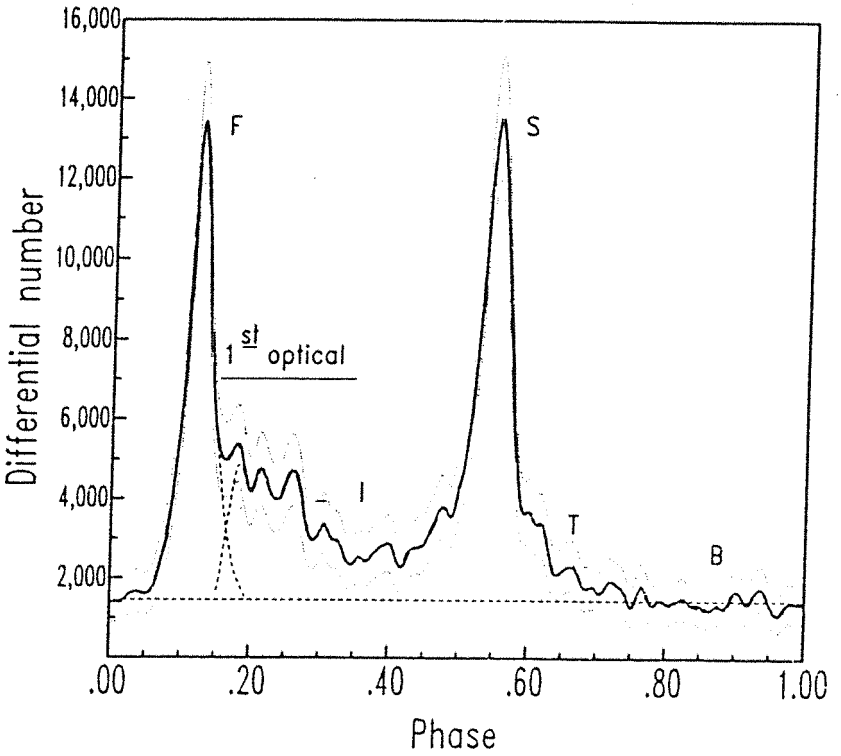

Fig.6.2. An example of the use of kernel density estimators : the Vela pulsar light curve analysed using the Swanepoel kernel. From de Jager, 1987.

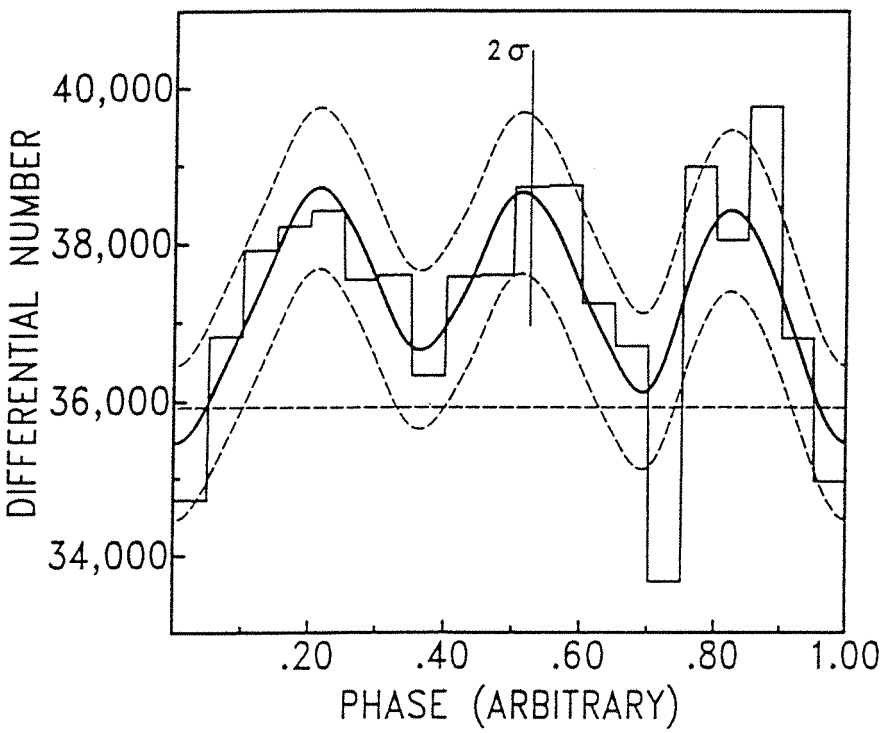

Fig.6.3. A kernel density estimator of the pulsar PSR 1509-58 showing the surprising triple-peaked density. Also shown is a histogram estimator for comparison. From de Jager et al., 1988.

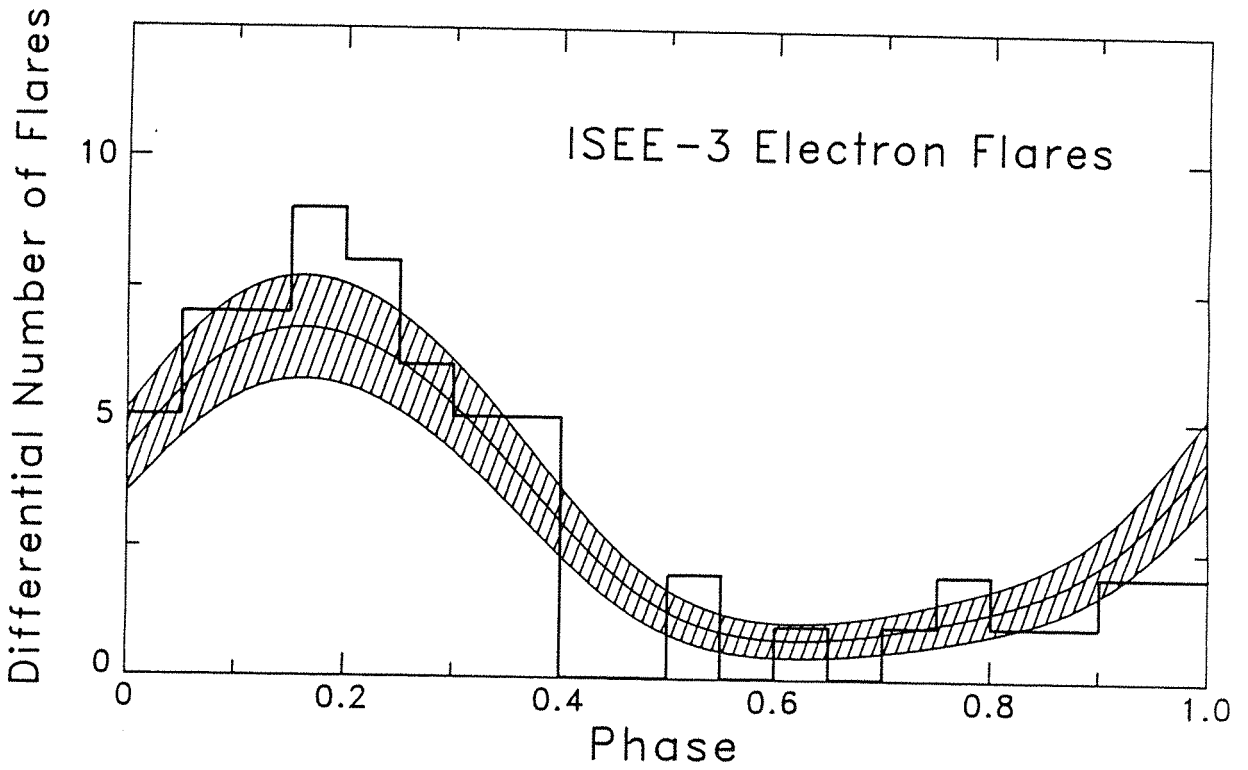

Fig.6.4. A gaussian kernel function used to determine the modulation curve for solar flare observations. From Droge et al., private communication.

CHAPTER 7 : *MIFRASO* OBSERVATIONS OF THE CRAB PULSAR : FAST TIMING ANALYSIS USING THE $H_{\hat{m}}$ TEST AND THE KERNEL ESTIMATOR TECHNIQUE

7.1 Introduction

This chapter outlines the application of the kernel density estimator technique and its associated statistic for phase uniformity to the *MIFRASO* observation of the Crab Pulsar. The Crab Pulsar is a good choice of object on which to try out the new techniques as it has a pulse period and a pulse profile that are well-known in the hard X-ray band.

7.2 The Observations of the Crab Pulsar

Three separate observations of the Crab region were made by the *MIFRASO* telescope, a tracking scan and a drift scan during the 1986 flight and a single drift scan during the 1987 flight. The durations of the scans were 738 s.,972 s. and 1080 s. respectively, not including data dropouts. The telescope was near the Milo-Trapani launch site when the Crab observations were made (they were first in the programme) and thus the telemetry quality was excellent throughout the observations, and so data dropouts were kept to a minimum.

All of the high energy detectors functioned throughout the duration of the two flights. During the 1986 flight, however, a breakdown in the high-tension supply to the low energy detectors impaired their performance to such a degree that no useful data has been recovered from them. They were fully operational during the 1987 flight.

Analysis of the flight tapes proceeded as outlined in Chapter 3 with the event times being barycentered and then folded for a full period search of the tracking scan to confirm the timing performance of the telescope, and to demonstrate the power of the $H_{\hat{m}}$ test. The folded phases were then analysed using the kernel density estimator technique to produce the light curves.

7.3 Barycentric Reduction

A pulsed source when observed from a moving frame of reference results in a variation of apparent period due to the Doppler effect. The magnitude and the sign of this period change depends upon the velocity of the observatory and its direction relative to the source vector . However, in the case of terrestrial or satellite borne telescopes additional complications arise due to motion through the varying gravitational field of the solar system. These effects have to be taken into account if one wants to do precision timing measurements.

Historically the need to make corrections for Doppler and gravitational red-shift effects arose with the discovery of pulsars in 1967 . At present there are over 500 known pulsars with periods ranging from 1.6 ms to 4.3 s. Due to the Earth's rotation and its motion around the Sun the apparent period of a pulsed source appears to modulate with components of 24 hrs and 365.2422 days. Furthermore the effects of the Earth's precession and nutation (wobble of rotation axis around precession orbit), together with the slowing down of the Earth and irregularities in its rotation must all be included.

The barycentric reduction for the *MIFRASO* observations was carried out using three different methods to cross-check the results. The sophisticated pulsar timing program PSRTIME at the Nuffield Radio Astronomy Laboratories, Jodrell Bank was used together with the monthly Crab Pulsar timing results as the main barycentring routine (Lyne and McKenna, private communication; Lyne and Pritchard, 1988). As verification of these results, the program BAT from the Cygnus collaboration was also used (Lloyd-Evans, private communication). This last routine used the Lincoln Labs ephemeris, which unfortunately only covered the years up to 1986. To barycentre the 1987 observation, a new routine was written (Lloyd-Evans, private communication). This new barycentring routine used the JPL DE200/LE200 ephemerides (Standish 1982). All produced consistent results. To check that the passage of the balloon during the course of the observations had no effect upon the barycentring the barycentring was repeated for selected

coordinates of the balloon's passage.

The form of the barycentring was a first-order linear interpolation of the event times. Consider a topocentric (site) time T_{topo} bracketed by two event times $TT1$ and $TT2$. If the equivalent barycentric times are $TB1$ and $TB2$ then

$$\frac{T_{bary} - TB1}{TB2 - TB1} = \frac{T_{topo} - TT1}{TT2 - TT1} \tag{1}$$

where T_{bary} is the equivalent barycentred time and is simply obtained from (1) as

$$T_{bary} = [\frac{T_{topo} - TT1}{TT2 - TT1}] \times (TB2 - TB1) + TB1 \tag{2}$$

This is equivalent to a first-order Doppler shift of the source period defined by

$$\beta = \frac{P_{bary}}{P_{topo}} = \frac{T_{bary} - TB1}{T_{topo} - TT1} \tag{3}$$

where P_{topo} is the observed period and P_{bary} the period at the barycentre.

The two first-order barycentric corrections to the source frequency are shown in Table 7.1 below.

year	barycentring factor
1986	1.0000658333
1987	1.0000464240

Table 7.1 The barycentring factors for both balloon flights.

7.4 Absolute Crab phase

The arrival times of the primary pulse from the Crab Pulsar at the barycentre of the Solar System are given by the Jodrell Bank ephemeris both using the MIT (PEP311) ephemeris and by using the JPL (DE200) ephemeris. The arrival time is given in Barycentric Dynamical Time (TDB). To obtain the TDB of the X-ray pulse from the *MIFRASO* telescope the UT of the events comprising the primary X-ray pulse must be converted into TDB. This is done by first obtaining the clock correction at the Milo-Trapani base to convert the UT on-board the *MIFRASO* telescope to corrected Universal Time UTC. The UTC is then corrected to Terrestrial Atomic Time (TAI). TAI is then corrected to Terrestrial Dynamic Barycentred time and then the TDB event time barycentred.

Unfortunately the comparison of the absolute phase could not be done because of two sources of unknown timing delays. It was not possible to obtain the correction needed to convert the UT stamp on the subframe data into UTC, that is, it was not possible to find the position on the subframe which corresponded to the UT stamp placed at the start of that subframe. Furthermore, the correction needed to transform UTC into TAI was not known at the Milo-Trapani base, so this correction could not be made for both flights of the *MIFRASO* telescope. Hence no calculation of the absolute phase of the Crab Pulsar could be made.

7.5 Kernel Density Estimators of the Three Pulse Profiles

The four kernel density estimates of the Crab Pulsar pulse profiles are shown in Figs 7.1, 7.2, 7.3 and 7.4 for the 1986 track (HED), 1986 drift scan (HED) and the 1987 drift scan respectively (HED and LED). Preliminary results have already been published (Carstairs et al., 1989) and a fuller treatment is under preparation. (Carstairs et al., 1992). The advantages of the KDE method are clear in that there is more detail resolved in the profile by using the new technique than can be made clear with the arbitrary binning into a histogram. Table 7.2 shows the parameters associated with each of the HED observations of the Crab Pulsar.

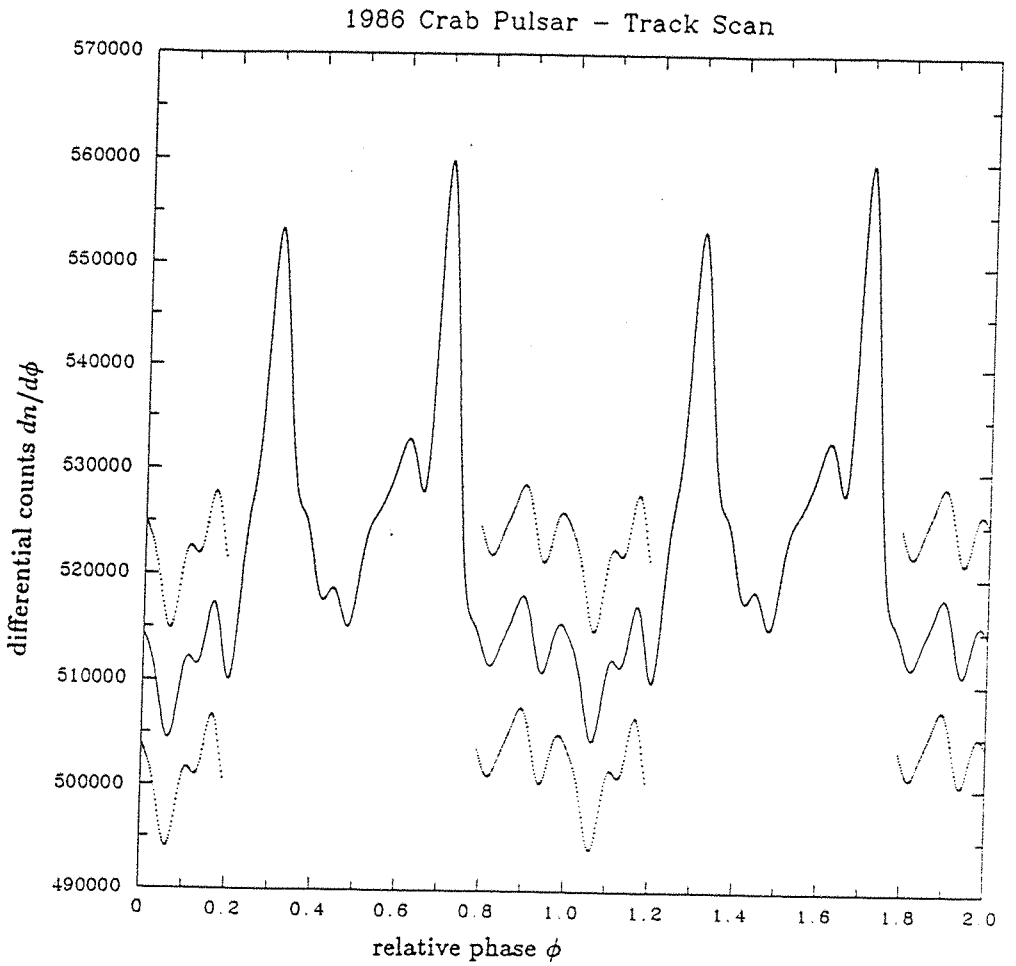

Fig.7.1. The kernel density estimator of the hard X-ray light curve from the Crab pulsar as observed using the high energy detectors of the *MIFRASO* telescope during the 1986 tracking scan of the Crab. The dotted confidence band shown is $\pm 3\sigma$ around the density estimate of the unpulsed region. The profile is repeated once for clarity.

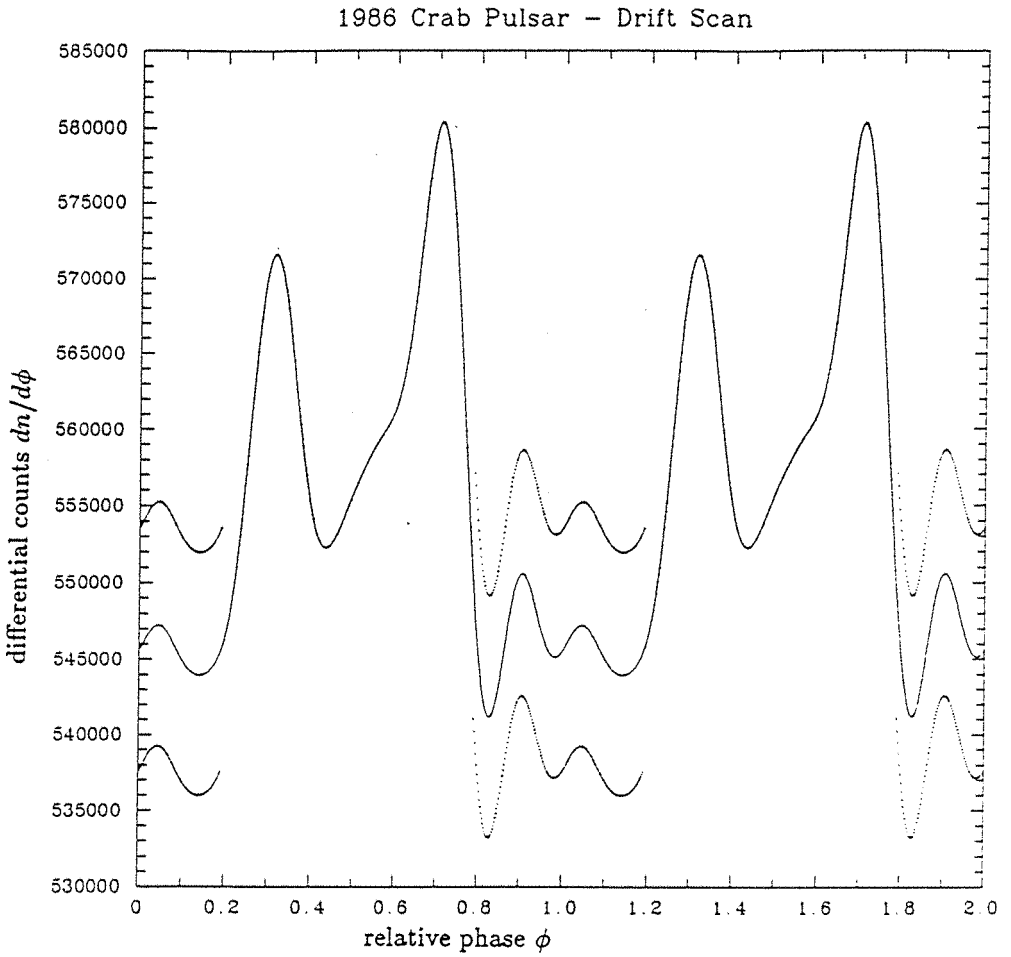

Fig.7.2. The kernel density estimator of the hard X-ray light curve from the Crab pulsar as observed using the high energy detectors of the *MIFRASO* telescope during the 1986 drift scan of the Crab. The dotted confidence band shown is $\pm 3\sigma$ around the density estimate of the unpulsed region. The profile is repeated once for clarity.

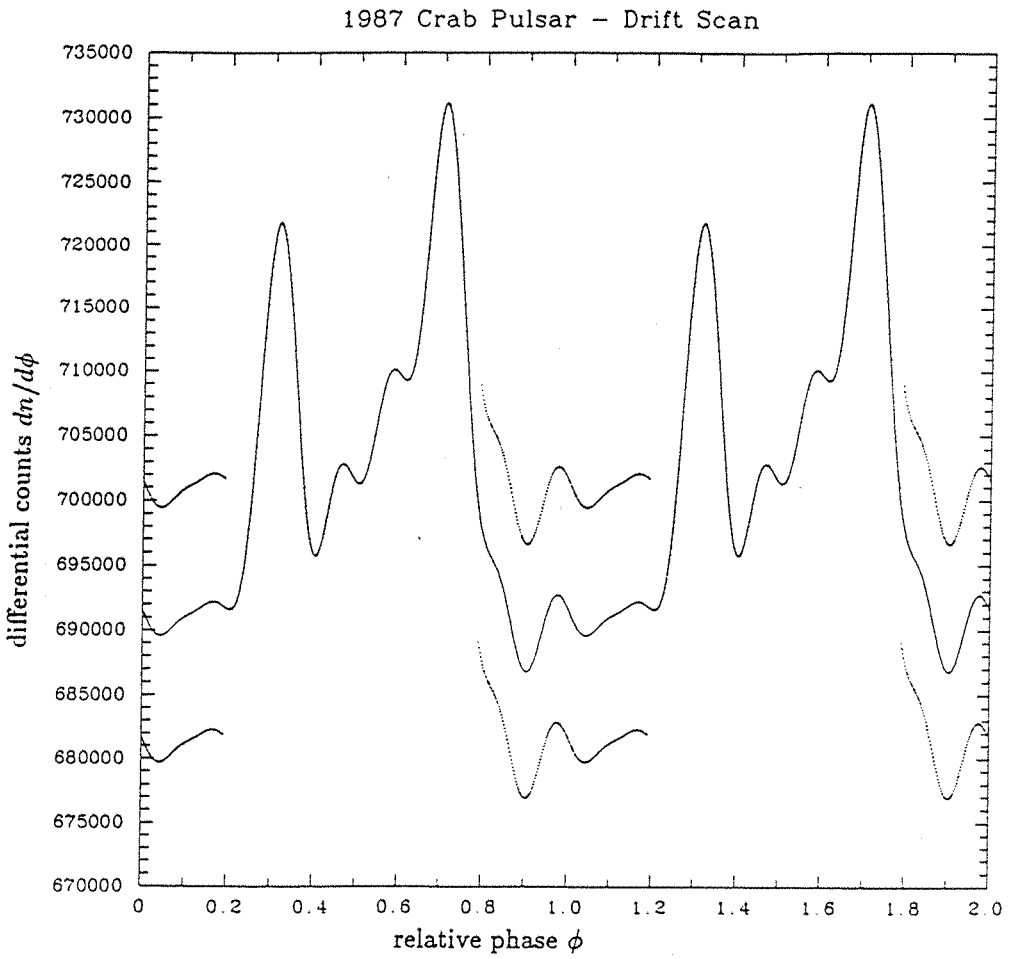

Fig.7.3. The kernel density estimator of the hard X-ray light curve from the Crab pulsar as observed using the high energy detectors of the *MIFRASO* telescope during the 1987 drift scan of the Crab. The dotted confidence band shown is $\pm 3\sigma$ around the density estimate of the unpulsed region. The profile is repeated once for clarity.

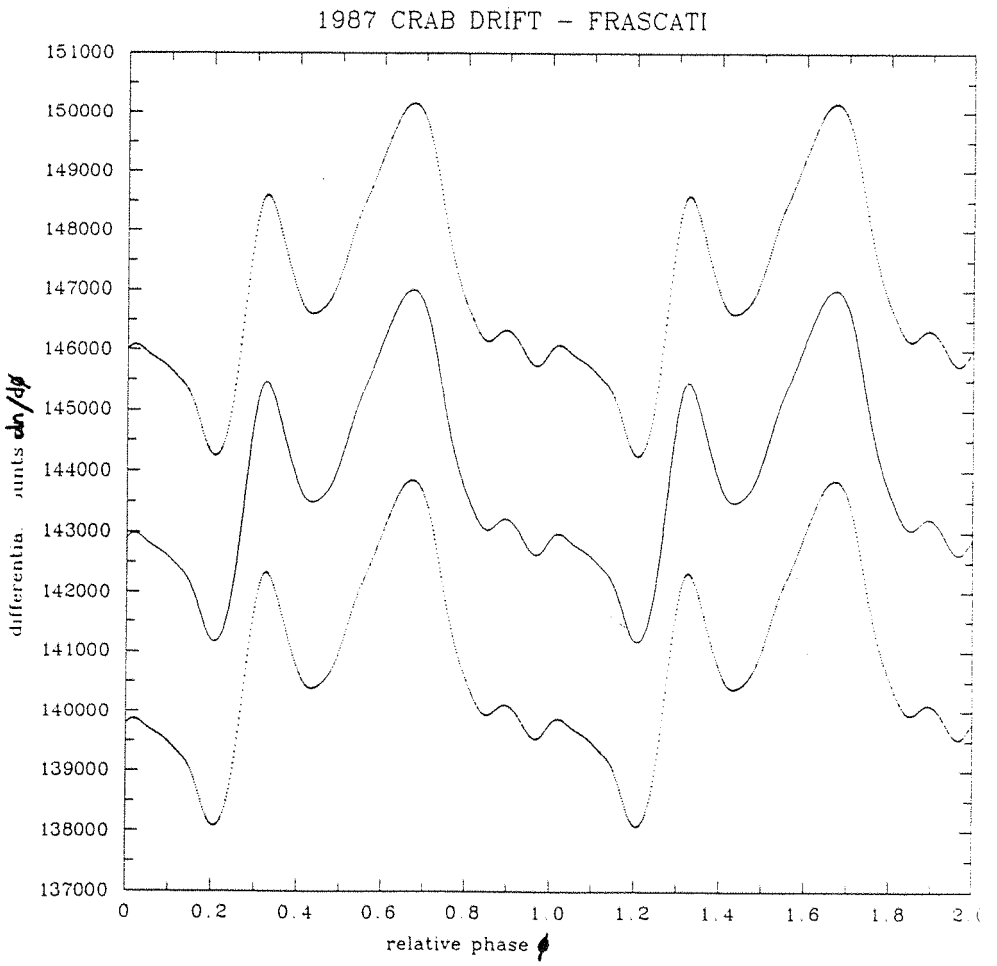

Fig.7.4. The kernel density estimator of the hard X-ray light curve from the Crab pulsar as observed using the low energy detectors of the *MIFRASO* telescope during the 1987 drift scan of the Crab. The dotted confidence band shown is $\pm 3\sigma$ around the density estimate. The profile is repeated once for clarity.

Crab Pulsar Scan	Scan Length/ secs	Number of Events n	Optimum Harmonics $\hat{m}$	Smoothing Parameter $h/10^{-2}$	Equiv. Bins per Phase	Statistical Significance σ
1986 Track	738	522 372	15	1.57	32	12
1986 Drift	972	555 565	7	2.88	17	11
1987 Drift	1080	701 590	8	2.39	21	11

Table 7.2. A summary of the KDE parameters for the three HED observations of the Crab pulsar made with the *MIFRASO* telescope.

Fig.7.5 shows the three data sets added together. This represents the total *MIFRASO* database on the Crab Pulsar. Also shown is the corresponding histogram estimator for the complete observation set for comparison. The addition was carried out using a weighted sum of the twenty harmonic moments of the individual pulse profiles (de Jager, private communication). For k observations (separate pulse profiles) we have

$$N = \sum_{i=1}^{k} n_i \tag{4}$$

where N is the total number of event phases. Defining the separate harmonic moments by

$$\alpha_i(p) = \frac{1}{n_i} \sum_{j=1}^{n_i} \sin p\theta_j \tag{5}$$

and

$$\beta_i(p) = \frac{1}{n_i} \sum_{j=1}^{n_i} \cos p\theta_j \tag{6}$$

for harmonics 1 to p. The weighted summed harmonic moments $\hat{\alpha}$ and $\hat{\beta}$ are then given by

$$\hat{\alpha} = \frac{1}{N} \sum_{i=1}^{k} n_i \alpha_i(p) \tag{7}$$

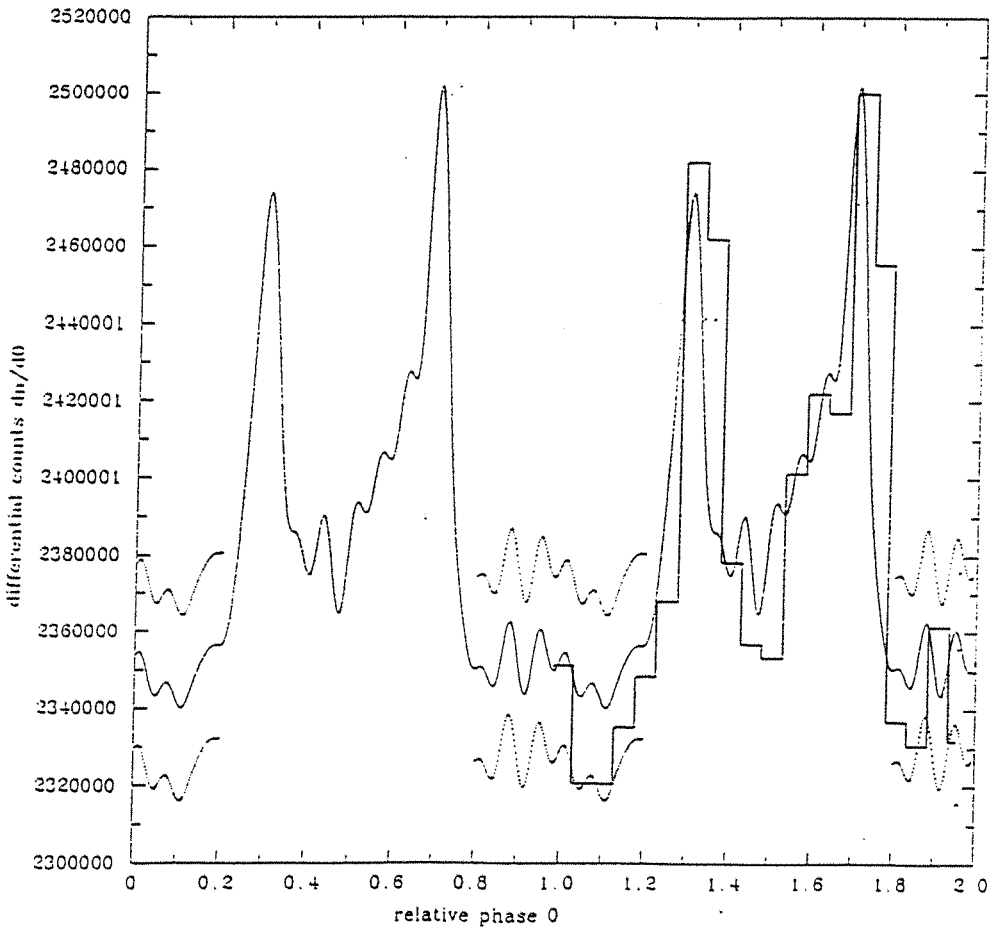

Fig.7.5. The kernel density estimator for the weighted sum of all the *MIFRASO* observations of the Crab pulsar. This represents the total timing database of observations. In the absense of absolute phase information the 1987 profiles have been adjusted in relative phase to align them with the 1986 observations. The dotted confidence band is $\pm 3\sigma$ around the unpulsed emission. A histogram estimator is included for comparison.

and

$$\hat{\beta} = \frac{1}{N} \sum_{i=1}^{k} n_i \beta_i(p) \tag{8}$$

All of the pulse profiles are consistent in the general features associated with the Crab pulse profile at these energies. All show the classical bimodal form with considerable structure in the interpulse region (defined as the region lying between the two pulses). The secondary pulse is separated from the primary pulse by a phase of approximately 0.4, and the secondary pulse is greater in amplitude than the primary pulse. Regarding the pulse profile for the complete set of observations, there is considerable structure within the interpulse region with hints of a sub-pulse at relative phase 0.45 together with a further sub-pulse at relative phase 0.90. Both sub-pulses are approximately at the 3σ level according to the confidence band. A cluster density estimator (CDE) analysis would be needed to accurately determine the statistical significance of these features, see Appendix 2. Such features provide an important guide to models of the emission regions of the pulsar (see Chapter 9). It is interesting to note that the *FIGARO II* balloon borne telescope observing in the range 0.2-6 MeV (Agrinier et al., 1990) found possible sub-pulses at relative phases 0.5 and 0.8, using the histogram method with 60 bins per phase. It would be instructive to apply the KDE and CDE techniques to the *FIGARO II* observations.

7.6 'Consistency' Statistics applied to the three observations

Given the three separate observations of the Crab Pulsar and their analysis by the KDE technique, it is instructive to ask the question 'are the three pulse profiles consistent with one

another ?'. That is, given the three sets of Rayleigh harmonics α_i^k and β_i^k, where $i = 1, 20$ is the harmonic number and $k = 1, 3$ the observation number, what is the probability that the three sets are consistent up to a harmonic i ?

This question can be answered by use of the Rayleigh 'consistency' statistics L and M. Both statistics are used to test a set of n independent vectors (Lloyd-Evans, private communication). The L statistic is defined as

$$L = \sum_{k=1}^{n} 2K0_k \tag{9}$$

where

$$K0_k = n_k(\alpha_k^2 + \beta_k^2) \tag{10}$$

L is distributed as

$$P(L)dL = \frac{L^{n-1}}{(n-1)!} \exp^{-L} dL \tag{11}$$

and is identical to χ^2 with $2n$ degrees of freedom. L thus tests whether the n scalar amplitudes are all drawn from a uniform distribution.

Similarly, the M statistic is defined as

$$M = 2\left[\left(\sum_{k=1}^{n} K0_k\right) - \mathbf{K_{sum}}\right] \tag{12}$$

where

$$\mathbf{K_{sum}} = n_{sum}\left(\alpha_{sum}^2 + \beta_{sum}^2\right) \tag{13}$$

and M is distributed as χ^2_{2n-2}. The M statistic tests whether all the harmonic amplitudes could be drawn from a distribution described by their resultant, that is, it answers the question 'what is the probability of obtaining the set of harmonics from the same but not necessarily uniform distribution?'.

Once the probabilities have been calculated using the above statistics, the binomial expression $Pr' = 1 - (1 - Pr)^k$ needs to be applied to the resultant probabilities obtained. The 'number of trials' is simply the number of harmonics tested for uniformity, in this case, $k = 20$.

The results of applying the M test to the three sets of harmonics from the 1986 tracking, drift and 1987 drift scans of the Crab region made with the *MIFRASO* telescope are shown in Fig.7.6.

As can be seen from Fig.7.6 the two most significant results from the M test are harmonics number 2 and 3. Thus it can be concluded that the three pulse profiles are consistent up to the third harmonic. This is in agreement with the Rayleigh power spectrum of the pulse profiles being dominated by the first three harmonics (see Fig.7.11).

7.7 Period Searching

7.7.1 Period Searching the Crab data

In order to confirm the radio period that the *MIFRASO* data was folded around, and to confirm the timing performance of the telescope, a routine was developed that incorporated a period searching algorithm using the $H_{\hat{m}}$ test. A small sample set taken from the 1986 tracking

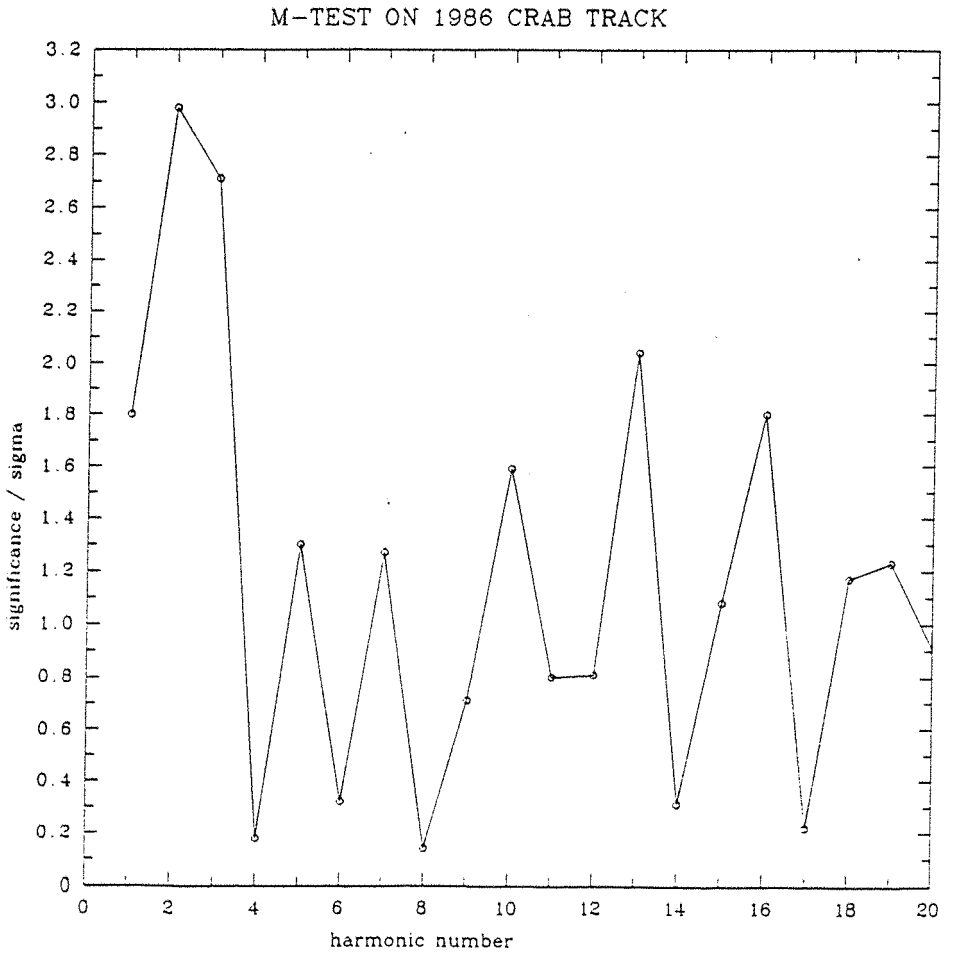

Fig.7.6. The result of applying the M test to the three harmonic series representing the HED observations of the Crab pulsar.

scan was used to compare the performance of the new test with that of the conventional Rayleigh and Pearson tests.2.10^5 events were used in this small sample set, corresponding to 278 seconds of observation time.

7.7.2 Periodicity Searches

The probability distribution of a chosen test for uniformity against a number of trial periods represents a period search. A statistical penalty is paid for any positive effect found that depends on the number and spacing of the set of trial periods used, this penalty reduces the significance of any effect found. Consider a period search conducted around a period P_o on a set of observations of length τ. Two trial periods are said to be Fourier independent if they are separated by a period space Δ where $\Delta = P_o^2/\tau$, and a result with significance level Pr from a search of k independent periods will be decreased to a significance level $Pr' = 1 - (1 - Pr)^k$. Note that this is only strictly true for a pure sinusoid observed for an integral number of periods. For a source density distribution with significant power in higher harmonics Δ should be modified from knowledge of the harmonic content of the source wavefunction. A number of searches may be conducted within Δ as it is unlikely that the most significant detection will lie on integer spacings of Δ. Either of these cases are known as oversampling and its penalty is harder to evaluate. Simulations have been used to estimate the factor of underestimation of a positive effect for various statistical tests (de Jager et al., 1989). These penalties will not be evaluated here because the Crab Pulsar period is known *a priori*, and searches in period are used only to compare the various tests used.

7.7.3 Results and Comparison of Periodicity Searches Conducted using the Pearson, Rayleigh and H_m Tests.

The results of the periodicity searches conducted using the three tests are shown in Figs. 7.7 and 7.8. The absolute values of trial period may be found from $P_{trial} = P_o + n(P_o^2/\tau)$ where P_o = 0.033326846 s ., τ = 278.4 s. and -2$\leq n \leq$ 2.The significance levels quoted here have not

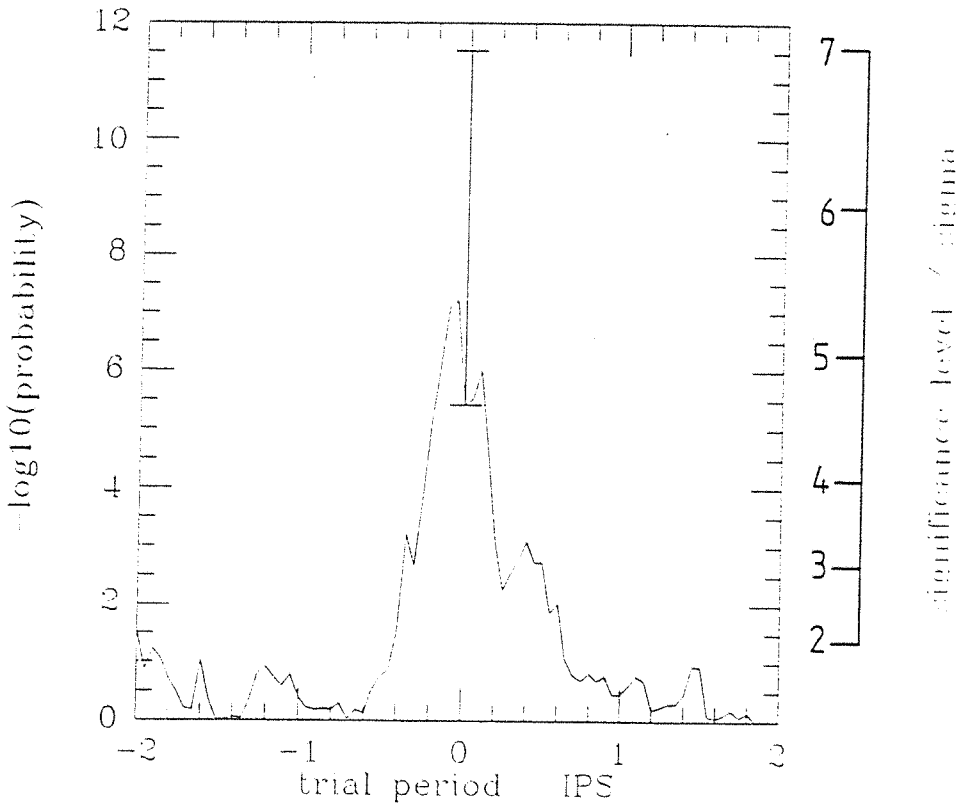

Fig.7.7.(a) The result of a periodicity search made on the 1986 tracking scan data using the Pearson test with 10 bins per phase. The interpolated radio period is at $P_{trial} = 0$. Vertical bar at P_o shows the effect of sliding the phase origin across one bin, see Fig.7.7(e).

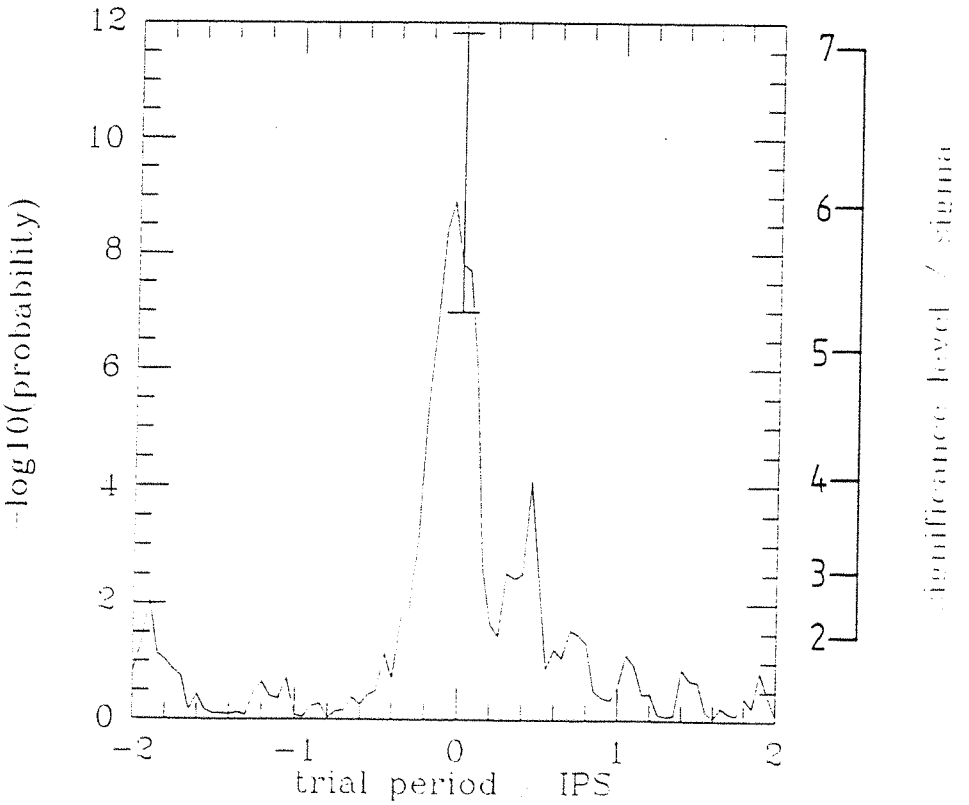

Fig.7.7.(b) The same as Fig.7.7.(a) but using 20 bins per phase for the Pearson test.

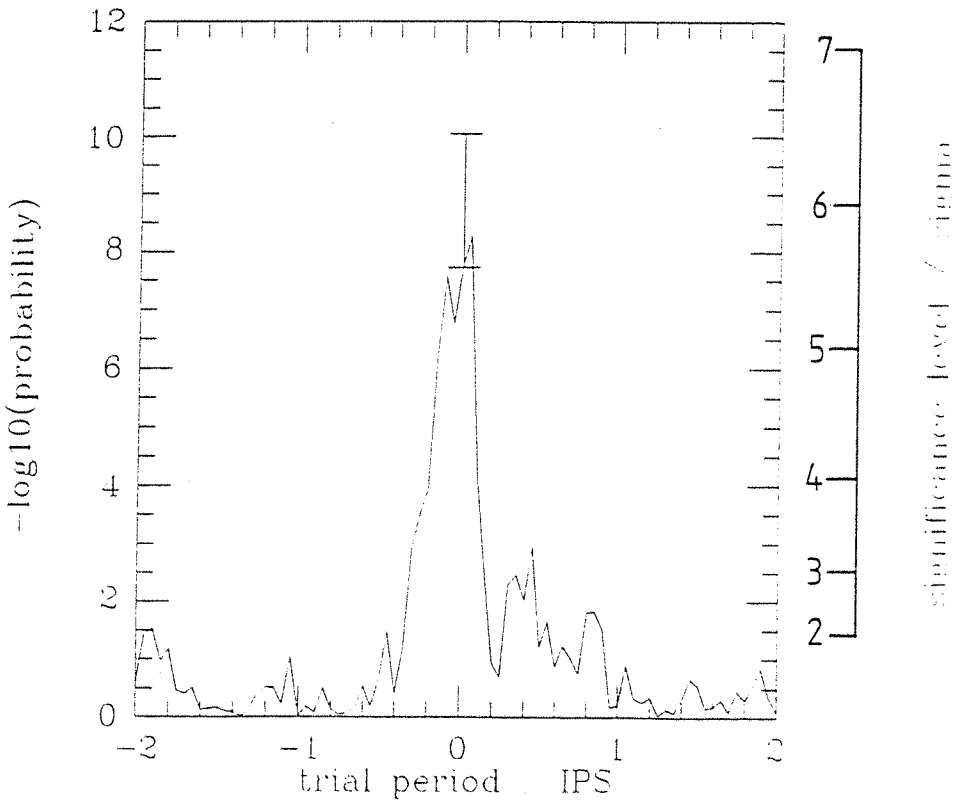

Fig.7.7.(c) The same as Fig.7.7.(a) but using 30 bins per phase for the Pearson test.

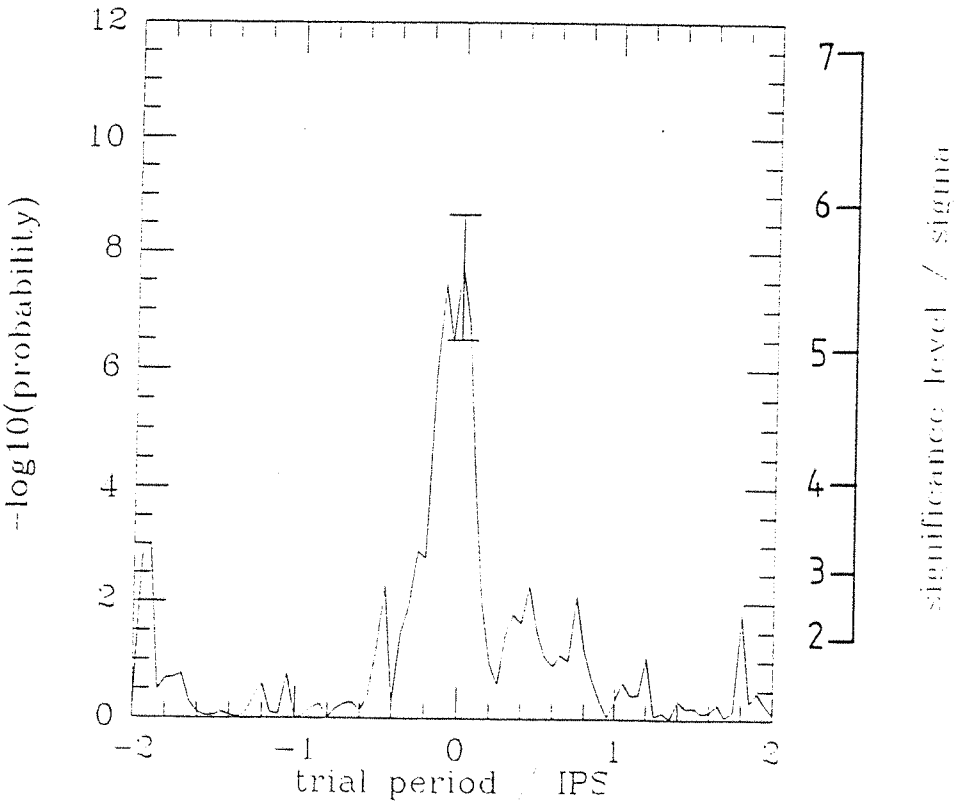

Fig.7.7.(d) The same as Fig.7.7.(a) but using 40 bins per phase for the Pearson test.

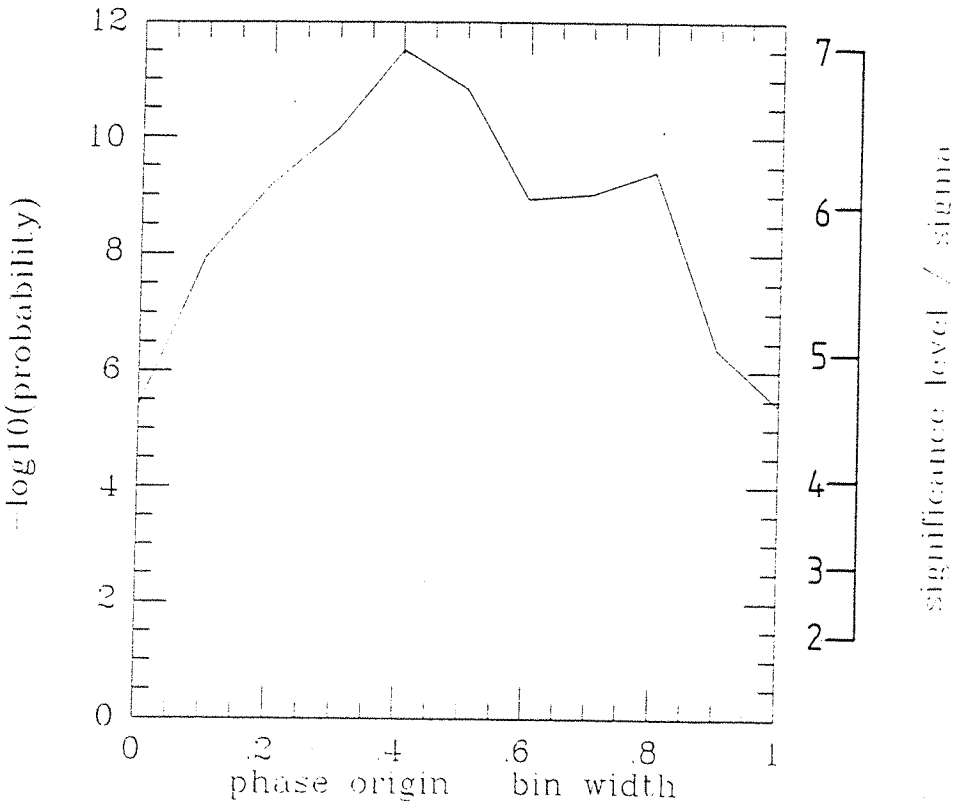

Fig.7.7.(e). The explicit variation in significance experienced with a single fold of the 1986 tracking scan data at P_o sliding across one bin using the Pearson test with 10 bins per phase.

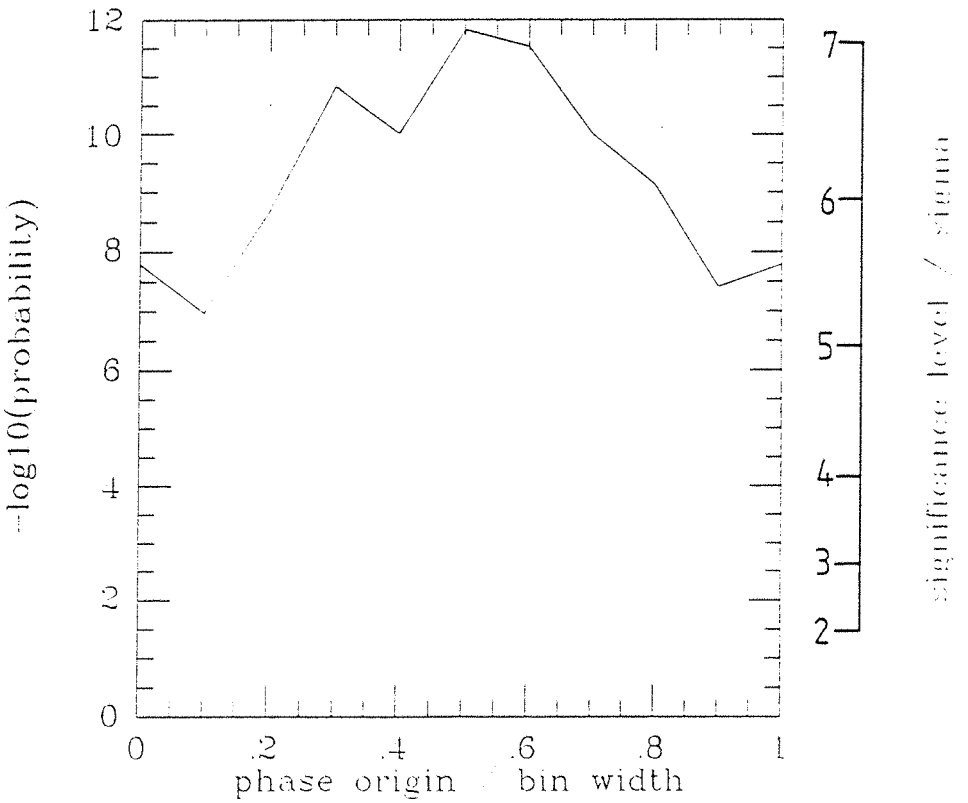

Fig.7.7.(f). The explicit variation in significance experienced with a single fold of the 1986 tracking scan data at P_o sliding across one bin using the Pearson test with 20 bins per phase.

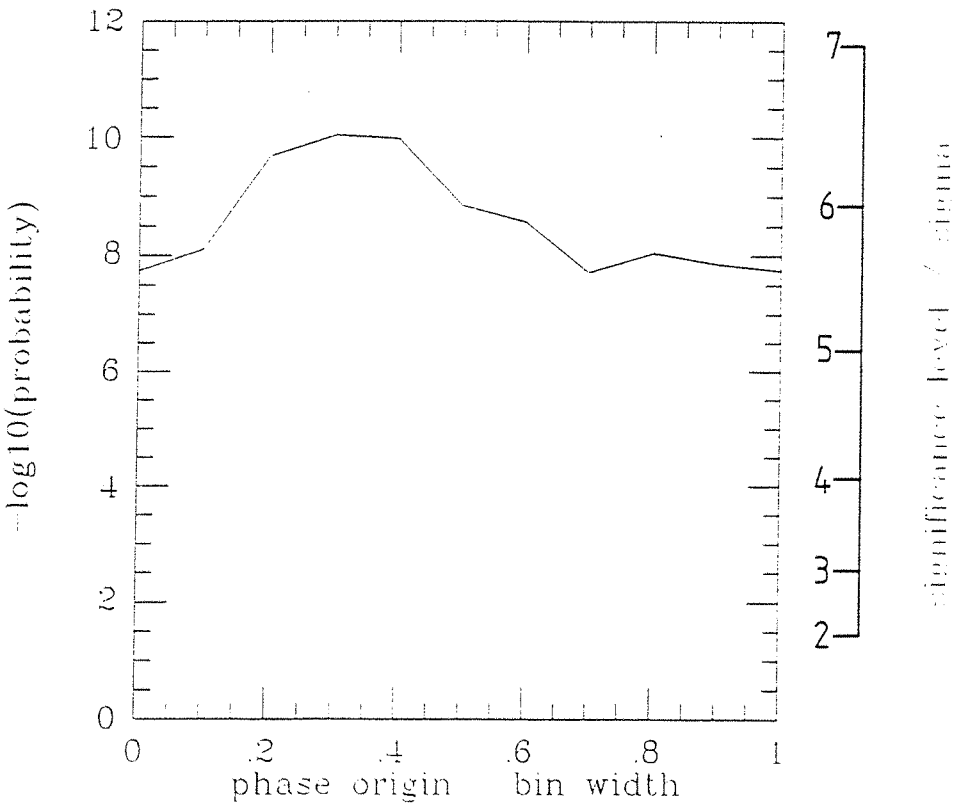

Fig.7.7.(g). The explicit variation in significance experienced with a single fold of the 1986 tracking scan data at P_o sliding across one bin using the Pearson test with 30 bins per phase.

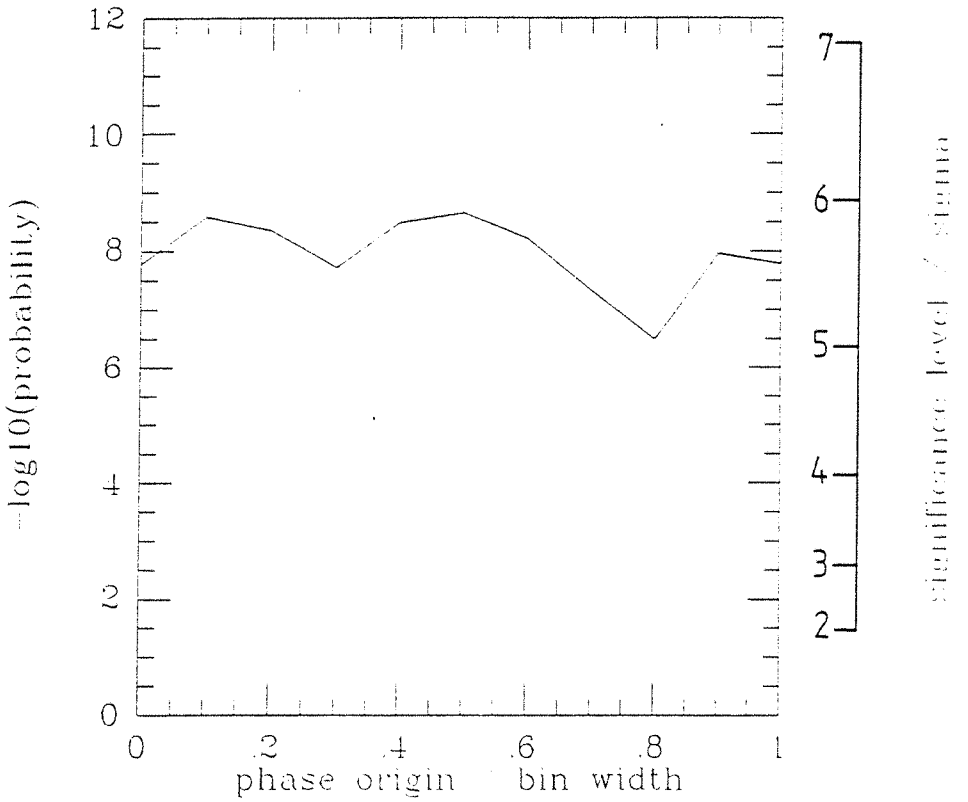

Fig.7.7.(h). The explicit variation in significance experienced with a single fold of the 1986 tracking scan data at P_o sliding across one bin using the Pearson test with 40 bins per phase.

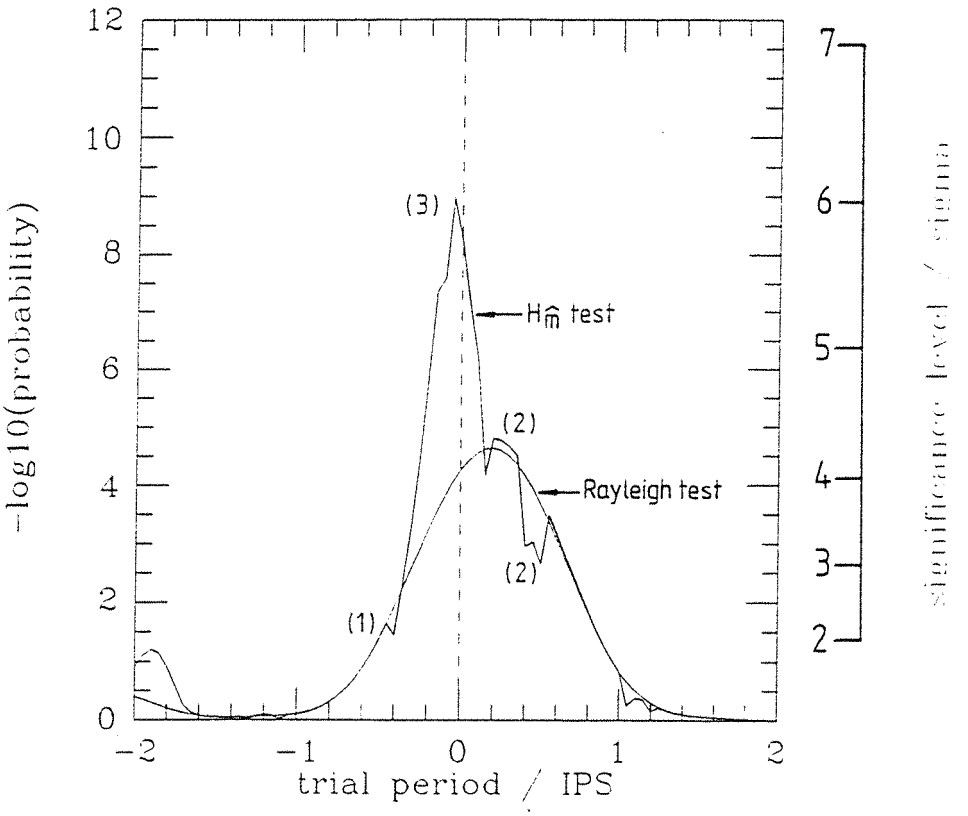

Fig.7.8. Results of a periodicity search made using the same data as for Fig.7.7 but using the $H_{\hat{m}}$ test. Also shown is the Rayleigh power for the search. Numbers in parenthesis refer to the optimum number of harmonics chosen using the Hart rule for the $H_{\hat{m}}$ test.

been corrected for the number of trials. Also shown are the corresponding σ-levels in one-sided normalised Gaussian units. The resultant periodicity searches using b=10,20,30 and 40 bins per phase domain with phase origin o=0.0 using the Pearson test are shown in Fig. 7.7 (a)-(d). The test finds positive detections at $P_{trial} = \pm\frac{1}{20}\Delta$ with significances ranging from 5.4 to 6.1σ. To examine the effect of a change of phase origin, the search was repeated using 11 values of phase origin running from $0.0 \leq o \leq 1.0$ per bin width. The variations in significance level for some permutations of b and o folding at the trial period P_o are shown in Fig. 7.7(e)-(h). These are also displayed as vertical bars on Fig.7.7(a)-(d) at P_o. Note the severe variation in detection significance from 4.6 to 7.0σ possible for b=10 merely by 'massaging' a peak on the source phase density distribution into a bin boundary. Although the Pearson test is powerful in rejecting the null hypothesis the disadvantages are apparent in that the detection and significance of a positive effect vary both with the number of bins chosen and (more severely in this case) with the arbitrary choice of phase origin. With a much weaker or controversial detection around the '3σ threshold' the choice of binning or 'massaging' may be critical in accepting or rejecting a claimed observation. The Pearson test is particularly powerful in detecting this type of narrow-peaked phase density distribution.

The periodicity search conducted using the Rayleigh and the $H_{\hat{m}}$ tests is shown in Fig.7.8. As expected, the Rayleigh test performs comparatively weakly under this phase density distribution which is both narrow-peaked and bimodal.It rejects the null hypothesis $\mathcal{H}_o$ at a significance level of 4.2σ for $P_{trial} = P_o + \frac{1}{10}\Delta$. The corresponding harmonic series contains significant power away from the fundamental and application of either the Rayleigh test or Fast Fourier Transform techniques may falsely reject $\mathcal{H}_1$ in smaller sample sets. Also shown is the performance of the $H_{\hat{m}}$ test . The numbers in parenthesis refer to the optimum number of harmonics chosen from the Hart rule. The $H_{\hat{m}}$ test detects a positive effect at $P_{trial} = P_o - \frac{1}{20}\Delta$ with a significance of 6.1 σ and has none of the arbitrary choices (and corresponding variations in significance levels)

associated with the Pearson test, but performs nearly as powerfully. Note that when the Hart rule selects $\hat{m} = 1$ the power of the test is equal to the Rayleigh power, as expected. Thus for broad unimodal light curves the proposed $H_{\hat{m}}$ test will perform just as powerfully as the Rayleigh test.

The result of conducting the $H_{\hat{m}}$ periodicity search over the complete sample of events from the 1986 track of the Crab Pulsar is shown in Fig.7.9(a). The number of independent periods searched over is 100, with an oversampling factor of 1. Fig.7.9(b) shows the same period search conducted over 2 IPS with an oversampling factor of 10.

7.8 Computation of the $H_{\hat{m}}$ test

The availability of a Meiko M-10 Computing Surface hosting a number of transputers presented a unique occasion on which to transfer the periodicity searching algorithm using the $H_{\hat{m}}$ test into parallel code and run on the Computing Surface, thus making very large periodicity searches feasible on large data sets (Carstairs and Gorrod, 1989). A discussion of the efficiency of this implementation is discussed in Appendix 3.

7.9 Fourier Analysis of the Crab Data

A conventional Fourier analysis was performed on a section of the 1986 tracking scan of the Crab to demonstrate the method. Total analysed counts were extracted from the dataset using the routines described in chapter 3 and the counts data file entered into an FFT package (Davies, private communication). The result of this FFT search for the Crab fundamental frequency is shown in Fig.7.10 and it can be seen that the test fails to detect the fundamental frequency. This is due to the bimodal nature of the Crab phase density distribution and is known as a type **II** error, see section **5.2.2**.

7.10 Disadvantages of the Kernel Density Estimator technique

While the KDE technique appears to be a good alternative to the conventional histogram method there appears to be one area of doubt and that is in the choice of truncation point for

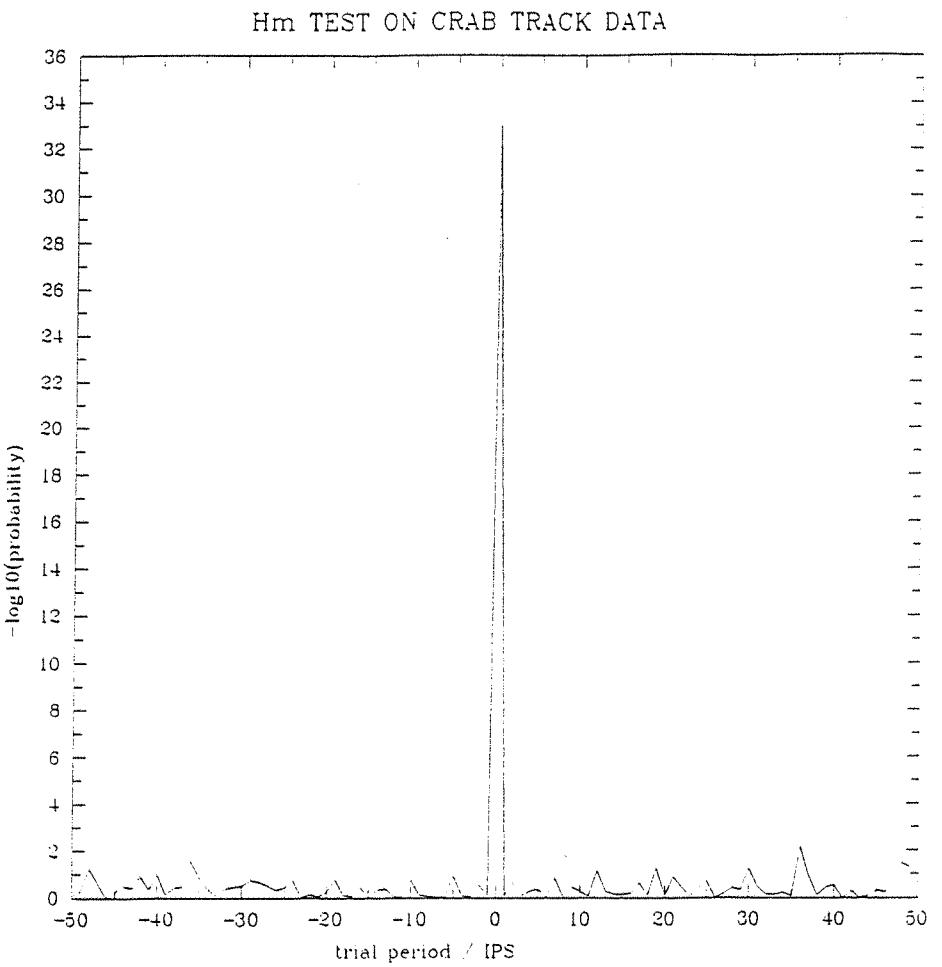

Fig7.9(a). Periodicity search using the $H_{\hat{m}}$ test on the complete 1986 tracking scan dataset. Trial period P_o corresponds to the interpolated radio period.

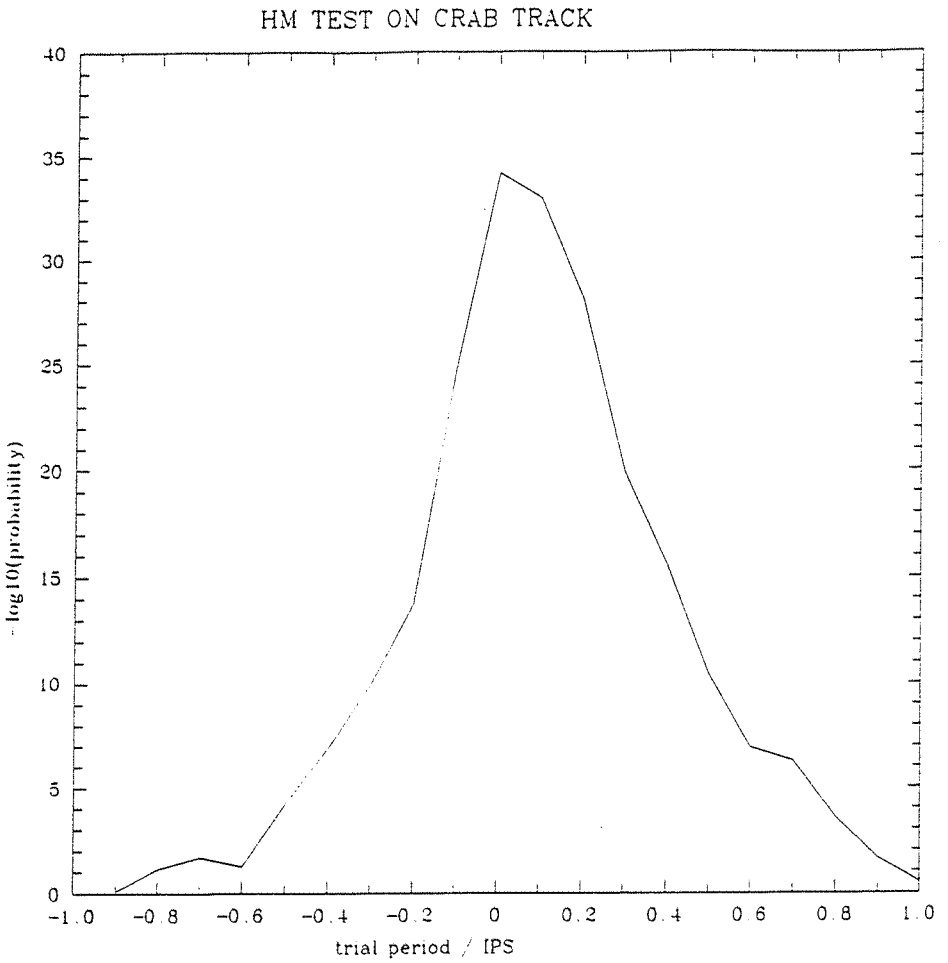

Fig7.9(b). Periodicity search using the H_m test on the complete 1986 tracking scan dataset. searching over 2 IPS with an oversampling factor of 10. Trial period P_o corresponds to the interpolated radio period.

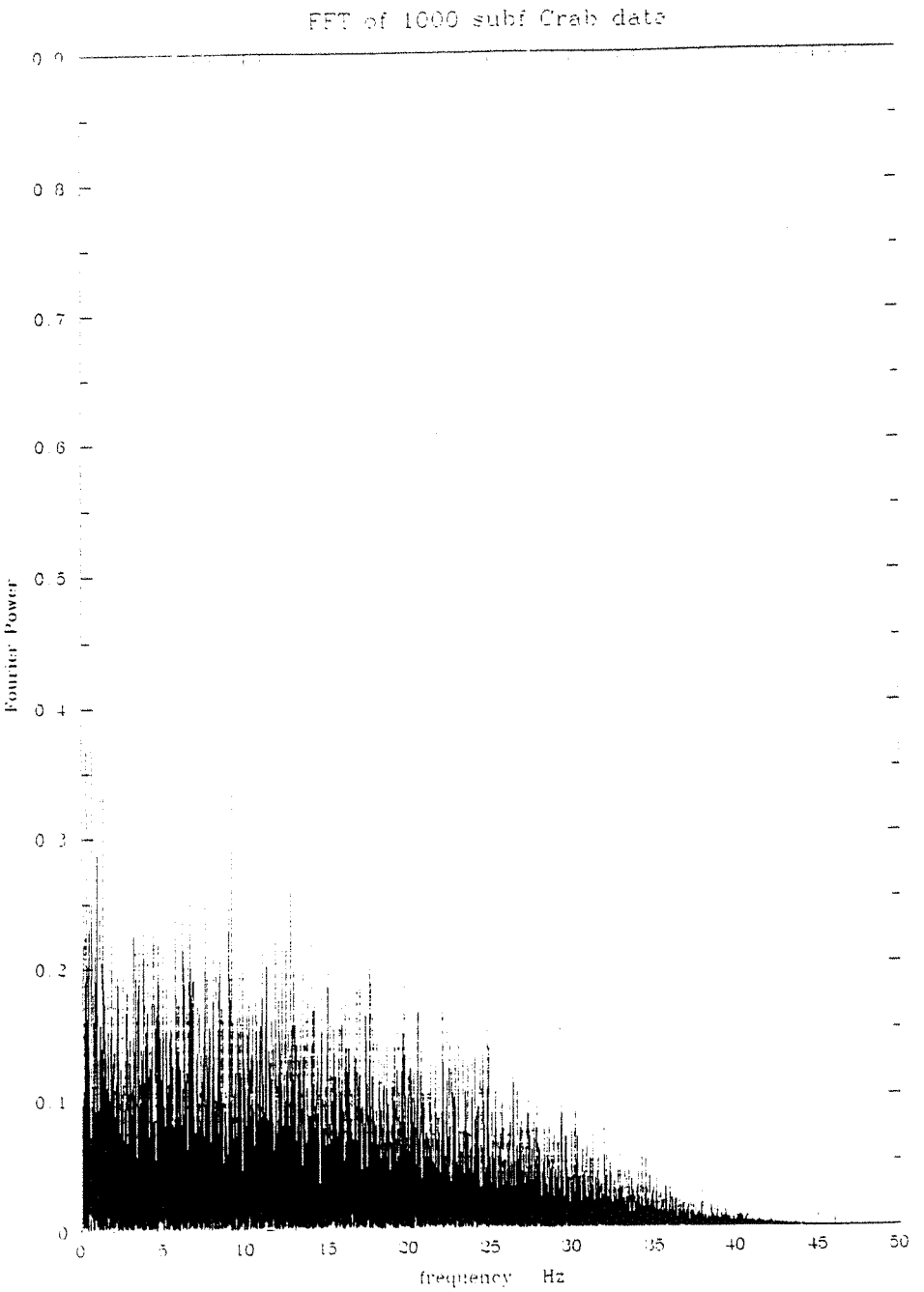

Fig.7.10. An FFT frequency search of the 1986 tracking scan Crab data, showing how the Rayleigh test fails to detect the fundamental frequency at 30 Hz, thus making a type **II** error in falsely accepting the null hypothesis.

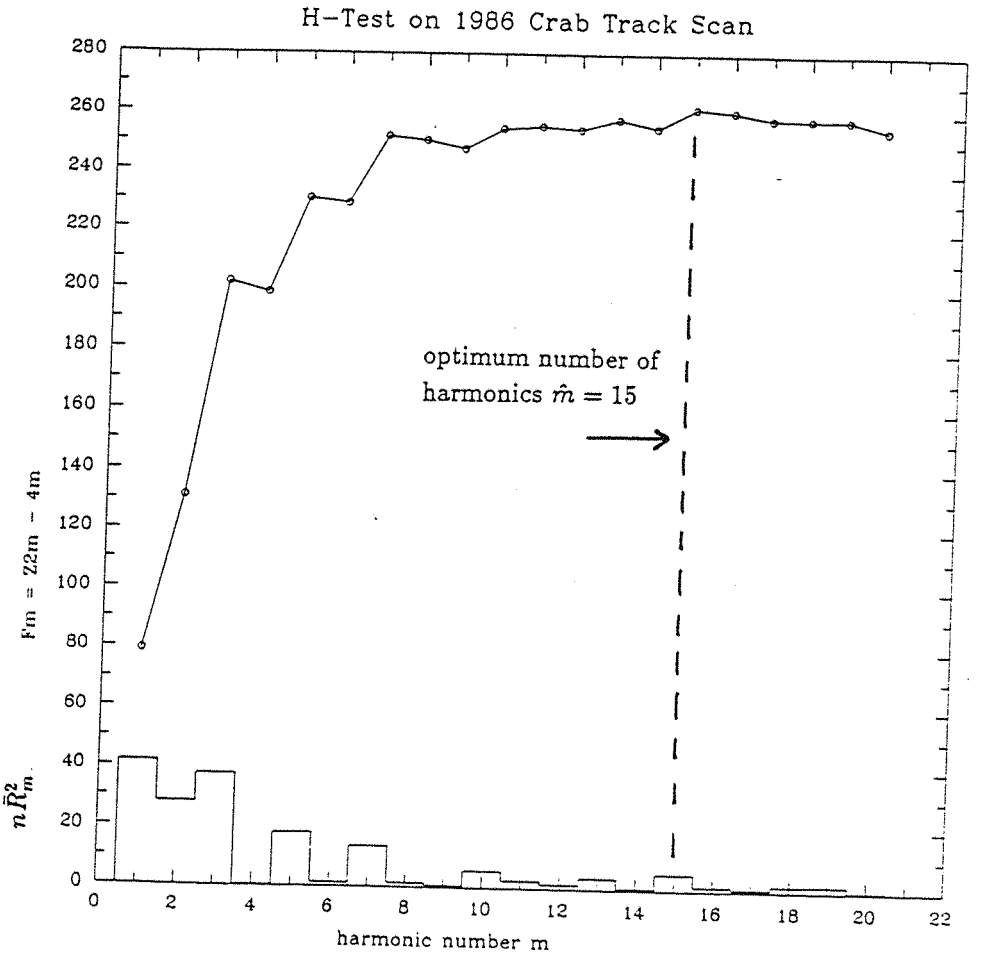

Fig.7.11. The Hart function plotted as a function of harmonic number m for the 1986 track of the Crab. Also shown is the Rayleigh power spectrum.

the harmonic series, namely, in the Hart rule. Fig.7.11 shows the Hart function plotted as a function of the number of harmonics m. The Hart rule states that the choice of truncation point with which to minimise the MISE is given by the maximum value of this function. It can be seen from Fig.7.11 that the Hart function Fm has a very poorly defined maximum at $m = 15$, in this case any choice from $m = 7$ to $m = 20$ would seem to approximate a local maximum value. It is interesting to note that in Hart's original paper a trimodal density was used as an example and a Hart function of similar form to Fig.7.11 resulted. There may be some better alternative to the Hart rule for choosing the truncation point of the harmonic series.

This chapter has concentrated on the timing analysis of the *MIFRASO* observations of the Crab Pulsar. The $H_{\hat{m}}$ test is seen to be a good alternative to the traditional Pearson and Rayleigh tests, and the kernel density technique is a good unbiased estimator of the pulsar light-curve.

Having completed the timing analysis of the Crab Pulsar using the KDE technique, and having shown that such a new technique was successful, the author applied the new test to the *MIFRASO* observation of Cygnus X-1 in order to search for pulsations from this source.

7.11 A timing analysis of the *MIFRASO* observation of Cygnus X-1

'*Any number of observations – such as the emission of pulses – could disprove a black hole.*'

- Professor Steven Hawking

The *MIFRASO* telescope observed Cygnus X-1 in a single drift scan on July 17th 1987

from 1.27 UT to 2.32 UT including background measurements. In about 900 seconds of useful on-source data, Cygnus X-1 was detected in the energy range 15-300 keV with a high degree of statistical significance. A spectral deconvolution analysis was performed on the data (Perotti, private communication), see Chapter 4. The photon spectrum is well described by either a single power law with photon index $\alpha = 1.90 \pm 0.07$ or by a Comptonized model characterised by an electron temperature of $kT_e = 55 \pm 10$ keV and an optical depth of $\tau = 2.4 \pm 0.4$. The measured flux levels suggest that during the *MIFRASO* observation Cygnus X-1 was in an intermediate condition between the so called 'low' and 'superlow' states.

The spectral deconvolutions have already been presented in Chapter 4, together with a review of the source. Conventional views of Cygnus X-1 hold that the compact object in the X-ray binary is a black hole. For example, in a rocket flight in October 1973 Rothschild et al. (1977) observed several bursts of 1ms duration with high statistical certainty. The latter measurement places the radius of the emission region at less than 10^2 km, which rules out a white dwarf as the compact object. When the compact nature of the source is combined with the mass estimates (Hutchings 1974; Avni and Bahcall 1975; Bolton 1975) and the current estimates of the upper limit of the mass of a neutron star (Rhoades and Ruffini 1974, Brecher and Caporaso 1976), the evidence suggests that Cygnus X-1 is a black hole.

Despite these considerations, the evidence that the compact object in the Cygnus X-1 binary system is a black hole is indirect at best, and the possibility exists that the compact object may be a neutron star. If this is the case, then pulsations may be observed from the rotation of the neutron star, that is, Cygnus X-1 may contain a pulsar (Pagels 1985). Because of this possibility, the *MIFRASO* observation of Cygnus X-1 was subjected to a timing analysis in the hope of discovering the pulsar.

The Cygnus X-1 observation occurred just after the groundstation for the telemetry link changed from the La Palma station to the Spanish station. Telemetry quality was very poor

with many interruptions and glitches in the data. There are two major glitches at 1.40-1.55 UT and at 1.85-2.00 UT. The latter glitch comprises the whole of the falling edge of the drift scan, so unfortunately only half of the on-source data is of sufficient quality worth analysing. Portions of the data used for spectral deconvolution were 1.32-1.44 UT, 1.55-1.87 UT and 2.00-2.30 UT (Perotti, private communication). The data were extracted from the good sections of the flight tape by inspection of the countrate and altitude profiles to assess telemetry quality. Three portions of data were used, one before the drift scan, one during the scan (the rising half) and one after the drift scan. This ensured that any signal found in the drift scan could be compared to an equal number of 'off-source' counts to be certain that any timing signal was coming from the source and not an artifact of the experiment.

The nature of the system in Cygnus X-1 - an accreting binary - immediately suggests that the pulsations (if any) will be of a broad, sinusoidal nature. Thus it is perfectly appropriate to commence the timing investigation by applying the Rayleigh test (see section 5.2.2) which is sensitive to power in the fundamental frequency. Since the search is underway for a completely unknown period, the Fast Fourier Transform was selected as the best test for the possible period (see section 5.2.3). Thus the counts per telemetry frame were extracted using the *MIFRASO* timing analysis routines and entered into an FFT package. The resultant plot of frequency against power is shown in Fig.7.12 and as can be seen there is no frequency at abnormal power in the power spectrum. Thus emission at a fundamental frequency between 0 and 30 Hz can be ruled out for a unimodal phase density distribution from the Cygnus X-1 observation.

The next step was to apply the $H_{\hat{m}}$ test to the Cygnus X-1 observation. The individual event times were barycentred using the JPL DE200/LE200 ephemerides (Standish 1982) in the manner described in section 7.2 and then extracted using the *MIFRASO* analysis routines. A file of trial periods from 1ms to 100ms in steps of 1ms was generated and the $H_{\hat{m}}$ test applied. The results are shown in Fig.7.13.

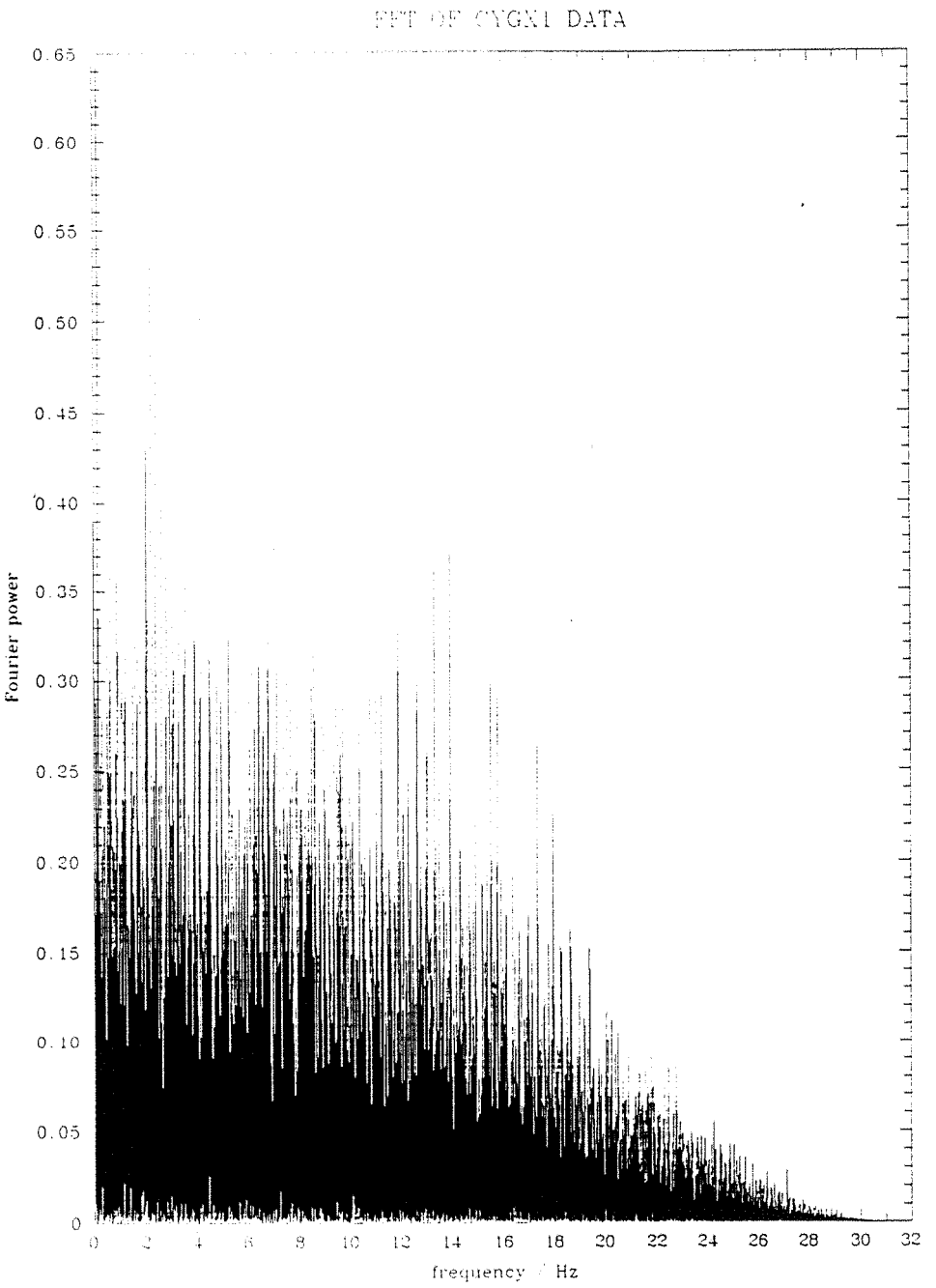

Fig.7.12. An FFT of the Cygnus X-1 data, taken from the 1987 *MIFRASO* observation.

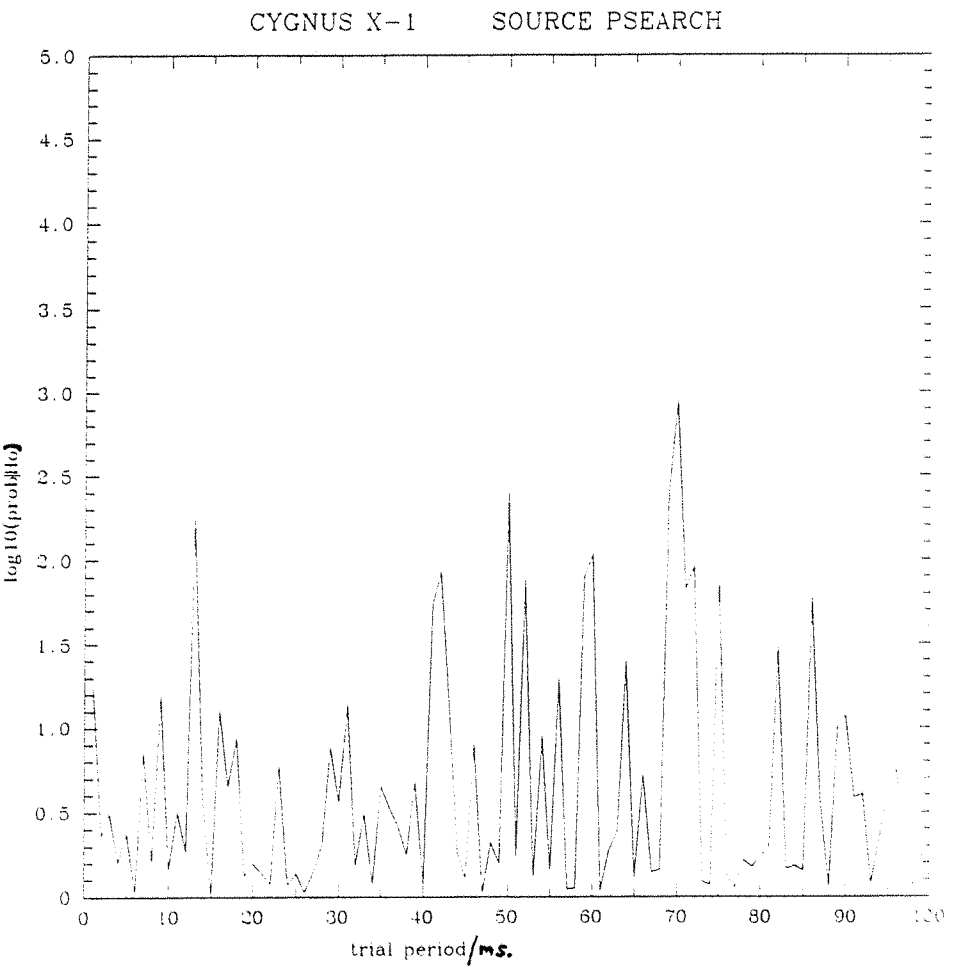

Fig.7.13. Illustrating the use of the H_m test on the Cygnus X-1 data. A period search over the range 1-100ms.

Clearly, from the very limited set of trial periods used, there is no significant periodicity present in the data. Further analysis is underway to test a larger number of trial periods, but the general conclusion from the *MIFRASO* observation of Cygnus X-1 is that there is no periodicity present within the data tested so far.

This chapter has concentrated on the timing analysis of the Crab Pulsar using the KDE technique. The next chapter concerns the spectral results of these observations. The KDE technique was used to separate the pulsed emission from the unpulsed emission, and this part of the analysis was performed by the author in collaboration with Dr.F.Perotti of the CNR, Milan, who performed the energy deconvolutions.

CHAPTER 8 :*MIFRASO* OBSERVATIONS OF THE CRAB PULSAR : SPECTRAL ANALYSIS

8.1 Introduction

In addition to the timing analysis of the Crab Pulsar described in this work so far there is a second important component to be included any study of the Crab, namely the energy spectrum originating from this object. The Crab spectrum has been studied by many telescopes and is now a 'laboratory standard' for observation programmes. The spectral characteristics of the Crab still contain one mystery : that of a transient cyclotron line feature that has been seen by some groups and not by others. It is the search for cyclotron emission that helped motivate the spectral observation of the Crab described in this chapter.

8.2 Time averaged energy spectrum of the Crab

The Crab was tracked between 8^h42^m and 8^h55^m UT for the 1986 observation. In order to minimise possible background variations related to changes in elevation and/or azimuth, the background hard X-ray flux was evaluated between 8^h29^m and 8^h42^m tracking a point of the sky having the same declination of the Crab but having a right ascension 4^o lower . This ensured that the same sequence of steering maneuvers was used during both source and background measurements.

The accuracy of the steering system was tested by scanning a region of sky centred on a declination of 22^o contained within right ascensions of 05^h11^m and 05^h56^m. The transit of the Crab through the *MIFRASO* field of view in about 1300 seconds produced a well defined triangular profile when the counting rate was plotted verses the angular distance between the axis of the telescope and the estimated direction of the source. From this profile an offset of about 0.5^o in the steering azimuth was detected. Consequently, for the 1986 flight the effective

detection area was reduced by 20% for all observations performed in the tracking mode. The data for the tracking and drift scans of the Crab were analysed separately and the results statistically combined . The only source of systematic variation in the background hard X-ray flux was found to be linearly related to the changes of the residual atmospheric pressure, which varied between 3.8 and 4.0 mbar. The energy response of the detectors was found to be stable to within $\pm 0.5\%$.

When the Crab was in the field of view of the telescope a mean increase in the HED detector counting rate of 41%, 25%, 5% and 1.3% was detected in the energy bands 20-45 keV, 45-100 keV, 100-180 keV and 180-300 keV respectively. The mean increase in the LED detector was 20%, 14% and 1.5% in the energy bands 15-30 keV, 30-60 keV and 60-120 keV respectively.

The time averaged photon spectrum of the Crab was computed under the assumption of a single power law emission from the source and taking into account the atmospheric interactions along the line of sight (mean value 4.3 gcm^{-2}), as well as the response function of the detectors. Fig.8.1 shows the mean photon spectrum for the two observations combined. The spectra relative to the individual observations differ by less than 3% over the full energy range. Fig.8.2 shows a goodness-of-fit plot of the total observations.

The best fit power law spectrum derived for the overall detector (LED + HED) is

$$\frac{dI}{dE_x} = (1.42 \pm 0.02) \times 10^{-3} (E_x/60)^{-(2.14 \pm 0.06)} \text{ photons cm}^{-2} \text{ s}^{-1} \text{ keV}^{-1}$$

with a reduced χ^2 value of 0.7 for 28 degrees of freedom. The errors given are at the 90% confidence level for the joint variation of the two parameters (Avni 1976).

The total spectrum of the Crab is in very good agreement with other high quality results obtained previously (Dolan et al. 1977, Strickman et al. 1979, Manchanda et al., 1982). The spectrum has been tested for the presence of a narrow line at 73.3 keV as reported by some observers (Jacobson et al. 1978, Ling et al. 1979, Manchanda et al., 1982). Evidence for the existence of such a spectral feature has not been found. A 95% confidence upper limit to the

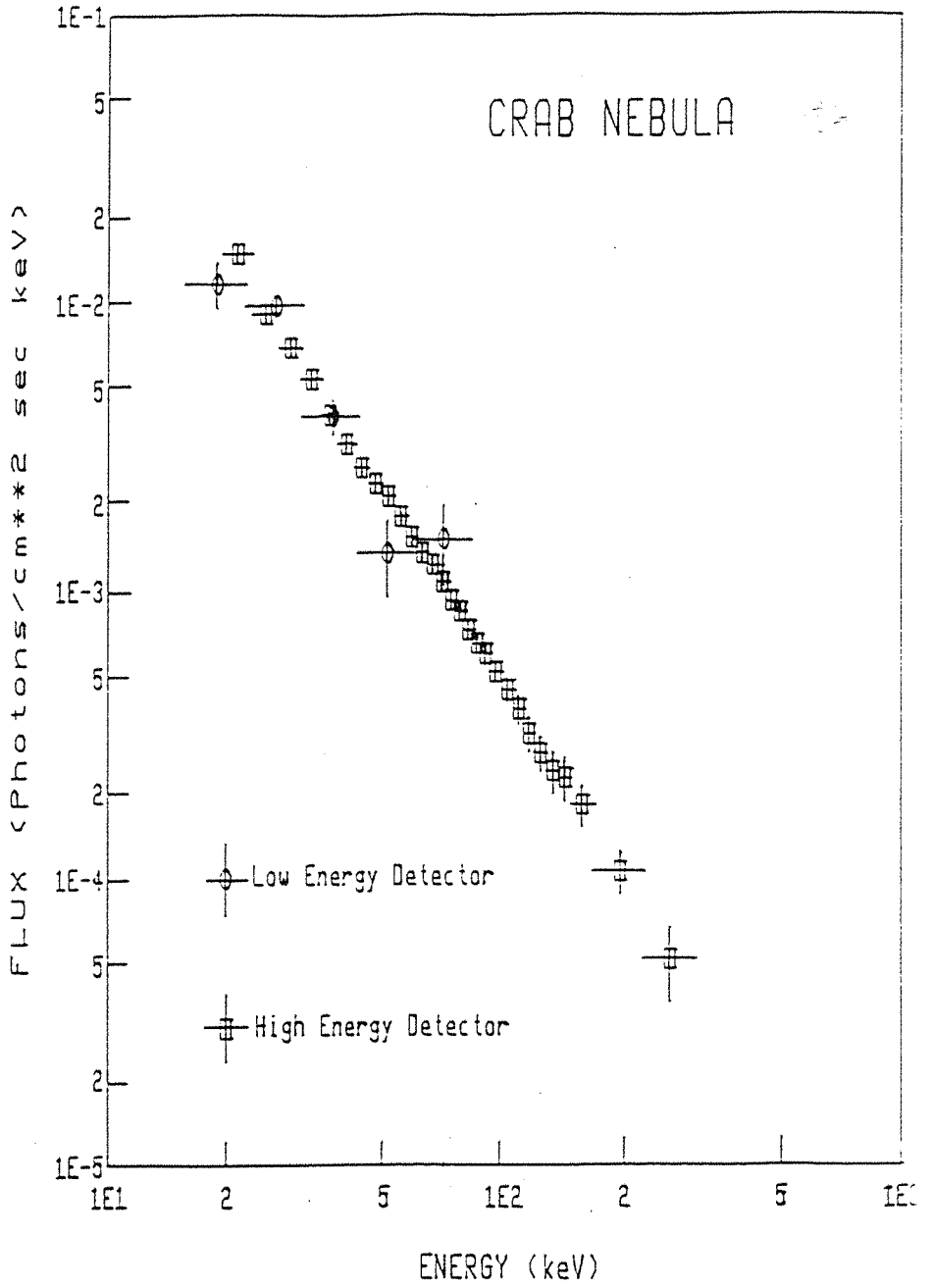

Fig.8.1. The time averaged photon spectrum for the Crab observations from 1986 and 1987.

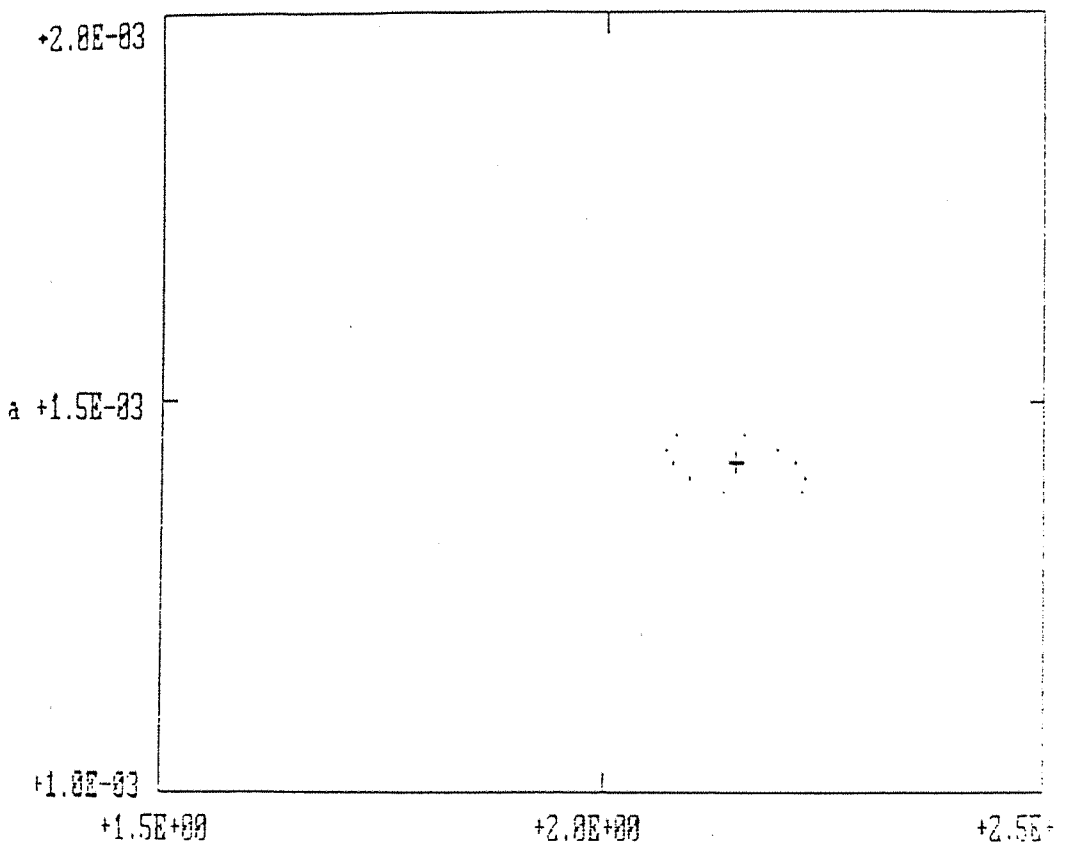

Fig.8.2. A goodness-of-fit plot for the *MIFRASO* observations of the Crab.

line intensity of 1.8×10^{-3} photons cm^{-2} s^{-1} was derived, significantly below the reported flux value of $3 - 5 \times 10^{-3}$ photons cm^{-2} s^{-1} (see section **8.4**).

8.3 Pulse Phase resolved energy spectrum

In order to separately deconvolve the pulsed emission from the Crab pulsar, phase boundaries have to be assigned to the various components of the profile. The pulsed emission has been defined as all those events within relative phase 0.2 to 0.8. With this definition, the Crab events from the 1986 tracking scan were separated into pulsed and non- pulsed emission and the pulsed excess countrate found from

$$x = \frac{p}{0.6 \times \tau} - \frac{up}{0.4 \times \tau} \tag{1}$$

where x is the pulsed excess countrate (counts/second), p is the total pulsed counts, up is the total unpulsed counts and τ is the total integration time for the observation.

The standard error squared on x is then

$$\sigma^2 = \frac{p}{(0.6 \times \tau)^2} + \frac{up}{(0.6 \times \tau)^2} \tag{2}$$

With knowledge of x and σ for each PHA bin, the pulsed flux can be deconvolved (Perotti, private communication). A power-law was found to fit the pulsed deconvolved emission of the form

$$\frac{dI}{dE_x} = (3.47 \pm 0.34) \times 10^{-4} \times (E/E_o)^{1.83 \pm 0.28} \text{ photons cm}^{-2} \text{ s}^{-1} \text{ keV}^{-1}$$

in good agreement with other reported observations (eg. Knight, 1982). For the 1987 drift scan of the Crab region, the pulsed flux was again found to have a power-law spectral fit of the form

$$\frac{dI}{dE_x} = (4.75 \pm 0.50) \times 10^{-4} \times E/E_o{}^{1.80\pm0.30} \text{ photons cm}^{-2} \text{ s}^{-1} \text{ keV}^{-1}$$

with E_o=60 keV. The power law fit model gave a reduced χ^2 of 0.54 for 12 degrees of freedom. Errors are given at the 1 σ confidence level for the joint variation of the free parameters. The mean exposed area for the drift scan was calculated as 1134 cm^2 and the mean atmospheric depth was taken as 4.33 gcm^{-2}.

No line feature was detected in the pulsed flux for either of the observations.

8.4 Detection of cyclotron lines from the Crab

There are several reports of a line feature both in the time averaged and pulsed energy spectra from the Crab. Line emission at (73.3± 1.0) keV was detected during a balloon flight on June 10, 1974 with a shielded germanium detector gamma-ray spectrometer (Ling et al, 1979). The line had an intensity of $(3.8\pm0.9) \times 10^{-3}$ photons cm^{-2} s^{-1} and a width of <4.9 keV FWHM. It was unpulsed with a limit of 25% (1σ) on the pulsed fraction.

Using data obtained during a subsequent balloon flight on May 11 1976 with a NaI detector experiment, no line feature near 73 keV from either the Crab nebula or its pulsar was reported (Strickman et al., 1979). However, further analysis indicated flaring line emission from the pulsar at (76.6 ± 2.5) keV (Strickman et al, 1982). This feature was detected only during the first 25 minutes of a 3 hour observation with a phase averaged intensity of $(3.0 \pm0.9) \times 10^{-3}$ photons cm^{-2} s^{-1} and a line width of (8 ±18) keV FWHM. A second apparent confirmation of the line emission was reported from observations made with a multiwire, high pressure xenon, proportional counter (Manchanda et al., 1982). These investigators reported an unpulsed line

feature near 73 keV with an intensity of $(5 \pm 1.5) \times 10^{-3}$ photons cm^{-2} s^{-1}.

On the other hand, there have been several observations of the Crab during which no line emission near 73 keV was detected. During a balloon flight on October 17-18 1979 an observation of the Crab was made with an array of planar germanium detectors (Schwartz et al., 1980). They saw no evidence for line radiation in the energy range of 30-200 keV and were able to place a 3σ limit of 2×10^{-3} photons cm^{-2} s^{-1} on any feature near 73 keV. An observation of the Crab was made with a balloon-borne germanium detector array on September 25 1980 (Hameury et al., 1983) and also failed to detect line emission near 73 keV. They reported a 3σ upper limit of 6.2×10^{-4} photons cm^{-2} s^{-1} on unpulsed emission. While they quoted no limits, there is no evidence for line emission in the published gamma-ray spectrum of the pulsar. Gamma-ray spectra of the Crab pulsar obtained with HEAO 1 on March 24-25 1978 and September 29 1978 (Knight, 1982) show no evidence for a line feature near 73 keV. A 3σ limit on the phase averaged emission of about 1.0×10^{-3} photons cm^{-2} s^{-1} has been obtained from these observations. Finally, an observation of the Crab pulsar made on September 28-29 1981 with a balloon-borne scintillation detector (Hasinger et al., 1982) deduced a 2σ upper limit on narrow line emission near 77 keV of 1.9×10^{-3} photons cm^{-2} s^{-1}. To these negative sightings must now be added the *MIFRASO* observations. There is also equally confused evidence for a narrow line feature at 400 keV.

The importance of cyclotron line emission from the Crab pulsar lies in the fact that line emission imposes certain restrictions on the possible beaming mechanisms for the pulsar (Meszaros, 1978). In the superstrong magnetic fields of neutron stars electrons can move freely only along the magnetic field lines while their transverse energies are quantised in units of the cyclotron frequency

$$E_n = n\hbar\omega_B = n\hbar\frac{eB}{m_e c} = 11.6 \text{ keV } B_{12}.$$

This is a nonrelativistic expression. The relativistic quantum mechanical treatment leads to eigenvalue solutions of the Dirac equation (Trumper, 1984).

If the temperature in the hot radiating plasma at the neutron star pole is high enough, excitation of the lower Landau levels may occur and the corresponding Landau transitions may give rise to discrete spectral features (Gnedin and Sunyaev, 1974). In addition, the Thomson scattering cross section as well as free-free emission and absorption processes become resonant at the cyclotron resonance frequencies , at least for the extraordinary photons.

There are several consequences of cyclotron emission. Presuming a gravitational redshift z=0.2, the magnetic field required to produce a 77 keV cyclotron line is 8 $\times 10^{12}$ gauss for electrons at rest. Such a high field is only expected very close to the neutron star surface. Furthermore, if the line emission occurs in the electron acceleration region, any acceleration mechanisms near the surface, for example, a surface spark gap (Ruderman and Sutherland, 1975) must be turned off at least temporarily for the electrons to be at rest (Harding, 1981). However, most of the electrons in a pulsar magnetosphere may be streaming along the magnetic field lines at relativistic velocities. Assuming a surface field of 10^{12} gauss and a strictly dipolar configuration of the field lines, this places the line emission at a radius of about 5×10^6 cm. This is still very close to the neutron star surface.

Two major requirements present themselves with respect to the cyclotron emission model. First, any detailed model must produce a pulsed, variable-intensity feature at 77 keV without causing the intensity of the pulsed continuum to vary. This requirement suggests that different electrons, or the same electrons in different regions of the magnetosphere, produce the continuum and the line feature. Furthermore, any cyclotron mechanism requires continual injection of energy into the electron excitation process, since electrons in excited cyclotron states radiate on time scales much less than 25 minutes.

Second, the line is observed to be relatively narrow. This implies a constraint on the

temperature of the emitting electrons, presuming they are thermal. A 95% upper limit to kT is 37 keV from thermal Doppler broadening. This upper limit applies to the line emission region only, it does not apply to the entire neutron star surface. In addition, a narrow line implies a small range of magnetic field strengths, implying a small volume of space.

8.5 Energy Resolved Pulse Profiles

For each of the three observations of the Crab region the datasets were split into three energy bands : 23-50 keV, 50-90 keV and 90-242 keV. These ranges were chosen so that an approximate equal number of events were captured in each. A KDE of the pulse profile was made of each energy range from each observation and the sets of each energy range combined using the weighted mean technique as described in Chapter 7.

Fig.8.3(a)-(c) shows the three pulse profiles resulting from this analysis. The general trend is for a decrease in amplitude of the pulses, as would be expected from the energy response of the detectors. The secondary pulse still dominates the profile, even down to the 90-242 keV profile (Fig.8.3(c)). There is substantial filling in of the interpulse region moving from low energy to high energy. Most interestingly, however, is the possible evidence for a sub-pulse in the energy region 25-50 keV at relative phase 0.1. The sub-pulse continues to be evident at higher energies. All three observations of the sub-pulse are at a significance level below the 3σ confidence threshold, however. It was noticed in one of the data cuts, the 50-90 keV pulse profile of the 1986 drift scan, that the sub-pulse at relative phase 0.9 appeared at a significance level greater than 3σ, thus providing confidence that the *MIFRASO* observations of the Crab provide tentative evidence for the detection of a sub-pulse from the pulsar. The pulse profile in question is illustrated in Fig.8.4. Possible explanations for the sub-pulse include the substructure representing instantaneous clumps of plasma in the pulsar magnetosphere (Buccheri et al., 1988). Alternatively, the appearance of a third weak pulse may represent another outer gap just entering

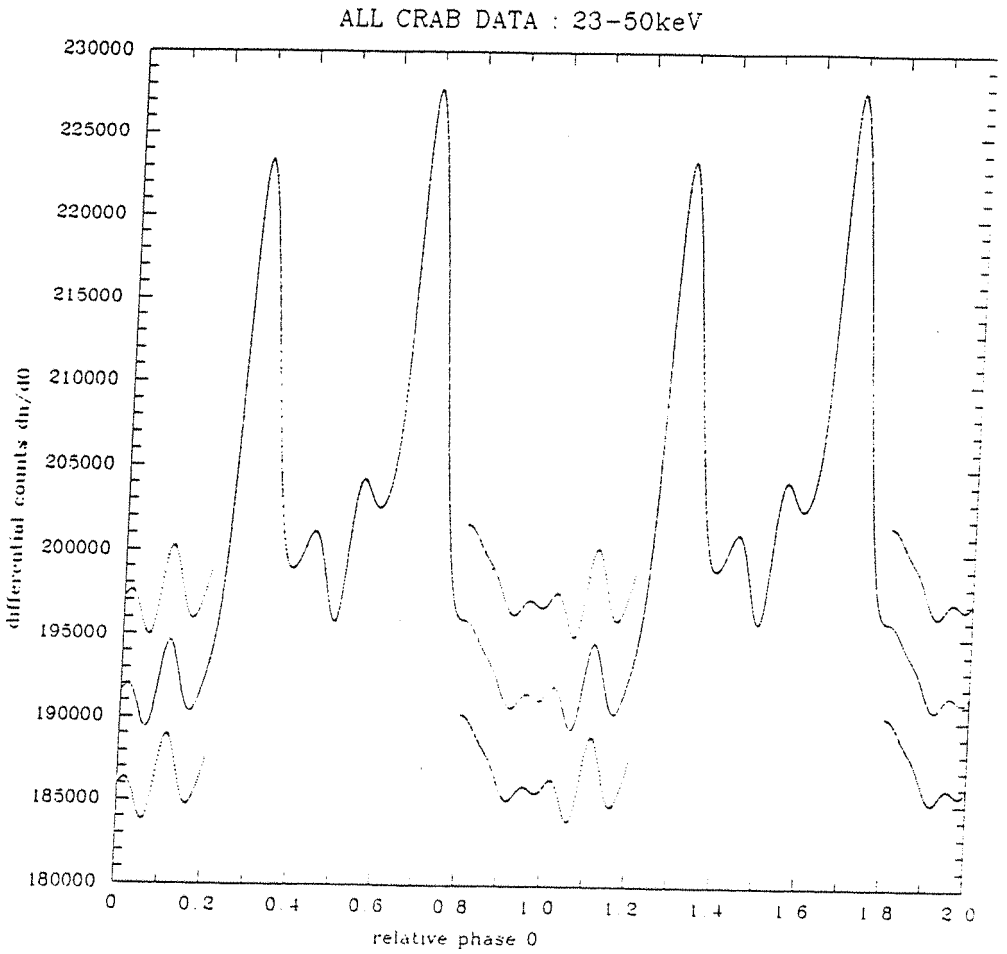

Fig.8.3.(a). The kernel density estimate of the 23-50 keV pulse profile of the Crab pulsar, summed from the three *MIFRASO* observations. The dotted confidence band is $\pm 3\sigma$ around the unpulsed emission.

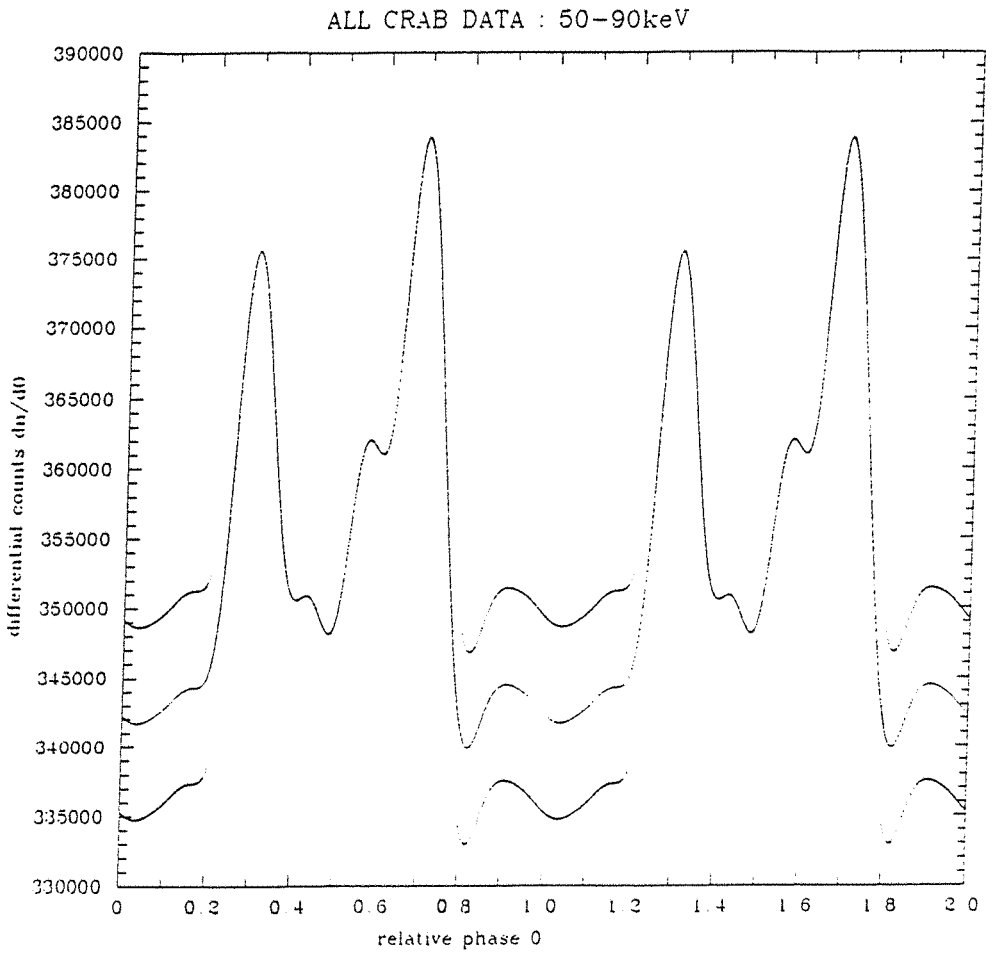

Fig.8.3.(b). The kernel density estimate of the 50-90 keV pulse profile of the Crab pulsar, summed from the three *MIFRASO* observations. The dotted confidence band is $\pm 3\sigma$ around the unpulsed emission.

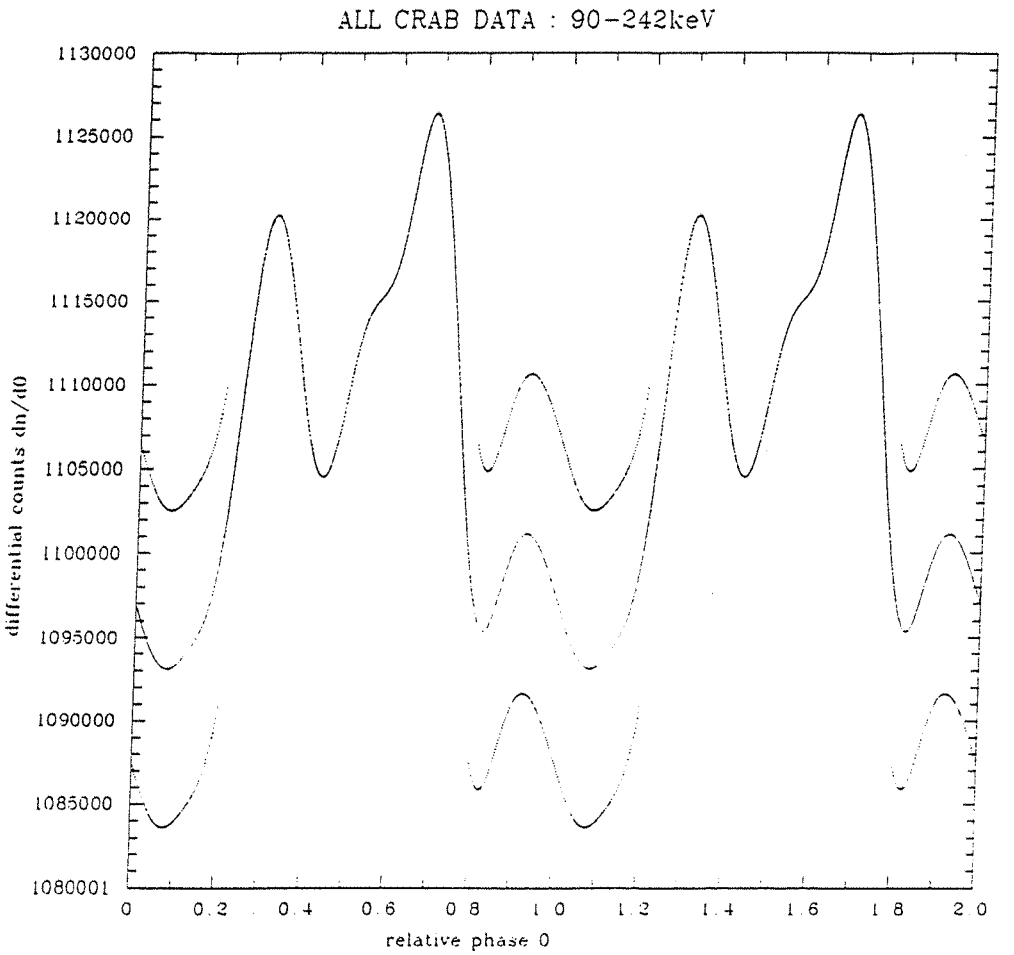

Fig.8.3.(c). The kernel density estimate of the 90-242 keV pulse profile of the Crab pulsar, summed from the three *MIFRASO* observations. The dotted confidence band is $\pm 3\sigma$ around the unpulsed emission.

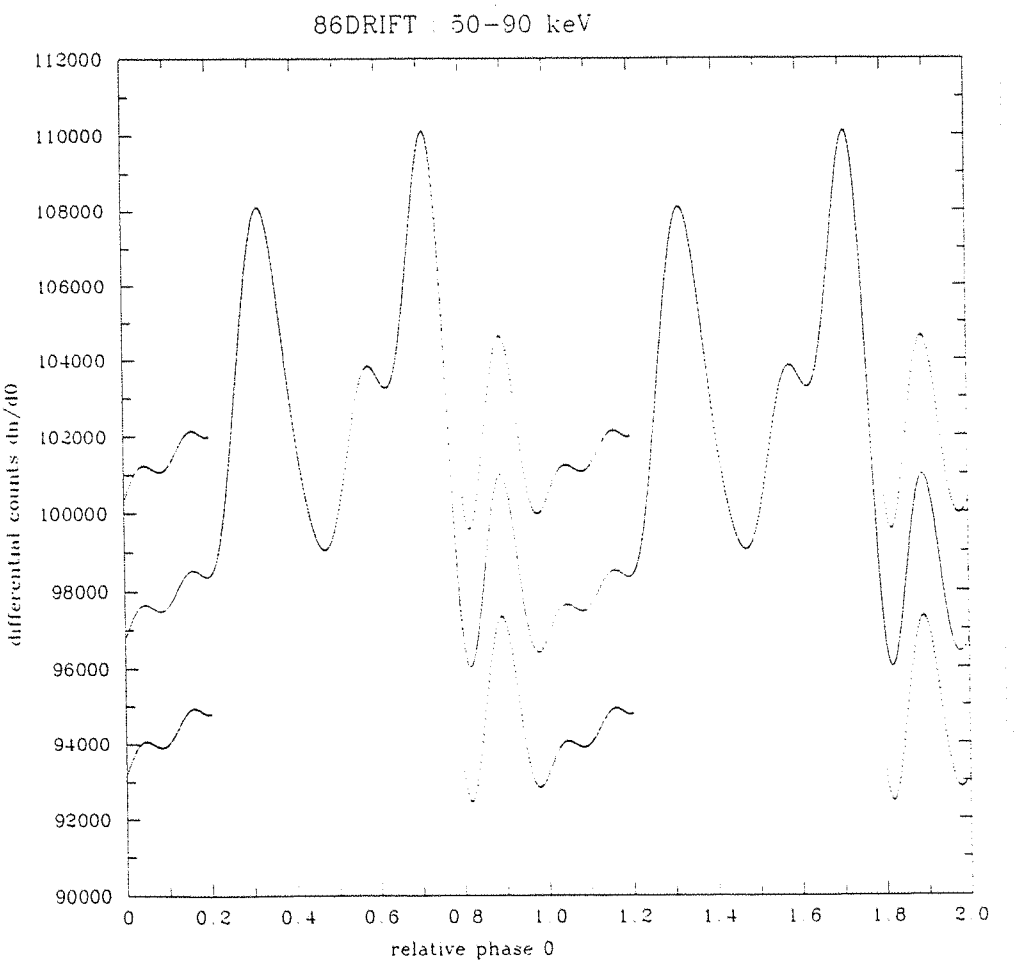

Fig.8.4. The 50-90 keV pulse profile from the 1986 drift scan observation showing the possible evidence of a subpulse at relative phase 0.9.

the line of sight (Cheng, Ho and Ruderman 1986b). The outer gaps are thought to be the site of the high energy emission (see Chapter 9). However, in this case one would expect a pair of sub-pulses, separated by a phase of 0.4 which seems to be related to the geometry of the emission regions, such as the location and origin of the outer gaps. Two such features were seen in the low-energy gamma-ray experiment *FIGARO II* observing in the energy range 0.2-6.0 MeV (Agrinier et al., 1990) at absolute phase 0.2 and 0.6, corresponding to the *MIFRASO* relative phases 0.5 and 0.1 respectively. In the *FIGARO II* experiment the residual phases were binned in a 60-bin histogram, thus bringing up the problems of varience and bias discussed in Chapter 5. (Agrinier et al., 1990). It would be most instructive to apply the KDE technique to the *FIGARO II* results and to estimate the significance of the subpulses using CDE (see Appendix 2).

This chapter has discussed the spectral results of the *MIFRASO* observations of the Crab Pulsar. The time-averaged energy spectrum is seen to be in good agreement with other high-quality measurements of the source. Separating the pulsed flux from the unpulsed flux leads to a harder spectral index for the pulsed flux, again in agreement with previous results. Forming the energy resolved pulse profiles leads to the possible identification of a sub-pulse.

The following chapter reviews the latest theories on the emission regions in the magnetosphere surrounding the pulsar, the very regions that are ultimately responsible for the pulsed and unpulsed emission as observed by the *MIFRASO* telescope.

CHAPTER 9 : ELECTRODYNAMICS OF THE CRAB PULSAR

9.1 Introduction

The final chapter of this work is a review of the theories describing the energetics of the Crab Pulsar, that is, theories describing its electromagnetic properties and emission of radiation. There are many such theories in evidence, some treat the Crab Pulsar as a purely classical phenomena (Mestel, private communication) while others, reviewed here, offer a relativistic treatment (Cheng, private communication). Any such theory has to account for the spectrum of the emission as well as the pulsations seen from radio through to the highest energy gamma rays.

9.2 Neutron Stars

The concept of a neutron star - an object consisting primarily of neutrons, with a mass about equal to that of the sun but with a radius of only about 10km - was first discussed by Baade and Zwicky in 1934. Model calculations giving the structure of the object were first made soon after (Oppenheimer and Volkoff, 1939). These authors considered a model in which the star is composed of noninteracting neutrons. At the enormous densities encountered in the interior of such stars, about 10^{14} gcm^{-3}, the neutrons form a degenerate Fermi gas; the pressure associated with this degeneracy is sufficiently large to prevent further collapse of the star. Further analyses have considered more realistic compositions and equations of state for the various density regions.

In the outermost regions the structure of a neutron star is expected to be the same as in the interior of white dwarf stars : ^{56}Fe nuclei surrounded by a sea of degenerate electrons and a density at the surface of about 10^4 gcm^{-3}. The iron nuclei, because of their mutual electrostatic repulsion, are expected to form a body-centered crystalline lattice, thereby giving the neutron

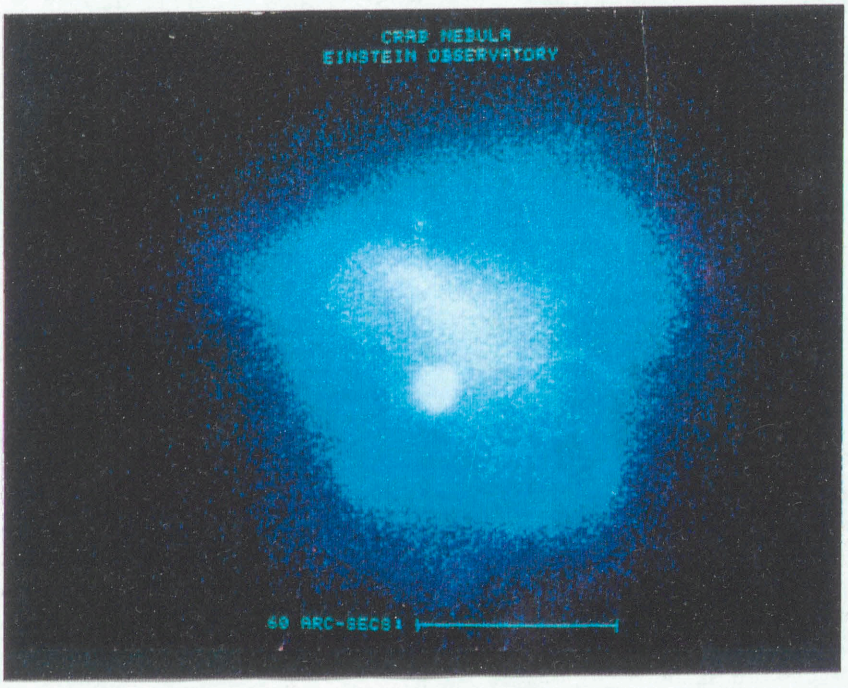

Plate 9.1. A X-ray image of the Crab taken with NASA's HEAO-2 satellite observatory showing the central pulsar surrounded by the active nebula.

star a solid outer crust. The Coulomb interaction energy is very high (about 1 MeV per nucleus), so this crust will have a large shear modulus and hence be very rigid. During the spin-down of neutron stars such as the one forming the Crab pulsar, strong stresses and strains develop in the stellar crust (Ruderman, 1991a). The stresses are caused by crystal lattice pinning of neutron superfluid vortices (Ruderman 1976), possibly reinforced by the pull on the crust of the superconducting core's magnetic flux tubes. When these growing vortex pinning stresses in the cool, spinning-down neutron star strain the crust beyond its elastic yield strength, large-scale crust cracking events may occur (Ruderman 1991b). These would result in pulsar timing glitches with magnitude and recurrence rates near those observed. Well-defined timing glitches were seen in the Crab pulsar in 1969 (Boynton et al., 1972) , 1975 (Gullahorn et al., 1977) and in 1986 (Lyne et al., 1988). The progress of this last glitch was monitored in unprecedented detail; it appears that it occurred one hour before observations began (Lyne and Pritchard 1987).

Beneath the outer crust of iron nuclei the density increases , resulting in electron capture by the nuclei. This layer consists of neutron-rich nuclei, forming another crystalline lattice known as the inner crust and surrounded by a sea of degenerate electrons. Within this inner crust the interaction between two neutrons is sufficiently attractive for the neutrons to form a superfluid.

In the next section, at distances of about 11km radius from the core, the material is thought to form a uniform sea of electrons, protons and neutrons, with all but a few percent of matter in the form of neutrons. The density here is greater than about 2×10^{14} gcm^{-3}. The properties of matter at these super-nuclear densities are still the subject of much investigation, but it is expected that in this region the neutrons will again be superfluid and that the protons will be superconducting. There may be a zone of normal neutrons between the crustal and interior superfluid regions; the behaviour of electrons remains normal throughout the star.

Fig.9.1. shows the inner structure of a 1 solar mass neutron star.

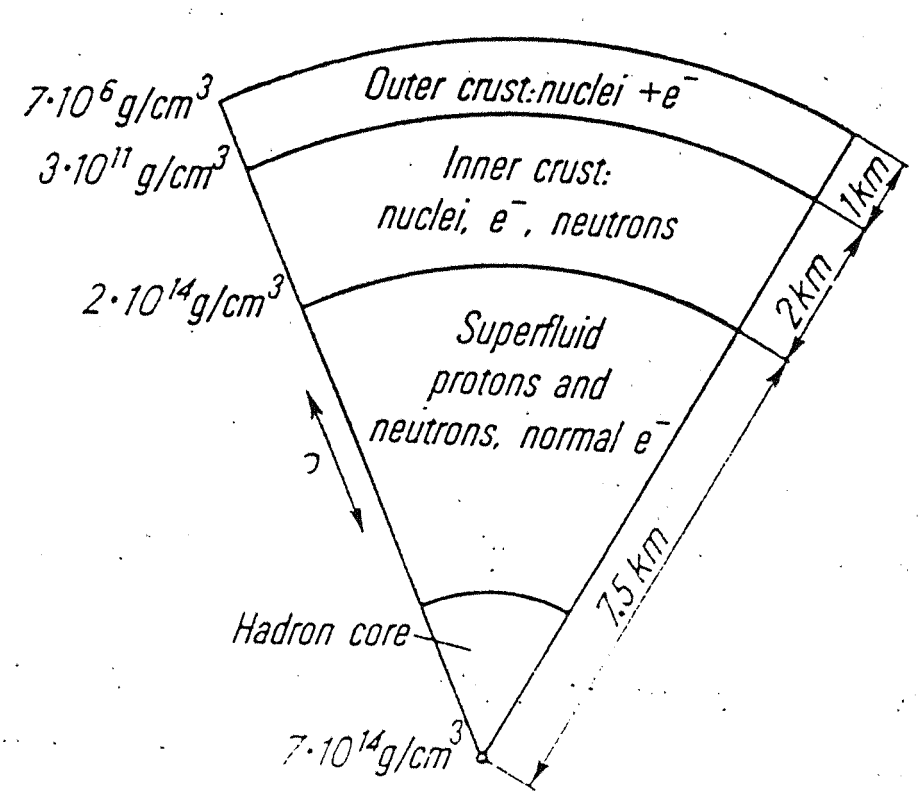

Fig.9.1. The internal structure of a 1 solar mass neutron star. From Demianski,1985.

9.3 Proof of existence of the Magnetosphere

Consider a neutron star which, if nonrotating, would have an external dipolar magnetic field which is continuous at the stellar surface (Goldreich and Julian 1969). Suppose the star is rotating about the dipole axis with angular velocity Ω and period $P = 2\pi/\Omega$. Assuming that the stellar matter in both the degenerate interior and the nondegenerate atmosphere is an excellent electrical conductor, the star will be polarised so as to possess an interior electric field that satisfies

$$\mathbf{E} + \frac{\mathbf{\Omega} \times r}{c} \times \mathbf{B} = 0 \tag{1}$$

If the star is surrounded by a vacuum then Laplace's equation for the external potential can be solved. The resulting potential would be

$$\Phi = \frac{-B_o \Omega R^5}{3cr^3} P_2(\cos\theta) \tag{2}$$

with B_o the polar magnetic field. The surface charge density on the star, as computed from the discontinuity of the normal component of the electric field at its surface, would then be

$$\sigma = \frac{-B_o \Omega R}{4\pi c} \cos^2\theta. \tag{3}$$

The Lorentz invarient **E.B** vanishes in the stellar interior. In the case where the star is surrounded by a vacuum, the external value of **E.B**, assuming a dipolar field, would be given by

$$\mathbf{E}.\mathbf{B} = -\frac{\Omega R}{c}(\frac{R}{r})^7 B_o^2 \cos^3\theta. \tag{4}$$

Within the surface charge layer the value of **E.B** must change continuously from zero to its external value.Thus, near the outer edge of the charge layer the magnitude of the electric force along the direction of the magnetic field would exceed the component of the gravitational force in the same direction. Clearly, the surface charge layer could not be in dynamical equilibrium. From this contradiction, it is concluded that a rotating magnetic neutron star cannot be surrounded by a vacuum. Charged particles are stripped from the stellar surface to form a dense magnetosphere.

9.4 Structure of the Magnetosphere

Consider a neutron star which is the remnant of a supernova. Assume that the supernova outburst gave rise to an expanding shell which has swept up all the interstellar material out to a distance D. Three separate zones may be distinguished in a general description of the particles and fields surrounding the neutron star. The *near zone* is contained within the light cylinder ($r\sin\theta = c/\Omega$) and is bounded in the z direction by planes at $z \pm c/\Omega$. The *wind zone* encloses the near zone out to $D/10$ where it merges into the *boundary zone*. The boundary zone stretches out to the *supernova shell* at distance D from the neutron star. These zones are illustrated in Fig.9.2(a) and (b).

In both the near and wind zones the magnetic-energy density greatly exceeds the particle kinetic-energy. In addition, the magnetic- field lines are very nearly electric equipotentials in these two zones. Thus charge-particle motion may be thought of as sliding along magnetic-field lines which rotate rigidly with the star's angular velocity. The poloidal magnetic field is shown in Fig.9.2(a). The particles which are attached to the closed magnetic-field lines corotate with the neutron star and comprise the corotating magnetosphere.The magnetic-field lines

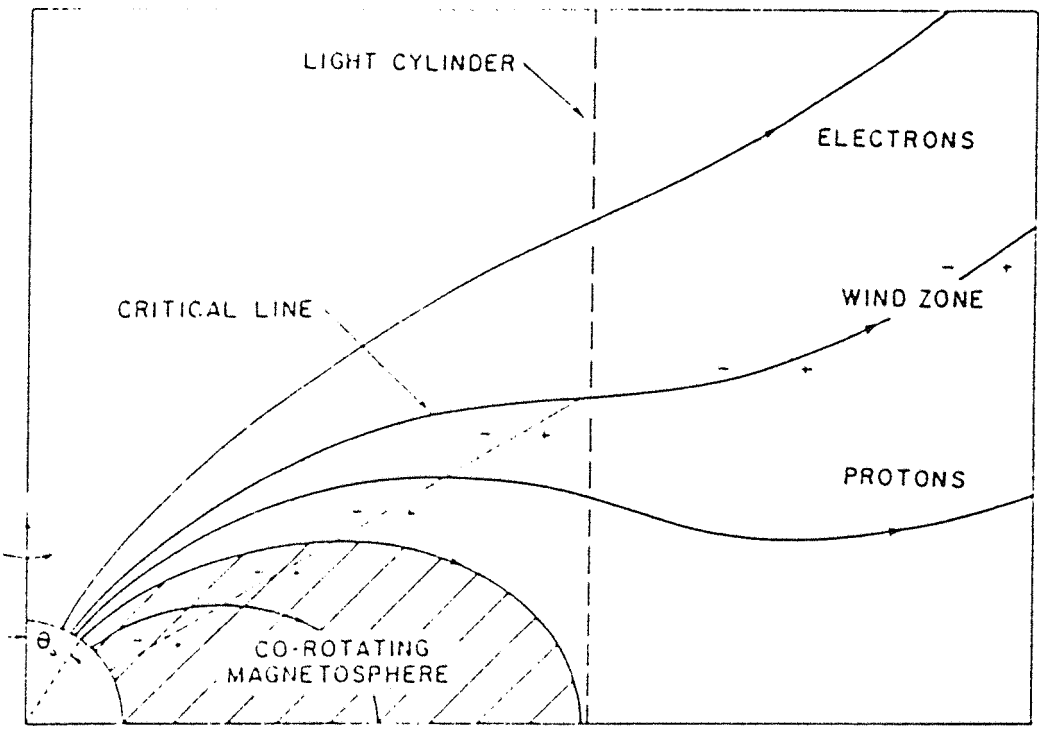

Fig.9.2(a).The corotating magnetosphere and the wind zone of a hypothetical pulsar. From Goldreich and Julian, 1969.

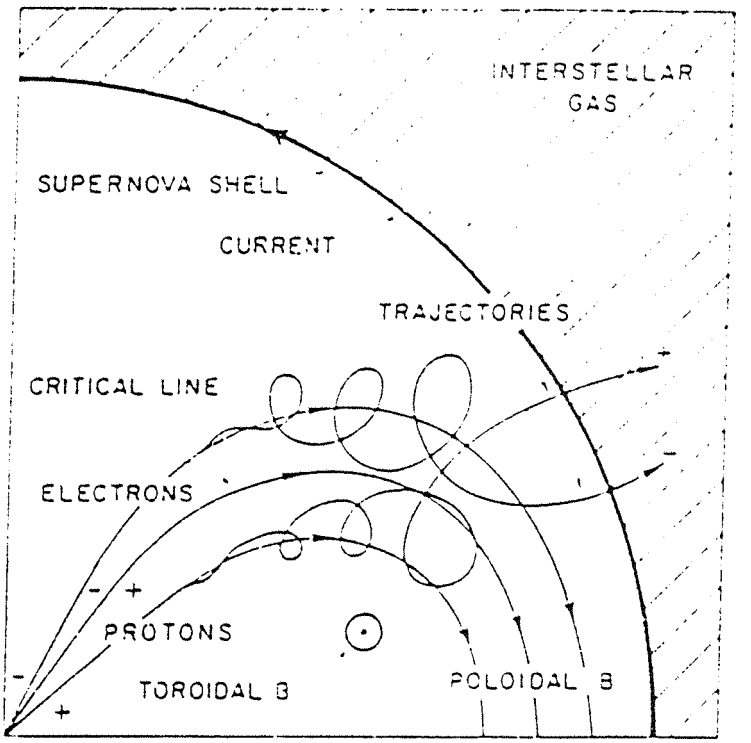

Fig.9.2(b). The supernova cavity, shell and interstellar gas surrounding the pulsar. From Goldreich and Julian, 1969.

which pass through the light cylinder are open (they close in the boundary layer) , and charged particles stream out along them. The feet of the *critical* magnetic-field lines are at the same electric potential as the interstellar medium. Electrons stream out along higher-latitude lines (*electron lines*) whereas protons escape along the lower-latitude open lines (*proton lines*) . In this model, the electric potential is highest at the equator of the stellar surface and decreases towards the poles.

It is assumed that the current distribution in the star would, by itself, produce a rotationally symmetric external dipole magnetic field. In the near zone the poloidal field is largely determined by the currents in the star.In the wind zone the currents due to the escaping charges are the principal source of the magnetic field. There is a toroidal component of the magnetic field (the field lines are bent backwards) whose source in both zones is the poloidal current distribution of the escaping particles. The toroidal field is a minor component in the near zone and a major component in the wind zone.The poloidal field lines become radial far out in the wind zone, and the streaming velocities of the escaping charges approaches c.The outflowing streams of electrons and protons remain separated until they reach the boundary zone.Here, the escaping charges, which really form an electromagnetically driven stellar wind, receive most of their acceleration in the boundary zone. Here the magnetic- field lines are not equipotentials, and the charges move across the poloidal field lines. The charge separation that held in the near and wind zones is destroyed, and both the tangential component of the electric field and the normal component of the magnetic field drop to zero as r approaches D, see Fig.9.2(b).

9.5 Application to the Crab Pulsar

Goldreich and Julian use their model of the pulsar fields to predict that the toroidal magnetic field has a magnitude of the order of 4×10^{-4} - 4×10^{-5} gauss in the boundary zone. This is in agreement with previous estimates of the magnetic-field strength in the Crab.

According to Woltjer (1958) there is some observational support for the contention that the Crab's magnetic field is tangential to the shell boundary. It is suggested that there is an electric field comparable in magnitude to the magnetic field in the Crab. This electric field is of great importance, both because it is essential to the convection of particles away from the star and also because it accelerates the escaping charges to relativistic energies in the outer parts of the nebula. The existence of a large-scale electric field in the Crab removes the difficulty that some previous authors have faced in trying to understand the lifetimes of the high energy, X-ray producing electrons in the nebula.

9.6 Formation of the Outer Gap regions of radiation production

Consider a young pulsar such as the Crab which can sustain pair production in otherwise

charge-depleted regions of the outer magnetosphere (Cheng, Ho and Ruderman 1986a). Charge depletion in regions of the magnetosphere can be a consequence of assumed outermagnetospheric current flow along open field lines between the neutron star and the light cylinder. The shape and location of the depleted region is determined by the physics of the pair production which limits its growth. The resulting gap is expected to exist far from the neutron star, where the corotating magnetosphere would be rotating at speeds a significant fraction of c. For rapidly spinning highly magnetized pulsars such as the Crab, the size and location of this gap supports the production of energetic radiation beams of quite different characteristics than those of the usual coherent microwave emission of radio pulsars. Emission is mainly into pairs of fan beams of X and gamma-rays which span essentially all latitudes: observers would detect two pulses per stellar rotation period. This, then, is the origin of the hard X-ray pulses observed by the *MIFRASO* telescope. The single broad 'precursor' part of the radio pulse of the Crab Pulsar is expected to be produced elsewhere in the magnetosphere by other mechanisms than those

responsible for the outer gap emission.

Fig.9.3 gives a schematic indication of assumed current flow patterns on open field lines of a spinning magnetized neutron star. Current flow of positive charge away from the star is balanced by a return current which is mainly through the 'null surface' $\mathbf{\Omega}.\mathbf{B} = 0$. The inward directed arrows indicate current flow direction only: negative electrons will be outflowing in the dotted region. The closed field lines which do not penetrate the light cylinder are in the shaded area. It is assumed that no steady currents flow on them.

Fig.9.4 shows the expected tangential emission from two points in the radiating region just beyond the boundary of each of two outer gaps. Because the inner gap end is near the 'null surface' where $\mathbf{\Omega}.\mathbf{B} = 0$, radiation from the innermost region is nearly horizontal. A southern hemisphere observer would see two radiation beams, (1) and (3), for each stellar rotation, as long as the viewing angle with respect to the pulsar spin does not fall below θ_o. The probability for seeing such beams from the Crab Pulsar would, therefore, be expected to be high.

The observed phase separation between double pulses is determined by (1) the flight path difference between the two beams, one of which must traverse almost the whole magnetosphere as indicated in Fig.9.4.; (2) aberration of the emitted beam direction and (3) magnetic field line bending near the light cylinder because of retardation or plasma loading or both. Cheng, Ho and Ruderman (1986a) have calculated the results for straight radial field lines (a monopole field) as a function of emission position and viewing angle. They find that the pulse phase separation of 140^o observed in the Crab Pulsar does not require exceptional viewing angles or emission positions. The observed separation does, however , suggest an emission region whose distance to the spin axis is about $0.6 r_{LC}$

9.7 Spectrum of the Crab Pulsar

As detailed in the previous section, to explain the origin and mechanism of the energetic radiation from the Crab Pulsar, a model has been proposed based on the formation of a finite

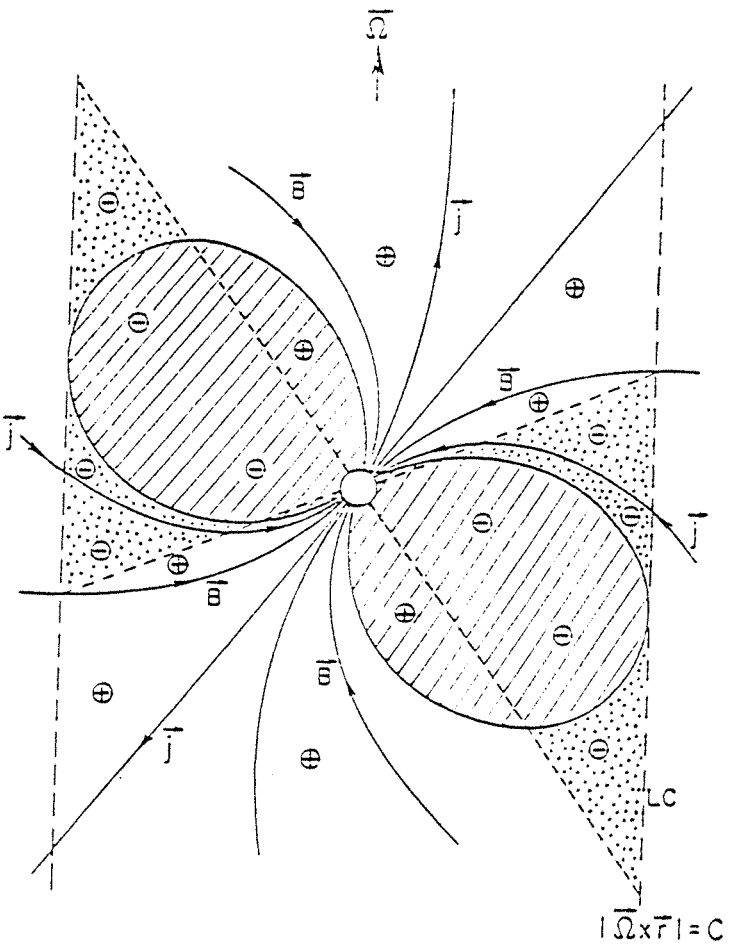

Fig.9.3. Assumed current flow patterns on open field lines around a spinning magnetized neutron star. From Cheng, Ho and Ruderman, 1986a.

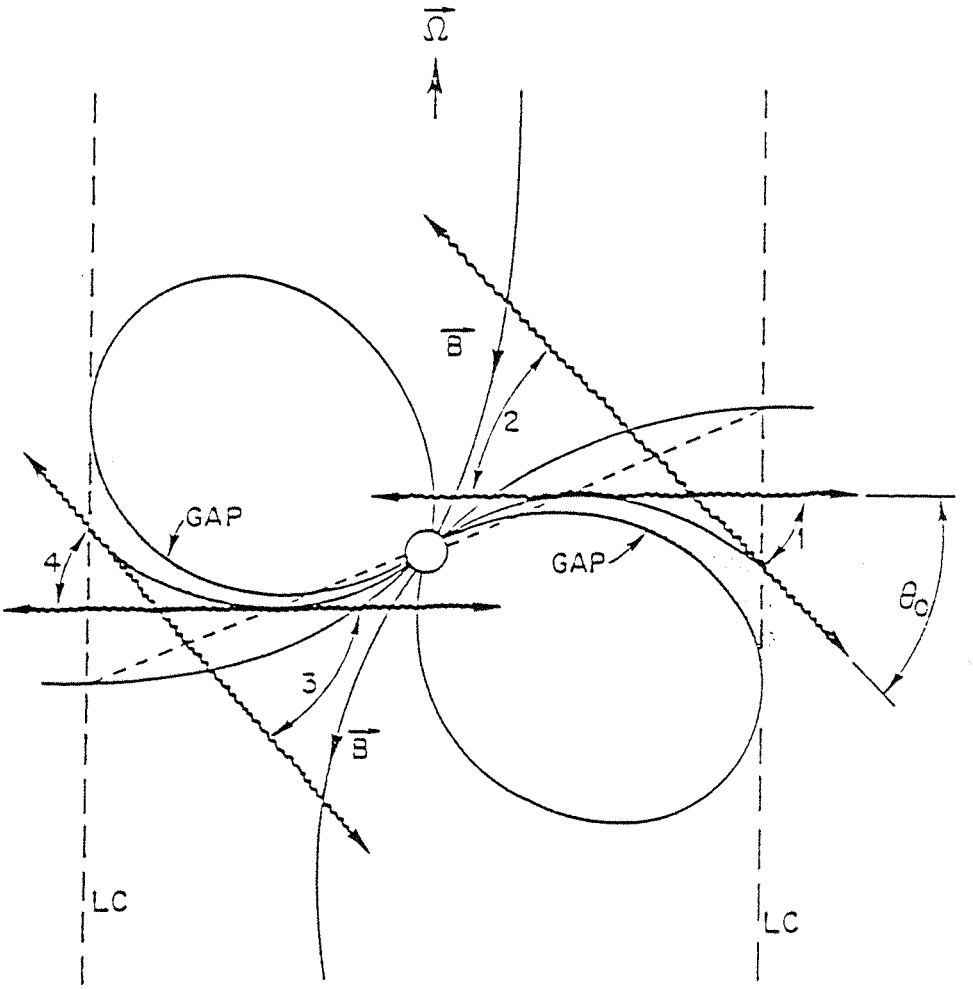

Fig.9.4. The tangential emission from two of the outer gaps in the pulsar magnetosphere. From Cheng, Ho and Ruderman, 1986a.

region of vacuum gap in the outer magnetosphere. In the Crab Pulsar, the gap produces GeV photons via curvature radiation and subsequently produces secondary electron-positron pairs ($\sim$ 100eV) which radiate synchrotron radiation and inverse-Compton-scattered photons. These produce the observed flux of X and gamma-rays.

In Cheng, Ho and Ruderman 1986b, the continuum spectrum of pulsed radiation was calculated for the Crab Pulsar and the result agreed semi-quantitatively with observations. Further to this, a single-parameter model has been constructed to calculate the spectra from the outer gap of the Crab Pulsar without the need for observational data as input (Ho 1989).

An outer gap is an extensive region of vacuum near the light cylinder ($r = c/\Omega$) which results from current flow along the open field lines. The Crab outer gap is shown in Fig.9.5. A gap of height a will induce an electric field with substantial component parallel to the magnetic field. The maximum parallel electric field is

$$E_{max} = \Omega B a^2 / 4sc \tag{5}$$

and the maximum potential drop along the gap is

$$V_{max} = \Omega B a^2 L / 4sc \tag{6}$$

where s is the radius of curvature of the field lines,Ω is the angular frequency of the pulsar, B is the local magnetic field strength and L is the length of the gap. The gap is bounded from below by the last closed field line assumed to be dormant with a static surface charge density

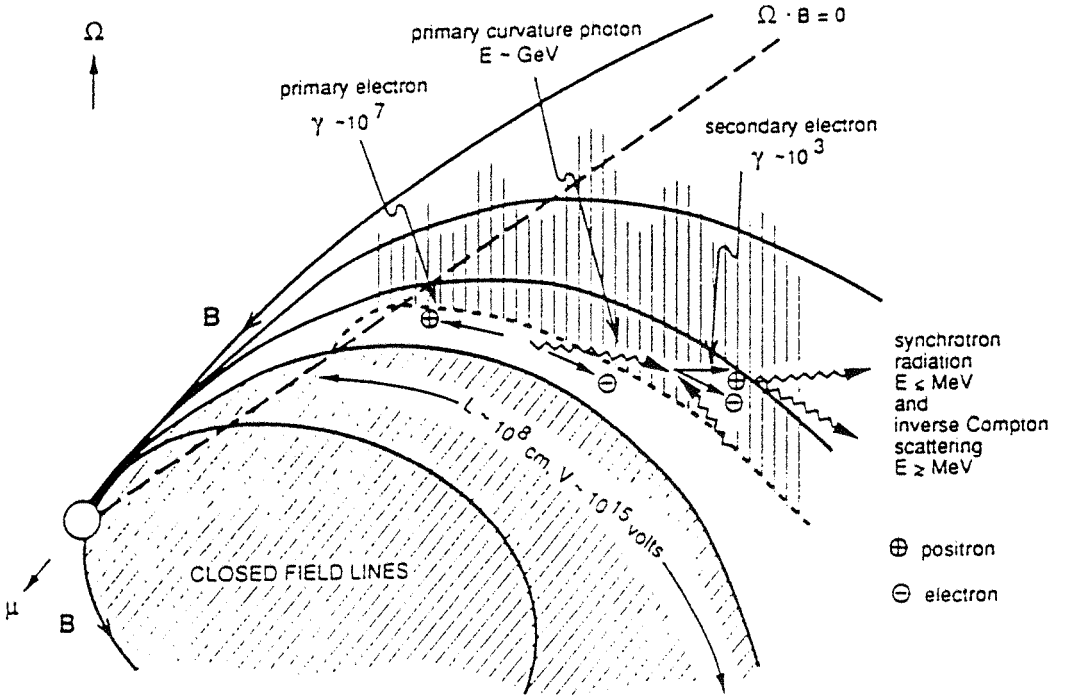

Fig.9.5. The Crab outer gap in the magnetosphere. The outer gap resides above the closed-field line region (diagonally shaded region) and the short -dash line. From Ho, 1989.

$$\Sigma = \Omega B a x / 4\pi c \tag{7}$$

where x is the distance along the gap. The upper boundary of the gap resides in the region threaded by open field lines and is not static. Electric current flows along it and constant charge production and separation maintain the surface charge density. The current in the upper boundary is given by

$$I \sim \Omega B a W L / 4\pi s \tag{8}$$

where W is the breadth of the gap. The surface charge density on the upper and lower boundaries shields the gap from the rest of the magnetosphere.

In the outer gap of the Crab Pulsar, 'primary' electrons accelerated by the electric field of the gap (equation 7) contribute to the electric current (equation 8) and radiate predominantly through curvature radiation ('primary photons') as they move along the curved magnetic field line. These primary photons typically have energy around several GeV and they annihilate into electron-positron pairs ('secondary' electrons) when they encounter a flux of keV X-ray photons in the head-on direction. The secondary electrons emit synchrotron radiation typically into energy bands below several MeV. The secondary electrons inverse-Compton scatter the X-ray synchrotron radiation emitted by the crossing beam of secondary electrons into the energy band greater than several MeV. These two components, the synchrotron and inverse-Compton, combine to yield the emergent spectrum ('secondary photons').

In the new model (Ho 1989) the outer gap is parameterized by the linear fraction of the gap :

$$f_G = a/s \tag{9}$$

The available potential drop along a gap with size f_G is given by equation 6 and the current in the upper boundary is given by equation 8. Assuming that the maximum potential drop along the gap is completely accessible by the current in the upper boundary of the gap, the total potential drop along the gap determines the energy of the primary electron and the total current determines the overall normalization. Taking

$$s = W = L = R_{LC} = c/\Omega \tag{10}$$

and

$$B = \mu R_{LC}^{-3} \tag{11}$$

where μ is the dipole moment of the pulsar. Applying this model to the Crab Pulsar where Ω = 190 rad s^{-1},μ = 3.8 $\times$ 10^{30} G cm^3 and D = 2kpc. The theoretical spectra of the Crab Pulsar after 10 iterations for f_G = 0.3,0.4,0.5 and 0.6 are shown in Fig.9.6. The general features include (1) a synchrotron-radiation component which can be described by a power law with a slowly-varying power-law index at the low-energy end and (2) a component from the inverse Compton scattering at the high energy end. These two components overlap at a photon energy between 300 keV and 30 MeV which produce a broad dipping feature in the spectrum. The synchrotron-radiation component at lower-energy is expected to be polarized. This is seen in the phase-resolved observations of the optical pulses from the Crab (Manchester and Taylor

1977).

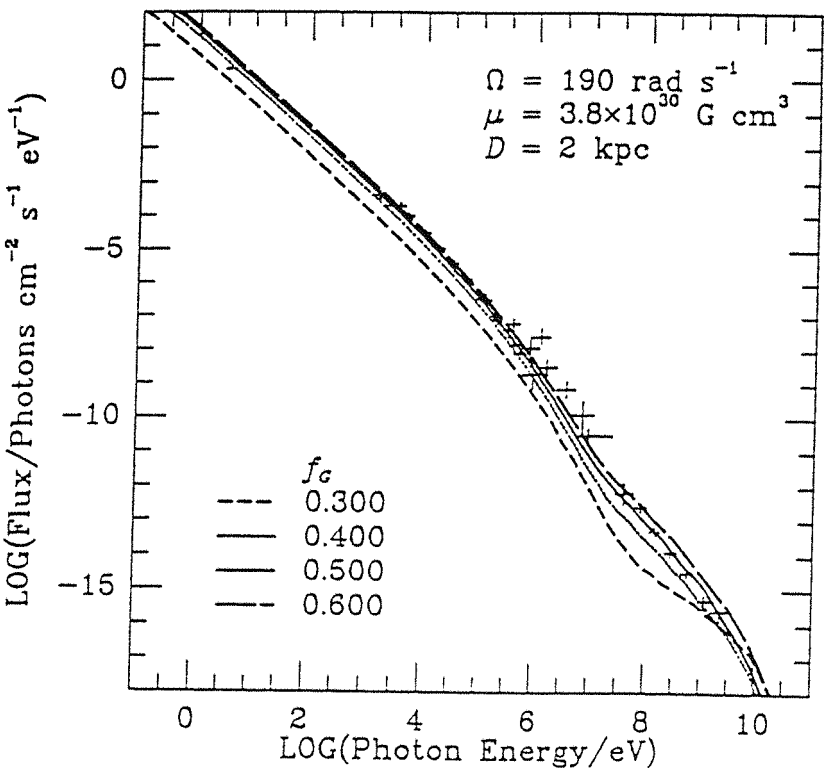

Fig.9.6. The theoretical spectra of the Crab pulsar after 10 iterations with f_G as shown, compared to some observations. From Ho, 1989.

CONCLUSIONS

The aims of this thesis have been twofold. Firstly, to demonstrate that the newly-proposed kernel density technique applied to the estimation of the Crab Pulsar light-curve worked and was superior to the traditional binning of event phases into a histogram. Secondly, the KDE method was applied to the *MIFRASO* observations and spectral deconvolution of the time-averaged and pulsed components of the Crab Pulsar light-curve has been performed.

The use of the kernel density estimator technique has proved to be very successful when applied to the *MIFRASO* hard X-ray observations of the Crab Pulsar, although there is some question as to whether the Hart rule for the truncation point of the harmonic series gives a clear end point for the hard X-ray observations. Application of the M test to the three high energy detectors' pulse profiles has shown that they are consistent to the third harmonic. This is in agreement with the Rayleigh power spectrum of the phase density distribution being dominated by the first three harmonics. Cutting the data into discrete energy bands produced the energy resolved pulse profiles which showed an increasing filling in of the interpulse at higher energies. One of the data cuts also suggested the presence of a sub-pulse in the pulse profile. Possible explanations for this sub-pulse include either an instantaneous plasma clump in the magnetosphere or a third outer gap coming into the line of sight.

It has been suggested that the adaptive cluster density estimator method recently proposed for the analysis of gamma-ray light curves might also be suitable for the analysis of such hard X-ray light curves as presented in this work. This would provide a firm statistical assessment of any microstructure within the pulse profile and represent a new tool for the analysis of pulsar pulse profiles. It is hoped that such use of cluster density estimators will form the basis of future work (see Appendix 2).

The search for cyclotron emission has failed to identify any such line feature in the decon-

volved time-averaged spectrum. The pulsed component has been successfully measured from the pulse profiles and its energy spectrum separately deconvolved. Again, no cyclotron line feature was seen. The pulsed emission has yielded a harder spectrum than the time- averaged spectrum. This is consistent with previous results. The pulsed component is thought to originate from a different part of the pulsar than the time- averaged component, which has contributions from the synchrotron Nebula.

The new tools for pulsar analysis are recommended for application in other wavebands, for example, where the number of photons collected is small and consequently the resulting pulse profiles are more controversial. The $H_{\dot{m}}$ test for pulsar periodicity searches has been demonstrated to be more powerful than the conventional Pearson or Rayleigh tests and its performance has been confirmed using a search on the Crab Pulsar signature. Its use is strongly recommended in future X and gamma-ray analysis work.

As an example of the new techniques, Fig.C.1 shows the COS-B light curve of the Vela pulsar above 100 MeV analysed using three different methods: a histogram estimator with 100 bins, a cluster density analysis with 0.05 probability threshold and a kernel density estimator analysis with $\pm 2\sigma$ confidence bands.

A preliminary timing analysis of the X-ray binary system Cygnus X-1 has been performed, and no pulsations have been detected. The range of trial periods searched so far is very small and further analysis is presently underway by the author to extend the range of trial periods tested. Despite this limitation, the exercise shows the feasibility of using the $H_{\dot{m}}$ test for searching for an unknown period.

Finally, on the computational side, this thesis has shown the great speed advantages to be gained for intensive routines using transputers running parallel code such as OCCAM (see Appendix 3). The use of such parallel machines represents a huge leap forward in terms of computing resources available to the astronomical community, a leap forward it cannot afford

to ignore.

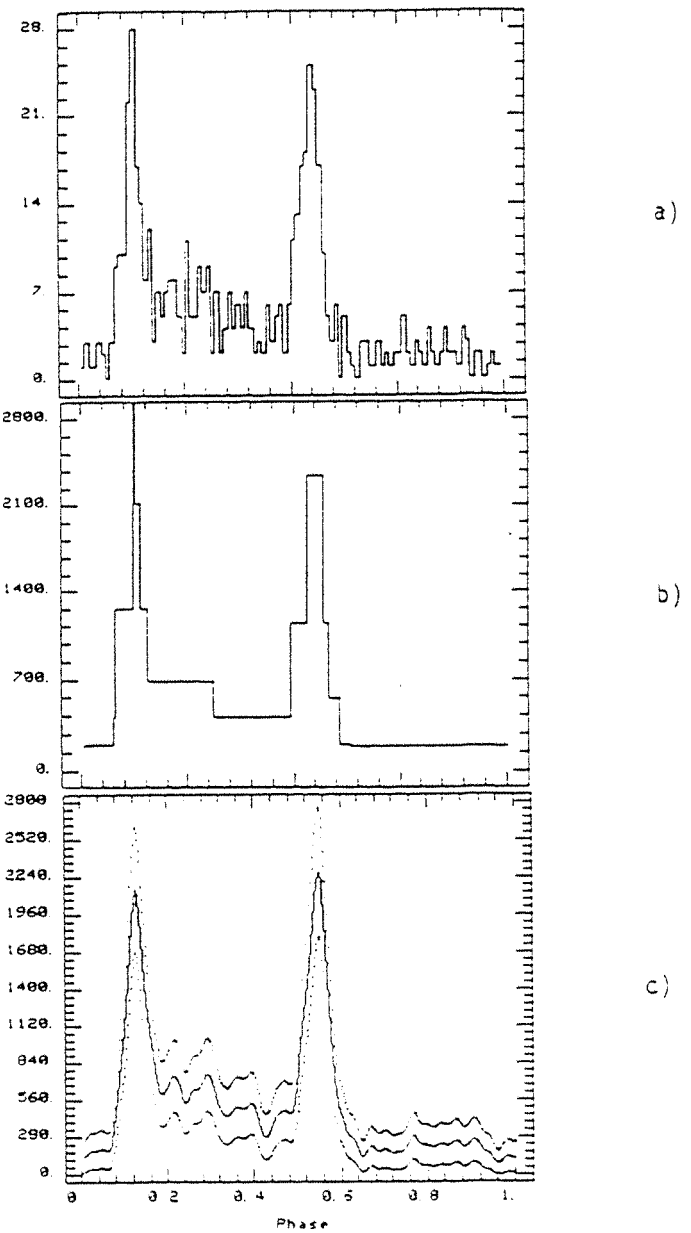

Fig.C.1.The light curve of the Vela pulsar above 100 MeV as observed by the COS-B satellite analysed using the following estimators: (a) histogram with 100 bins, (b) cluster density estimator with 0.05 probability threshold and (c) kernel density estimator with 2σ confidence bands.

APPENDIX 1 : THEORETICAL OBSERVATION OF A 'CRAB-LIKE' SOURCE

The following is a simple model to predict the countrate excess that $MIFRASO$ should observe from a 'Crab-like' source, given a known spectral index of emission from the source together with atmospheric attenuation and detector response functions. This is then compared to the observed countrate excess.

Let the count-rate observed by $MIFRASO$ from the Crab be S counts s^{-1}. Then,

$$S = D \int_{E_{min}}^{E_{max}} I(E).R(E).A(E) \quad \mathrm{dE}$$

where D is the detector area, $I(E)$ is the source spectrum, $R(E)$ the instrument detector response, $A(E)$ is the atmospheric attenuation and E_{min} and E_{max} are the energy limits of $MIFRASO$, taken as 20 keV and 300 keV respectively.

For a simple model, the energy spectrum of the Crab can be approximated by

$$I(E) = 10E^{-2.16}.$$

The instrumental detector response is shown in Fig.A1.1 and may be approximated by

$$R(E) = 2E - 10 \qquad 20 < E/keV < 45$$

$$R(E) = 92 - 0.28E \qquad 45 < E/keV < 300$$

The atmospheric attenuation is shown in Fig.A1.2 and may be approximated by

$$A(E) = 1.8E - 21 \qquad 20 < E/keV < 45$$

$$A(E) = 0.6 \qquad 45 < E/keV < 300$$

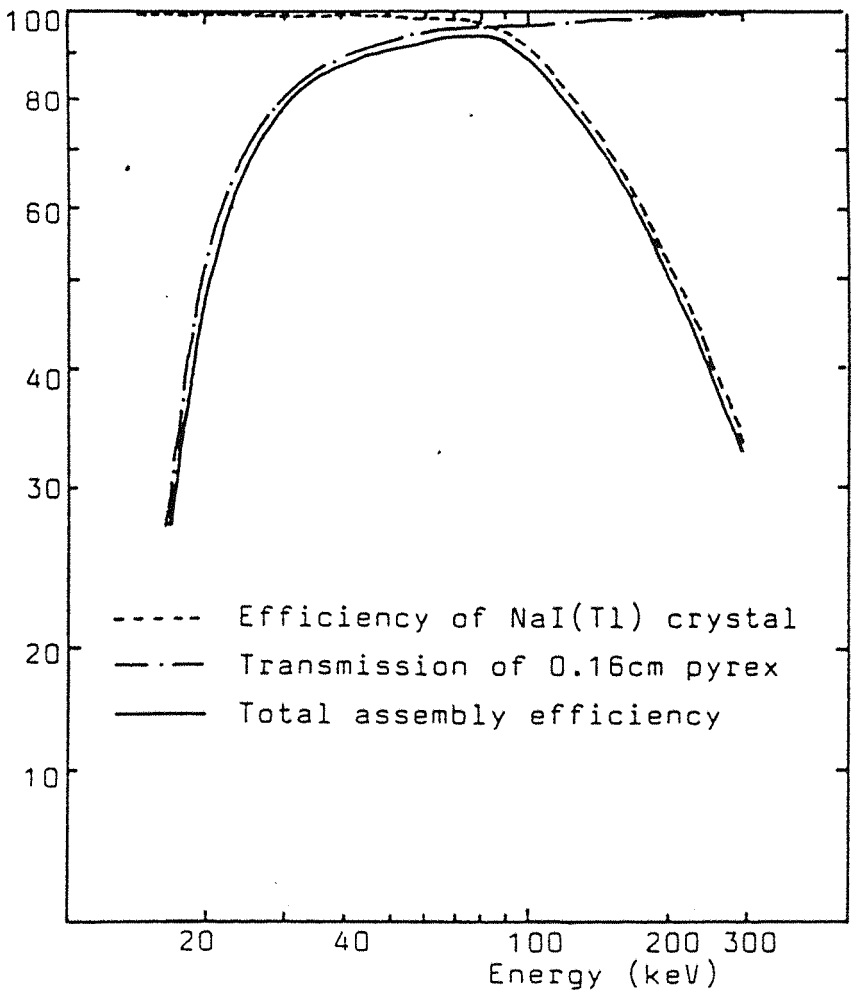

Fig.A1.1. The total assembly efficiency for the high energy detectors on board the *MIFRASO* telescope. From Lewis, 1984.

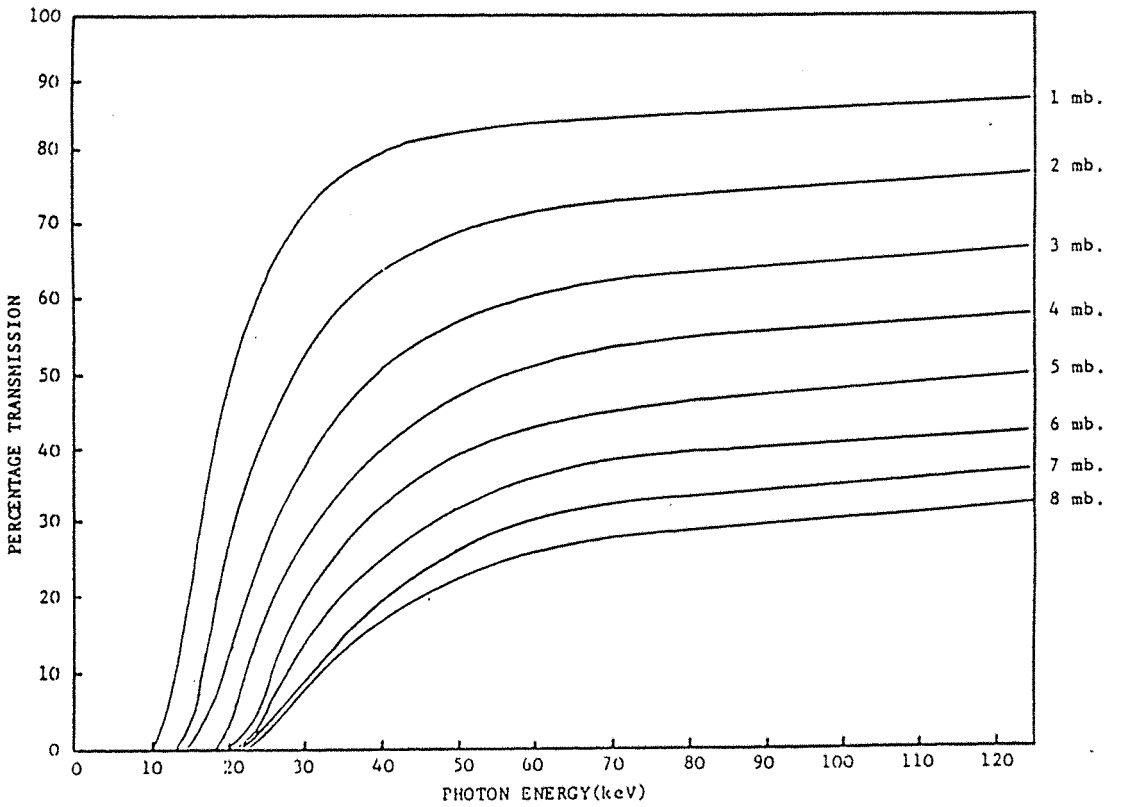

Fig.A1.2. The atmospheric transmission as a function of X-ray energy. From Lewis. 1984.

Combining the two,

$$R(E).A(E) = aE - b \qquad 20 < E/keV < 45$$

$$R(E).A(E) = c - dE \qquad 45 < E/keV < 300$$

where the coefficients are found to be $a = 0.0174, b = 0.3030, c = 0.5540, d = 0.0016$.

With D=2656 cm^2, performing the integral, the total on-source count-rate excesses from a 'Crab-like' source is given by

$$S \sim 130 \text{ counts s}^{-1}$$

From the *MIFRASO* observations, the observed excess is about 100 counts s^{-1}.

APPENDIX 2 : CLUSTER DENSITY ESTIMATORS

The use of the cluster density estimator analysis technique (CDE) is a non-parametric, bin-free, adaptive method for the detection and analysis of microstructures within the pulse profiles of pulsars. (Buccheri et al., 1988). For example, the *MIFRASO* observations of the Crab Pulsar have yielded several interesting microstructures within the pulse profiles (see Figs. 7.1 and 7.5). CDE is a method of distinguishing these suspected structures from merely statistical fluctuations, that is, it provides a probability level that the fluctuation has arisen by chance. Even the KDE method suffers from smoothing, that is, microstructures may be lost due to the global smoothing inherent in the process. CDE does not suffer from this, and is a complementary method to KDE. It exploits the full timing resolution of the instrument involved.

Microstructures have been detected so far in the radio range (Craft et al., 1968; Boriakoff et al., 1981) and refer to single micropulses which may represent instantaneous clumps of plasma in the pulsar magnetosphere. In the high-energy domain, microstructures may represent more intrinsic properties of the polar cap or magnetospheric outer gaps of the pulsar and could therefore add important information to the morphology of the magnetosphere in its long term evolution.

The CDE method is based on a single link cluster algorithm applied to the residual phases corresponding to the arrival times of the selected photons. The residual phases are sorted into ascending order thus building a one dimensional Minimum Spanning Tree (Zahn, 1971). The choice of threshold on the distance between consecutive phases allows the tree to be cut in several places thus selecting a number of 'clusters' of residual phases with mutual interdistances below the given threshold (Di Gesu and Sacco, 1983). On each individual cluster a statistical analysis is performed to evaluate the probability that the cluster may occur by chance from uniformly distributed phases. For the low counting rates of gamma-ray astronomy, the Erlangian function is used (Eadie et al., 1971). However, for the relatively high counting rates found by the

MIFRASO telescope the normal distribution function is more appropriate (Busetta, private communication). A threshold on the probability allows to define the clusters as 'significant'; when this occurs the phase density, which was assumed to be uniform in the interval (0,1) at the beginning of the analysis, is modified by including a square peak in the position of the detected significant cluster; outside of the peak the phase density is accordingly reduced such to keep equal N (the total number of phases under analysis) the integral of the phase density distribution over the whole phase interval. The peaks found in this way do not suffer any bias in their width and phase location, the only error being of statistical nature; furthermore, all the clusters for which the probability for chance occurrence is above the threshold are considered as fluctuations of the background and are smoothed down. Repeating the process several times with decreasing interdistance thresholds allows the investigation of narrower and narrower structures and the derivation of an estimate of the parent density distribution from which the measured phases are sampled.

Fig.A2.1 shows a cluster analysis performed on the COS-B gamma-ray observation of the Crab pulsar, compared to the traditional binning technique. There is a significant cluster ($> 3\sigma$) at relative phase 0.1, representing some microstructure within the pulsed emission. This has important implications for pulsar magnetosphere models and theory of the pulsed emission.

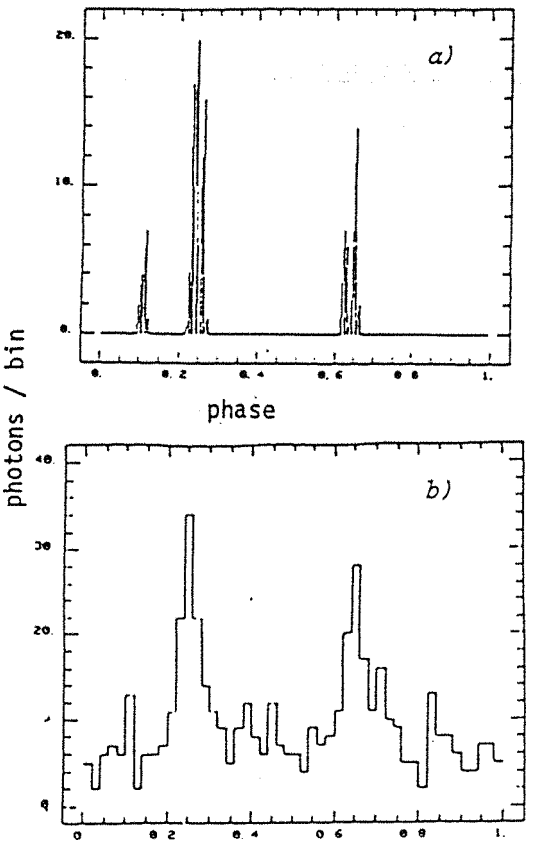

Fig.A2.1.(a) A cluster analysis performed on the COS-B observation of the Crab Pulsar showing the detection of a microstructure in the light-curve at relative phase 0.1. The binned light-curve is shown in (b) for comparison. From Buccheri et al., 1988.

APPENDIX 3 : TIMING AND EFFICIENCY COMPARISON OF A PARALLEL IMPLEMENTATION OF THE $H_{\hat{m}}$ TEST

Timing comparisons were made for periodicity searches using the $H_{\hat{m}}$ test performed on a μVAXII and on an M-10 Computing Surface (Carstairs and Gorrod, 1989). The results are shown in Figs.A3.1 and A3.2 for sets of 2.10^3 and 2.10^5 event times respectively, expressed as execution time as a function of the number of transputers used and searching over 11, 51 and 101 trial periods. The trivial search over 11 trial periods for 2.10^3 events was chosen to indicate any drawbacks inherent in the parallel implementation.

The graphs illustrate the performance characteristics of the implementation and it may be seen how increasing the processing resources affects the execution time. This may be investigated further by examining the efficiency of the implementation following the definition given by Fox (Fox, 1985), where, for N processors,

$$efficiency = \frac{time\ on\ one\ processor}{N \times time\ on\ N\ processors}.$$

Ideally the implementation with N processors should run N times faster than one processor and the efficiency would be 100%. However, because of communication overheads and the fact that not all the processing resources are always being utilised to the full (that is, the implementation is not perfectly load-balanced), this is rarely the case.

For the case of 11 trial periods increasing the number of transputers does not decrease the execution time after $N = 4$ (see Fig.A4.1) and the remaining two curves seem to level out at this value of N. This is due to the saturation of the communication link between the Computing Surface and the μVAXII. This link has a limited bandwidth and high response time, giving a minimum load time for the data. If the dataset is preloaded then efficiencies of $> 95\%$ can be achieved with 12 transputers (on all the sets of trial periods and 2.10^5 event times), indicating

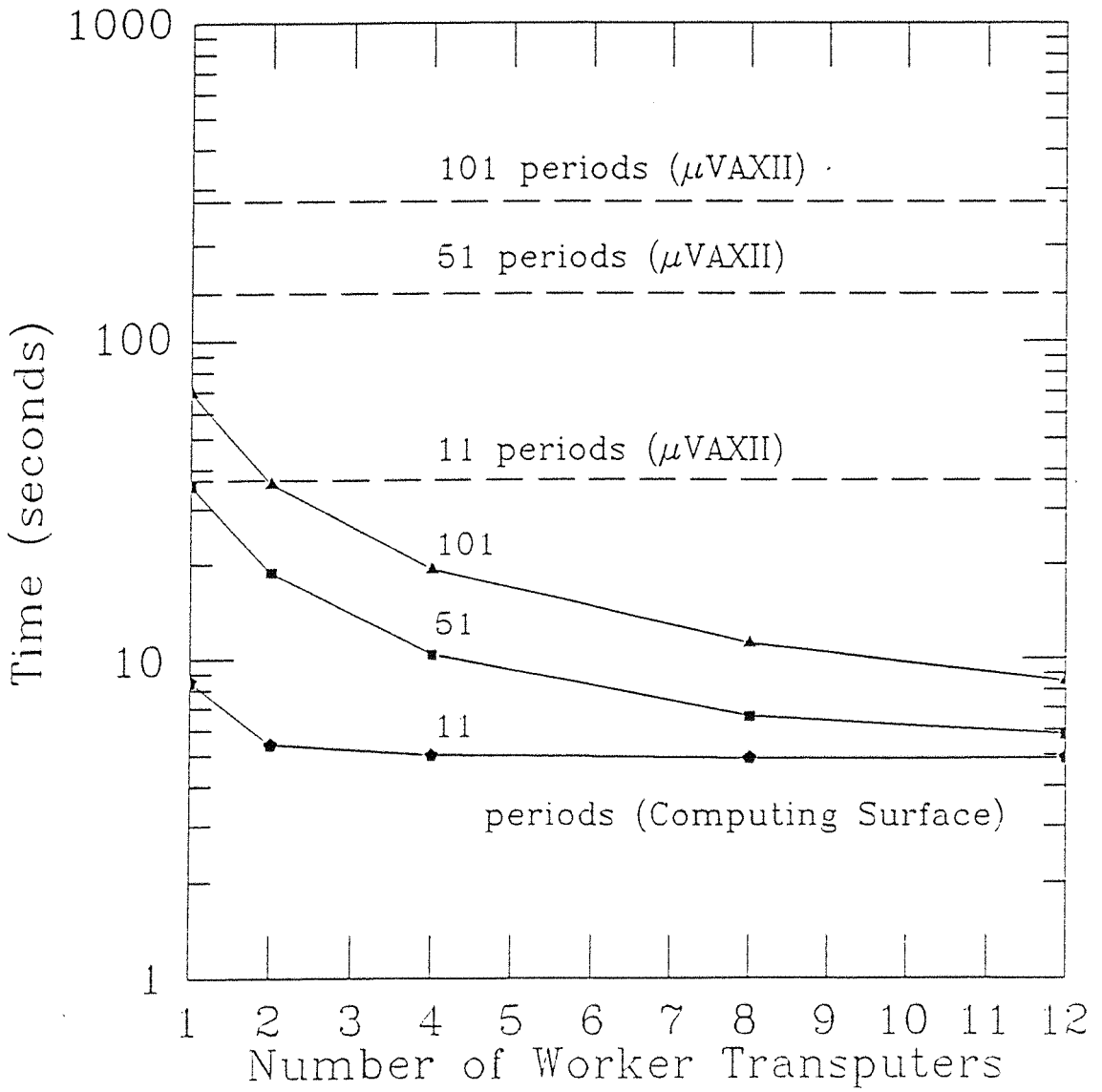

Fig.A3.1. The performance characteristics of a parallel implementation of the $H_{\tilde{m}}$ test for a varying number of worker transputers compared to the same test implemented on a μVAXII. The number of events searched over was 2.10^3. From Carstairs and Gorrod, 1989.

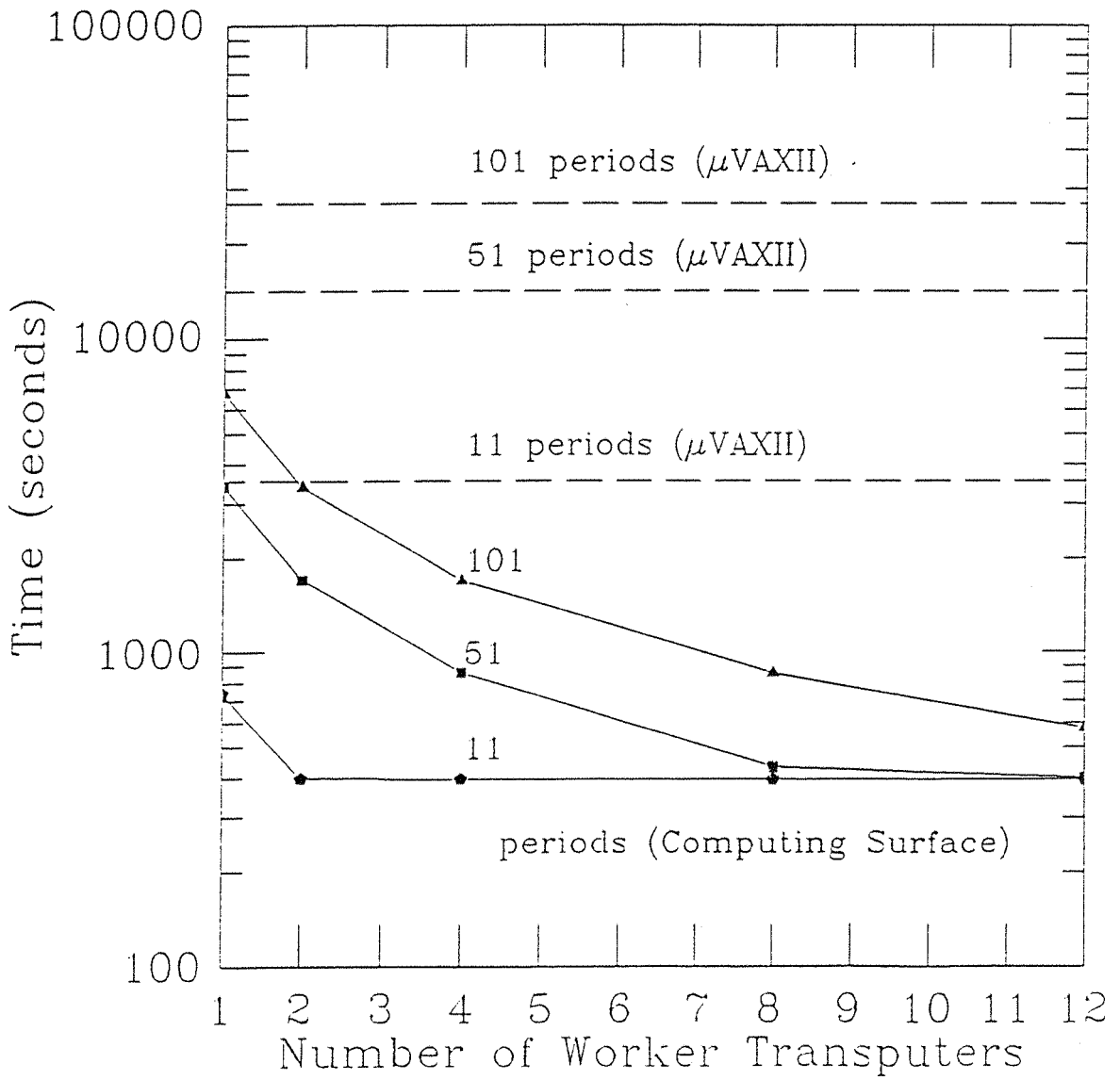

Fig.A3.2. The same set of performance characteristics as for the previous figure, but this time searching over 2.10^5 events. From Carstairs and Gorrod, 1989.

that there are no major communication bottlenecks or overheads associated with the pipeline code. The communication link problem may be overcome by the use of a faster fileserver (such as a Sun workstation) or by using a separate disk system connected directly to the transputer array. One further problem that can limit the efficiency with a search over a small number of trial periods is the time taken to convert the formatted event time data into its internal representation. Although this can be performed quickly it is possible that the data can be processed faster by the worker processors than the master can generate it. This may be solved by using unformatted data files. Another possible solution is to output the formatted data to the workers which then convert it to its internal representation. This will increase the volume of data being transferred over the links and increase the communications overhead. However, because this implementation is bandwidth limited between the fileserver and the Computing Surface the data is being converted to its internal representation faster than it can be loaded from the fileserver. Ultimately the problem is limited by the speed of the transputer links themselves and the communications overheads involved in forwarding the data, which will restrict the size of the array. In this case an alternative network structure should be used (Pritchard, 1987).

Despite these considerations efficiencies of $> 98\%$ are still being obtained for the case of searching over 101 trial periods with 2.10^5 event times using the $H_{\hat{m}}$ test. This efficiency will be improved for a search over a longer trial period set as the ratio of communications to computations decreases. However, initial overheads in preparing and loading the data by the master will decrease the efficiency for small event time datasets. This overhead is very low but will be noticeable when the calculations on small datasets can be performed in only a few seconds, see Fig.A3.1 for the case of 11 trial periods.

REFERENCES

'*' indicates joint authorship of a paper by the author

Agrinier et al., *Ap.J.*, 355:645, 1990.

Avni and Bahcall, *Ap.J.*, 197:675, 1975.

Avni, *Ap.J.*, 210:642, 1976.

Baade and Zwicky, *Proc. Nat. Acad. Sci*, 20:254, 1934.

Baity et al., *Ap.J.*, 279:555, 1984.

Baker et al., *Nucl. Instr. and Meth.*, 228:183, 1984.

Bazzano et al., *Nucl. Instr. and Meth.*, 214:481, 1983.

Bickel and Rosenblatt, *Ann. Stat*,1(6):1071, 1973.

Bolton, *Ap.J.*, 200:269, 1975.

Boriakoff et al., *IAU Symp.No.*95, p. 191, 1981.

Boynton et al., *Ap.J.*, 175:217:1972.

Bradt et al., *Ap.J.*, 204:L67, 1976.

Brecher and Caporaso, *Nature*, 259:377, 1976.

Buccheri et al., *AAP.*, 128:245, 1983.

Buccheri et al., *AAP.*, 201:194, 1988.

Carstairs and Gorrod, *Proc AAPP Workshop , Southampton*, 1989.

Cheng, Ho and Ruderman, *Ap.J.*, 300:500, 1986a.

Cheng, Ho and Ruderman, *Ap.J.*, 300:522, 1986b.

Cocke et al., *Nature*, 221:525, 1969.

Cocke,*Ap.J.*,202:773, 1975.

Coe et al., *Nature*, 256:630, 1975.

Coe et al., *MNRAS*, 243:475, 1990. *

Court, *Ph.D. thesis*, University of Southampton, 1987.

Craft et al., *Nature*, 218:1122, 1968.

de Jager, *Ph.D. thesis*, Potchefstroom University, 1987.

de Jager et al., *Ap.J.*, 329:831, 1988.

de Jager et al., *AAP.*, 221:180, 1989.

Dolan et al., *reference not found*, 1977.

Eadie et al.,*Statistical Methods in Experimental Physics*, Amsterdam, p.74, 1971.

Ferguson et al., *Ap.J.*, 190:375, 1974.

Fox, *Caltech Report* C^3 $P-255$, 1985.

Fritz et al., *Science*, 164:709, 1969.

Gerardi et al., *Proc Compstat'*82, 1982.

Goldreich and Julian, *Ap.J.*, 157:869, 1969.

Groth, *Ap.J.Suppl.Ser.*, 29:431, 1975a.

Gullahorn et al., *Ap.J.*, 82:309, 1977.

Hart, *J. Statist. Comput. Simul.*, 21:95, 1985.

Hewish et al., *Nature*, 217, Febuary 24, 1968.

Hillier et al., *Ap.J.*, (Letters), 162:L177, 1970.

Ho, *Proc. GRO Workshop*, 174, 1989.

Hoel, '*Intoduction to Mathematical Statistics*', New York:Wiley, 1971.

Horowitz et al., *Ap.J.*, (Letters), 172:L51, 1972.

Hutchings, *Ap.J.* (Letters), 193:L61, 1974.

Korn and Korn,'*Mathematical Handbook for Scientists and Engineers*'. New York:McGraw-Hill, 1968.

Kurfess and Share, *Nature Phys. Sci.*, 244:39, 1973.

Lewis, *Ph.D. thesis*, University of Southampton, 1984.

Ling et al., *Ap.J.*, 231:869, 1979.

Lyne and Thorne, *MNRAS*, 172:97, 1975.

Lyne et al., *MNRAS*, 229:223, 1987.

Lyne et al., *MNRAS*, 233:667, 1988.

Manchanda et al., *Ap.J.*, 252:172, 1982.

Manchester, *Ap.J.*, 172:43, 1972.

Manchester and Taylor,'*Pulsars*'. Freeman and Co., 1977.

Mardia, '*Statistics of Directional Data*', Academic Press, 1972.

Mitton,'*The Crab Nebula*'.Faber and Faber, 1979.

Muncaster and Cocke, *Ap.J.*, (Letters), 178:L13, 1972.

Mushotzky et al., *Ap.J.*, 235:377, 1980.

Oppenheimer and Volkoff, *Phys. Rev.*, 55:374, 1939.

Pagels, *Perfect Symmetry*, Michael Joseph, 1985.

Papaliolios et al.,*Nature.*,228:445, 1970.

Parzen, *AMS.*, 33:1065, 1962.

Perotti et al., *Nature*, 282:484, 1979.

Perotti et al., *Ap.J.*, (Letters), 255:L115, 1981.

Perotti et al., *Ap.J.*, 356:467, 1990.

Priedhorsky and Terrell, *Nature.*, 303:681, 1983.

Pritchard, *Proc.* 7^{th} *OCCAM User Group Technical Meeting*, Grenoble, 1987.

Rankin et al., *Ap.J.*, 162:707, 1970.

Rankin et al., *Ap.J.*,(Letters), 193:L71, 1974.

Rhoades and Ruffini, *Phy. Rev. Letters*, 32:324, 1974.

Richards and Comella, *Nature*,222:551, 1969.

Ricker et al., *Ap.J.*, 204:L73, 1976.

Rosenberg et al., *Nature*, 256:628, 1975.

Rosenblatt, *AMS.*, 27:832, 1956.

Rothschild et al., *Ap.J.*, 213:818, 1977.

Ruderman, *Ap.J.*, 203:213, 1976.

Ruderman, *Ap.J.*, 382:576, 1991a.

Ruderman, *Ap.J.*, 382:587, 1991b.

Staelin and Reifenstein, *Science*, 162:1481, 1968.

Standish, *AAP*, 144:297, 1982.

Strickman et al., *Ap.J.*, 230:L15, 1979.

Strickman et al., *Ap.J.*, 253:L23, 1982.

Swanepoel, *CIS.*, 1987.

Ubertini et al., *Space Sci. Instr.*, 5 :237, 1981.

Ubertini et al., *Nucl. Instr. and Meth*, 217:97, 1983.

Ubertini et al., *Ap.J.*, 284:54, 1984.

van den Bergh and Pritchet, *Ap.J.*,(Letters),338:L69, 1989.

Ward et al., *AAP.*, 59:L19, (1977).

Weisskopf et al., *Ap.J.*, (Letters), 208:L125, 1976.

Wilson, *MNRAS*,166:499,1972.

Woltjer, *B.A.N.*, 14:39 (no.483), 1958.

Yaqoob et al., *MNRAS*, 236:153, 1989.

Zahn, *IEEE Trans. Comput.*, c-20:68, 1971.

ACKNOWLEDGEMENTS

I would like to thank all those people who have helped me through the years throughout this work, especially :

My supervisor at Southampton University, Dr. David Ramsden for his guidance and advice; my supervisor (and external examiner) Dr. Keith Orford for my time with the Durham VHEGRA group and for introducing me to the world of kernel analysis; Dr. Jeremy Lloyd-Evans for his continual encouragement and advice on statistics; Dr. Francesco Perotti for guiding the *MIFRASO* project and for performing the energy deconvolutions presented here; Dr. Paolo Maggioli for much helpful advice; Dr. Okkie de Jager of Potchefstroom University for much help and advice concerning kernel analysis; all members of the *MIFRASO* collaboration, past, present and (hopefully) future; Professor Arnold Wolfendale for his advice; Dr. Nigel Dipper for inspiration to travel south; Dr. John Douthwaite for continuity from north to south; Martin Gorrod for getting me involved with transputers; Dr. Andy Norton for help with the *MIFRASO* software; Drs. Tony Dean, Malcolm Coe and Andy Court for many useful discussions;Drs. Bernie Payne and Mike Yearworth for helping me with the computing, and all members of the Southampton University Astronomy Group.

I would like to thank Dr. Heather Couper for introducing me to Southampton University; Dr. Carl Sagan for his inspirational *Cosmos* TV series and Regina for her paintings and poetry.

Special thanks to Tim Watkinson for putting me up on his floor for so long, and for being a great friend.

I am especially grateful to Drs. M. Bernadt and P.Nott for much helpful advice and guidance. Like the *MIFRASO* telescope, the author runs on lithium.

Finally, I would like to thank my parents and family for their constant support throughout my postgraduate career.

This work was financed by the Science and Engineering Research Council and the Department of Social Security.